The Thesis Committee for Yunhan Huang
Certifies that this is the approved version of the following thesis:

Designing a Laboratory Model Test Program for Developing a New Offshore Anchor

APPROVED BY
SUPERVISING COMMITTEE:

Supervisor: _____
Robert B. Gilbert

Co-Supervisor: _____
Ellen M. Rathje

Designing a Laboratory Model Test Program for Developing a New Offshore Anchor

by

Yunhan Huang, B.S.E.

Thesis

Presented to the Faculty of the Graduate School of

The University of Texas at Austin

in Partial Fulfillment

of the Requirements

for the Degree of

Master of Science in Engineering

The University of Texas at Austin

May 2015

Dedication

To my parents

Acknowledgements

I am thankful to Professor Robert B Gilbert for his valuable suggestions and guidance on my thesis. I was privileged to be a student of such an intelligent professor who was the smartest person I ever met. His ingenious algorithm for using Excel gave me a complete understanding of this powerful software. He kept me learning and is an excellent mentor.

I would like to thank my Pick Research Campus team: Hande, Asitha, and Ying for their help and support. We had a lot of good times at the Pickle Research Campus. I enjoyed every lunch with them and every second working with this team. I appreciate Hande ‘s patience in guiding me into the offshore anchor world. I appreciate Asitha for his intelligence and introducing me many electric devices and software programs. I appreciate Ying for her kindness in helping us build set up for many tests.

I am grateful to Professor Ellen M Rathje for her wonderful teaching style and big smile when she talked with me. I also thank the faculty in Geotechnical Engineering for their support in my two years of graduation study.

Thanks to Eugenio for his every patient discussion. Thanks to Huamiao for his positive life style. Thanks for Jinbo for his advice. Thanks to my group work team: Benchen, Yumeng, and Tianjian for the interesting discussions last semester. Thanks to all my friends at The University of Texas at Austin.

Special thanks to my parents Jialin and Rong for their love and care. I love my family so much.

Abstract

Designing a Laboratory Model Test Program for Developing a New Offshore Anchor

Yunhan Huang, M.S.E.

The University of Texas at Austin, 2015

Supervisor: Robert B. Gilbert

Co-Supervisor: Ellen M. Rathje

The Flying Wing Anchor (patent pending) is a new anchor concept that combines the features of dynamically penetrating anchors, drag embedment anchors, and plate anchors. To study and optimize the behavior of the new anchor, this study developed a simplified predictive model and a new data acquisition system for performing physical model tests. The simplified predictive model couples a limit-equilibrium-based model for the anchor line and a plasticity-based model for the anchor to predict the embedment trajectory and holding capacity of the new anchor. The new data acquisition system is used to record data from sensors and control the movement of an electric motor. The system was developed by LabVIEW and demonstrated with a model test.

The following major conclusions are drawn from this work about the behavior of this anchor concept in clay:

(1) The pitch angle at the initiation of dive can be optimized to achieve the maximum dive depth and ultimate holding capacity.

(2) The maximum depth of the dive is not strongly dependent on the undrained shear strength of the soil, while the ultimate holding capacity is proportional to the undrained shear strength of the soil at the maximum dive depth.

(3) A smaller diameter of the line makes the anchor dive deeper and increases the ultimate capacity.

(4) A deeper initial embedment depth after free fall makes the anchor dive deeper and increases the ultimate capacity.

(5) A series of model tests to calibrate the simplified predictive model for the performance of the anchor should consist of varying the thickness of the line, the depth of initial embedment, the pitch angle at the initiation of dive, and the profile of undrained shear strength versus depth.

It is recommended that model tests be conducted using the guidance presented in this thesis.

TABLE OF CONTENTS

TABLE OF CONTENTS ..... **VIII**

LIST OF TABLES ..... **XII**

LIST OF FIGURES ..... **XIII**

Chapter 1: Introduction 1

1.1 Motivation 1

1.2 Objectives 2

1.3 Organization of Thesis 4

Chapter 2: Background Information 5

2.1 Types of Drag Anchors 5

2.2 Predictive Models for Drag Anchors 7

2.2.1 Line models 7

2.2.1.1 Randolph model 7

2.2.1.2 Aubeny model 9

2.2.2 Anchor models 10

2.2.2.1 Limit equilibrium models 11

2.2.2.2 Plasticity models 12

2.2.3 Coupled anchor line and anchor models 14

2.3 Physical Model Tests for Drag Anchors 15

Chapter 3: Simplified Predictive Model 20

3.1 Line Model Module 21

3.1.1 Line model algorithm....21
3.1.2 Sensitivity study for line model....23
3.2 Dive Initiation Module....28
3.3 Trajectory Prediction Module....37
3.4 Sensitivity Analysis on A Full-scale Anchor Example....40
3.4.1 Different release angles, $\boldsymbol{\beta threshold}$....42
3.4.2 Different profiles of undrained shear strength....49
3.4.3 Different diameters of the chain....53
3.4.4 Different initial embedment depth....54
3.5 Summary of Simplified Predictive Model....56
Chapter 4: Design Plan for Experimental Tests....58
4.1 Bearing Factors....58
4.1.1 Pure normal bearing factor for the anchor....58
4.1.2 Pure shear bearing factor for the anchor....60
4.1.3 Pure moment bearing factor for the anchor....61
4.1.4 Previous tests....62
4.2 Drag Embedment Test....66
4.3 Summary of Plan for Experimental Tests....73
Chapter 5: Development of Data Acquisition System for Model Tests....74
5.1 Experimental Facilities....74
5.1.1 LVDT displacement sensors....74
5.1.2 LMT displacement sensor....76

5.1.3 Load cell....78
5.1.4 Electric motor....79
5.1.5 Magnetometer device....81
5.2 Data Acquisition and Motion Control Programs....81
5.2.1 Data Acquisition Program....82
5.2.1.1 Data Acquisition program user interface....82
5.2.1.2 Data Acquisition program Block Diagram....88
5.2.2 Motion Control program....96
5.2.2.1 Motion Control program user interface....97
5.2.2.2 Motion Control program Block Diagram....98
5.3 Demonstration of Data Acquisition and Motion Control Programs....103
5.3.1 Introduction of T-bar test....103
5.3.2 Results from T-bar tests....105
5.4 Summary of the Data Acquisition and Motion Control Programs....106
Chapter 6: Conclusion and Future Work....108
6.1 Conclusion....108
6.2 Future Work....109
APPENDICES....111
Appendix I – Spreadsheets and Program Code for Simplified Prediction Model....112
Appendix II – LabVIEW Modules....117

GLOSSARY.....129

REFERENCES.....130

VITA.....133

LIST OF TABLES

Table 2.1 Interaction factors for strip anchor with a thickness 1/7 of its width (from Aubeny and Chi 2013) 13

Table 3.1 Input parameters for prediction example 42

Table 4.1 Normalized bearing factors for original model (Ganjoo, 2010) 64

Table 4.2 Normalized bearing factors for wider model (Ganjoo, 2010) 64

Table 4.3 Normalized shear bearing factors for original model (Ganjoo, 2010) ... 64

Table 4.4 Normalized shear bearing factors for wider model (Ganjoo, 2010) 65

Table 4.5 Normalized pitch rotation factors for original model (Ganjoo, 2010) ... 65

Table 4.6 Normalized pitch rotation factors for wider model (Ganjoo, 2010) 65

Table 4.7 Proposed testing plan 68

Table 4.8 Experimental tests anchor analysis input 70

Table 4.9 Ultimate tensions in the thin and thick line conditions 72

LIST OF FIGURES

Figure 1.1 Examples of offshore facilities for energy production that utilize anchors 1

Figure 1.2 Types of anchors used for offshore production facilities (Randolph et al., 2011) 2

Figure 1.3 Concept for Flying Wing Anchor (patent pending) 3

Figure 2.1 Stevpris Mk6 drag embedment anchor (Vryhof).....5

Figure 2.2 Typical trajectory for a Drag Embedment Anchor (Byoung MIN, 2005)6

Figure 2.3 The Bruce Dennla Mk 4 Vertically Loaded Anchor (BRUCEANCHOR) 6

Figure 2.4 Inverse catenary shape of chain.....8

Figure 2.5 Force equilibrium of chain element (Neubecker and Randolph 1995) ..9

Figure 2.6 Definition sketch for Aubeny model (Aubeny and Chi 2013) 9

Figure 2.7 Free body diagram of a drag embedment anchor (Zhang et al. 2014) .12

Figure 2.8 The yield locus and plastic potential function (O'Neill et al. 2003) 14

Figure 2.9 Stage 1 and Stage 2 of VLA deployment (Aubeny and Chi, 2013) 15

Figure 2.10 Chain model tests (Neubecker and Randolph 1995) 16

Figure 2.11 Dimensions of scale model anchor and axes of motion (McCarthy 2011) 16

Figure 2.12 Test configuration for anchor model test (McCarthy 2011).....17

Figure 2.13 Comparison trajectories for thin and thick lines (McCarthy 2011)....17

Figure 2.14 Comparison trajectories for different initial pitch angles (McCarthy 2011) 18

Figure 2.15 Example model anchor drag tests in transparent soil (Deke 2011) 19

Figure 3.1 Illustration of the trajectory of a Flying Wing Anchor (patent pending)20
Figure 3.2 Definition sketch for the line model 21
Figure 3.3 Comparison profile of the line in different gradient k.....24
Figure 3.4 Comparison profile of the line in different T_a 24
Figure 3.5 Comparison profile of the line in different θ_0 25
Figure 3.6 Comparison profile of the line with different diameters 26
Figure 3.7 Comparison profile of the line in different z_a 27
Figure 3.8 Proportional relationships between T_a and T_0 in two θ_0 conditions28
Figure 3.9 Simplified representation of Flying Wing Anchor (patent pending)....29
Figure 3.10 Dive initiation process 30
Figure 3.11 Free body diagram of the anchor at initiation of pitch rotation.....31
Figure 3.12 Free body diagram of the anchor at pitch rotation 32
Figure 3.13 Free body diagram of anchor at initiation of dive 34
Figure 3.14 Yield surface drawn based on yield function (Equation 3.11) 35
Figure 3.15 An example of force (loci) moving to the yield surface.....35
Figure 3.16 Plasticity solution for Flying Wing Anchor 38
Figure 3.17 Analysis flowchart for trajectory prediction.....40
Figure 3.18 Parameters definition for trajectory program 41
Figure 3.19 Sensitivity of trajectory to Δs in catenary mooring system.....41
Figure 3.20 Relationship between $\beta_{threshold}$ and α.....43
Figure 3.21 Trajectories with different $\beta_{threshold}$ for the catenary mooring system 43
Figure 3.22 Trajectories with different $\beta_{threshold}$ for the taut mooring system.44
Figure 3.23 Component forces in vertical and horizontal directions.....45

Figure 3.24 Relationship between yield surface gradient and depth in different α ($\theta 0 = 5°$).....46
Figure 3.25 Yield surface.....47
Figure 3.26 The relationship between $\beta threshold$ and ultimate depth 48
Figure 3.27 The relationship between $\beta threshold$ and ultimate capacity 48
Figure 3.28 Trajectories of different su profiles for catenary mooring system 49
Figure 3.29 Trajectories of different su profiles for taut mooring system.....50
Figure 3.30 Trajectories of different su0 (k=0) for catenary mooring system 50
Figure 3.31 Trajectories of different su0 (k=0) for taut mooring system 51
Figure 3.32 The relationship between $su0$ and ultimate capacity.....51
Figure 3.33 The relationship between k and ultimate capacity 52
Figure 3.34 The relationship between $k$and ultimate depth.....52
Figure 3.35 Trajectories of different diameters of the chain for the catenary mooring system 53
Figure 3.36 Trajectories of different diameters of the chain for the taut mooring system 54
Figure 3.37 Trajectories of different initial embedment depths for the catenary mooring system 55
Figure 3.38 Trajectories of different initial embedment depths for taut mooring system 55
Figure 3.39 The relationship between initial embedment depth and ultimate capacity 56
Figure 4.1 Test configuration for measuring the pure normal bearing factor.....59
Figure 4.2 Test configuration for measuring the pure shear bearing factor.....60

Figure 4.3 Test configuration for measuring the pure moment bearing factor 61
Figure 4.4 Two anchor models used by Ganjoo (2011).....63
Figure 4.5 Example of a drag embedment test in 12-foot thermo-plastic tank.....66
Figure 4.6 Example of drawing yield interaction surface.....67
Figure 4.7 Trajectories of different fluke areas with 1/8 inch diameter line 71
Figure 4.8 Trajectories of different fluke areas with 13/38 inch diameter line 71
Figure 4.9 Comparison of trajectories with different α in thick line 73
Figure 5.1 Linear Variable Displacement Transducer sensor.....74
Figure 5.2 Output data of LVDT and load cell in a monotonic pile test 75
Figure 5.3 Linear Motion Transducer sensor.....76
Figure 5.4 Output data of LMT and load cell in a Gulf of Mexico soil test 77
Figure 5.5 Load cell 78
Figure 5.6 Electric motor system 80
Figure 5.7 Magnetometer sensor system (McCarthy, 2011).....81
Figure 5.8 Data acquisition and motion control system 82
Figure 5.9 Data Acquisition hardware 83
Figure 5.10 User interface of Data Acquisition program 83
Figure 5.11 Buttons and indicator light used in DAQ user interface 84
Figure 5.12 Calibration factors input area 85
Figure 5.13 Load, LVDT, and LMT output area 86
Figure 5.14 LOAD-LVDT and LOAD-LMT output area 87
Figure 5.15 Motion Raw Read.....87
Figure 5.16 Data Producer loop 90
Figure 5.17 DAQ Assistant user interface 91

Figure 5.18 Channels connections 92
Figure 5.19 Calibration procedures....93
Figure 5.20 Chart Output section....94
Figure 5.21 Writing Data to File section 95
Figure 5.22 Flow chart of motion control program 96
Figure 5.23 Motion Control user interface 97
Figure 5.24 Decision Phase....98
Figure 5.25 Input Parameters Phase....100
Figure 5.26 Data Consumer section....101
Figure 5.27 Check Movement section 102
Figure 5.28 Stop Phase 103
Figure 5.29 T-bar test....104
Figure 5.30 Sensitivity test on Golf of Mexico soil....106

Chapter 1: Introduction

1.1 MOTIVATION

Anchors provide the foundation for a variety of offshore facilities that produce energy (Figure 1.1). Existing anchors consist of driven or drilled and grouted piles, suction caissons, drag anchors, suction embedded plate anchors, and dynamically penetrating anchors (Figure 1.2).

Figure 1.1 Examples of offshore facilities for energy production that utilize anchors

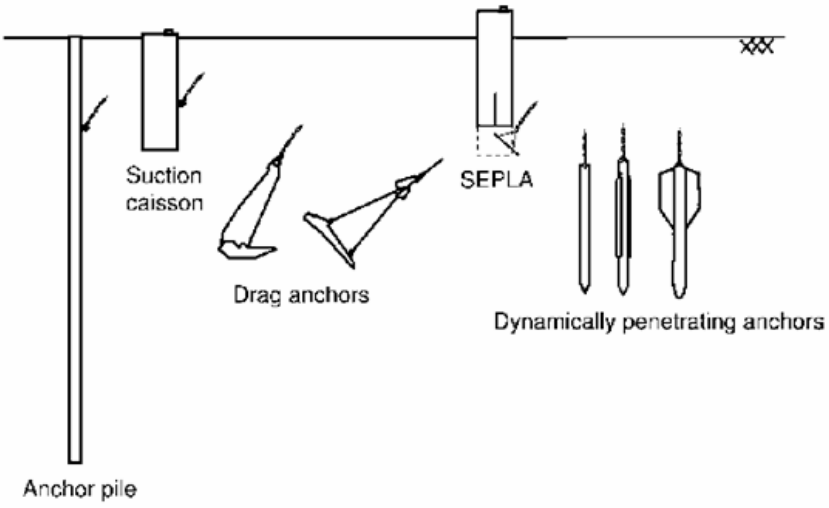

Figure 1.2 Types of anchors used for offshore production facilities (Randolph et al., 2011)

A new anchor concept, called the Flying Wing Anchor (patent pending), is currently being developed at The University of Texas at Austin (Figure 1.3). This anchor combines beneficial aspects of dynamically penetrating anchors, drag embedment anchors and plate anchors in an attempt to provide an effective and efficient anchor. Since this concept is new, it needs to be proven and optimized using physical model tests.

1.2 OBJECTIVES

The goal of this study is to develop a plan for conducting model tests on a new anchor concept, the Flying Wing Anchor. The objectives of this work are as follows:

1. Develop a simplified analytical model to predict the trajectory and capacity of the anchor when it is pulled (dragged) through the soil by the anchor line.
2. Use the simplified analytical model to establish properties for the model anchor, anchor line and the soil test bed.
3. Create a data acquisition system to conduct model tests.

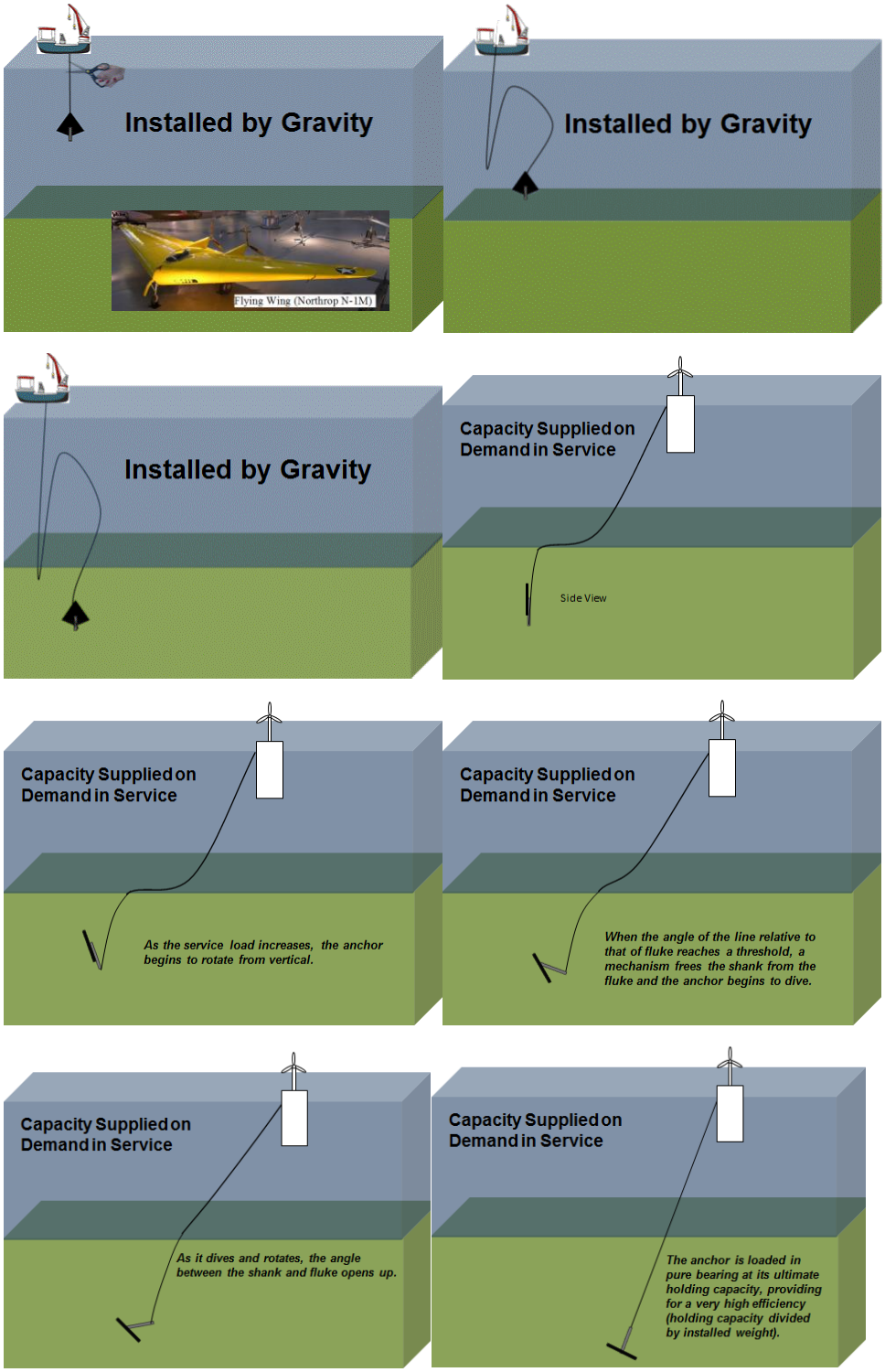

Figure 1.3 Concept for Flying Wing Anchor (patent pending)

1.3 ORGANIZATION OF THESIS

This thesis consists of six chapters, including this introduction chapter. Chapter 2 is background information on offshore anchors. Chapter 3 describes the development of a simplified analytical model to predict the trajectory and capacity of the anchor when it is pulled through the soil by the anchor line. Chapter 4 presents a plan for conducting model tests, including target properties for the model anchor, anchor line and the soil test bed. Chapter 5 describes the development of a data acquisition system for conducting model tests. Chapter 6 presents the conclusions of this study and recommendations for future work.

Chapter 2: Background Information

In this chapter, we summarize information about existing drag anchors.

2.1 Types of Drag Anchors

Drag anchors for energy production facilities evolved from the anchors used for ships. There are two main types of the drag anchors: Drag Embedment Anchor (DEA) and Vertically Loaded Anchor (VLA).

Drag Embedment Anchors consist of a fluke and a shank (Figure 2.1). The angle between the fluke and the shank is fixed at typically about $30°$ for anchors in sand and $50°$ for anchors in clay (Randolph and Susan 2011). The anchor is set down on the sea floor with the shank horizontal, and then it is dragged into the soil as tension is placed on the anchor line (Figure 2.2). Being dragged through a distance of 10 to 20 times the fluke length, Drag Embedment Anchors are typically able to dive from one to five fluke lengths below the mudline and mobilize a holding capacity of 20 to 50 times the anchor weight. Drag Embedment Anchors are typically used with catenary mooring systems where the anchor line is near horizontal on the sea floor under design loading conditions (Randolph and Susan 2011).

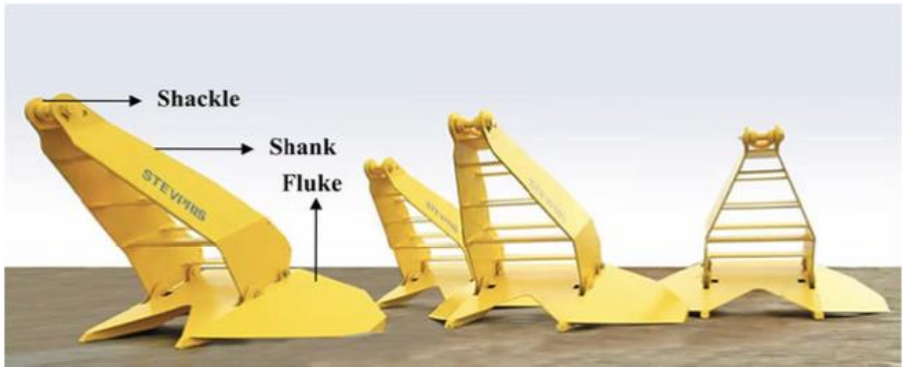

Figure 2.1 Stevpris Mk6 drag embedment anchor (Vryhof)

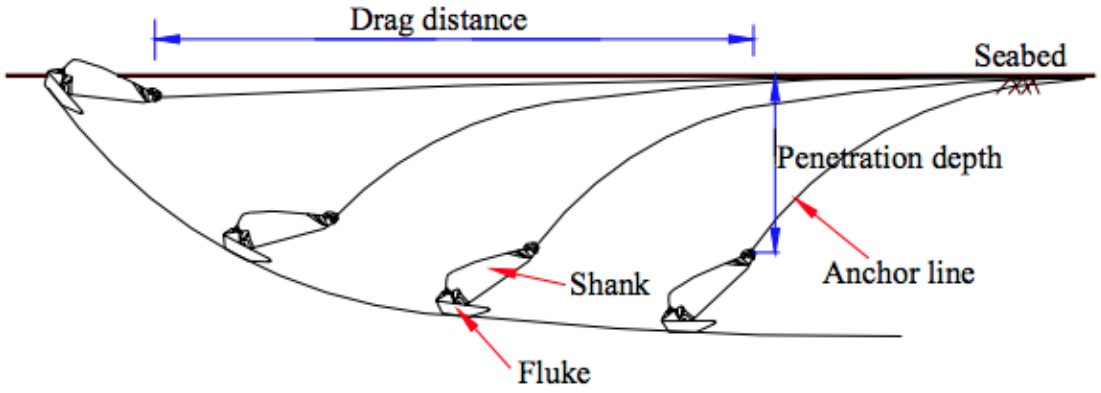

Figure 2.2 Typical trajectory for a Drag Embedment Anchor (Byoung MIN, 2005)

With a Vertically Loaded Anchor, the angle between the shank and fluke is initially fixed during diving like a Drag Embedment Anchor and then manually released so that the anchor line is pulling near normal to the fluke under design loading conditions (Figure 2.3). Vertically Loaded Anchors are typically used for semi-taut and taut mooring systems where the anchor line is angled at 20 to 40 degrees from the horizontal at the sea floor (Randolph and Susan 2011).

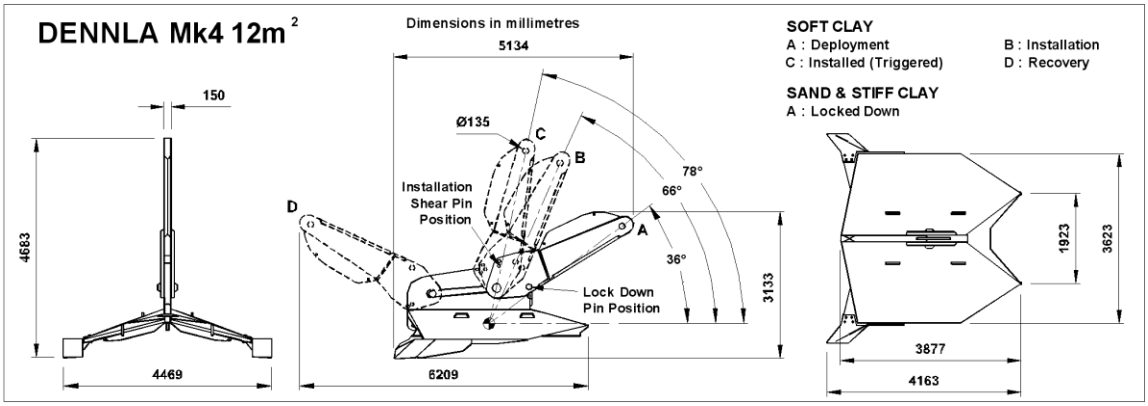

Figure 2.3 The Bruce Dennla Mk 4 Vertically Loaded Anchor (BRUCEANCHOR)

2.2 PREDICTIVE MODELS FOR DRAG ANCHORS

Predictive models have been developed for the anchor line, for the anchor and for coupling the anchor line and the anchor during dive in clays.

2.2.1 Line models

2.2.1.1 Randolph model

Neubecker and Randolph (1995) developed a series of equations to produce expressions for the force distribution and the geometric profile along the anchor line or chain (Figure 2.4). The line was connected with a foundation at a depth D. At the connecting point, θ_a was the angle between the chain and horizontal and T_a was the tension force applied on the connection. The shape of the chain was inverse catenary. At the mudline, θ_0 was the chain inclination and T_0 was the tension force. Neubecker and Randolph (1995) assumed θ_0 equaled zero or a small value during drag, like for a catenary mooring system. The bearing resistance force, normal to the chain, was Q per unit length. The friction force parallel to the chain was F per unit length, where $F = \mu Q$ with a friction coefficient μ that is typically between 0.4 and 0.6 (Neubecker and Randolph 1995).

The equations they developed based on force equilibrium (Figure 2.5 to relate T_a, θ_a, and θ_0 were the following:

$$\frac{T_a}{2}(\theta_a^2 - \theta_0^2) = D\bar{Q} \qquad (Equation\ 2.1)$$

$$Q = bq = bN_cS_u \qquad (Equation\ 2.2)$$

where: $b = E_n d_b$ where $E_n = 1$ for wire and $E_n = 2.5$ for chain and d_b = diameter of the tension line or chain link

N_c = bearing factor for anchor line (5.1 at the mudline increasing linearly with depth to a constant value of 7.6 below a depth of $z_{break} = 2.4E_n d$)

S_u= undrained shear strength of soil (either a constant with depth or linearly increasing with depth)

$\bar{Q}$ = average bearing resistance over the depth range $0 \leq z \leq D$

Changing the forms of Equation (2.1) and Equation (2.2), Neubecker and Randolph (1995) obtained the following equations:

$$\theta_a = \sqrt{\frac{2D\bar{Q}}{T_a}} = \sqrt{\frac{2}{T^*}} \qquad (Equation\ 2.3)$$

$$\frac{T_0}{T_a} = e^{\mu\theta_a} \qquad (Equation\ 2.4)$$

where T^* is a normalized chain tension, $T^* = T_a/D\bar{Q}$.

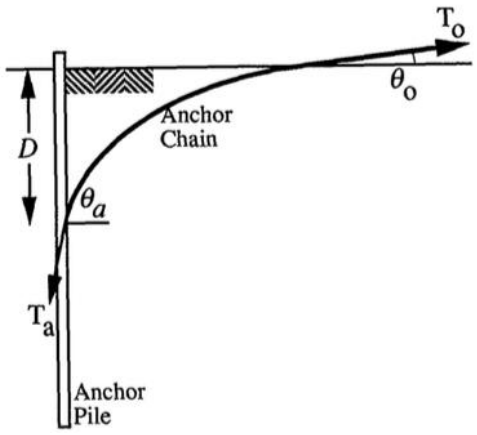

Figure 2.4 Inverse catenary shape of chain

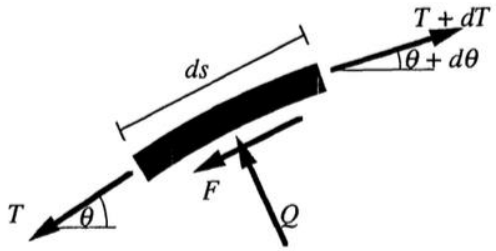

Figure 2.5 Force equilibrium of chain element (Neubecker and Randolph 1995)

This solution ignored the weight of the chain but can be readily modified to account for it in soft soils where it plays a role (Neubecker and Randolph 1995).

2.2.1.2 Aubeny model

Aubeny and Chi (2013) extended the Randolph model to account for a general undrained strength that has an intercept at the mudline and increases linearly with depth below the mudline (Figure 2.6).

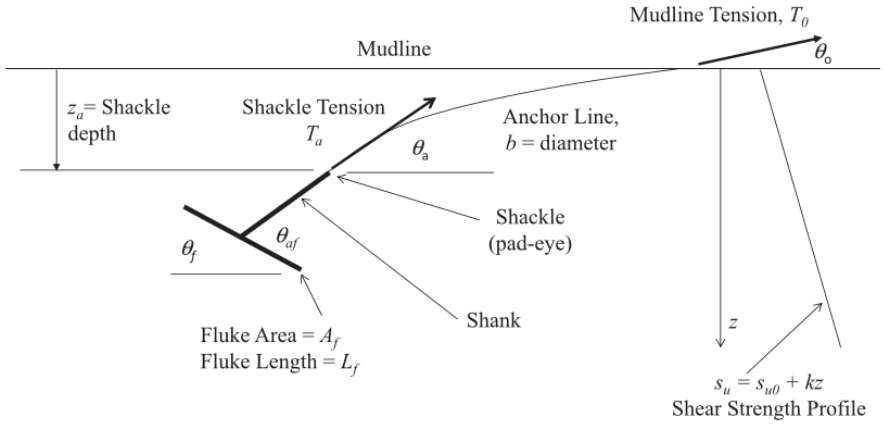

Figure 2.6 Definition sketch for Aubeny model (Aubeny and Chi 2013)

The solution was expressed as the profile of the line in the soil for a given tension T_a at the padeye and angle θ_0 at the mudline. The equation was shown below is as follows:

$$x^* = \sqrt{\frac{1}{2Q_2}} \ln \left[\frac{Q_2 + \frac{Q_1}{2} + \sqrt{Q_2^2 + Q_1 Q_2 + \frac{Q_2 \theta_0^2}{2}}}{Q_2 z^2 + \frac{Q_1}{2} + \sqrt{Q_2^2 (z^*)^2 + Q_1 Q_2 z^* + \frac{Q_2 \theta_0^2}{2}}} \right] \qquad Equation\ (2.5)$$

where: x^* = normalized horizontal coordinate = x/z_a;

z^* = normalized vertical coordinate = z/z_a;

Q_1 = normalized soil resistance due to mudline strength = $E_n N_c S_{u0} z_a / T_a$;

Q_2 = normalized soil resistance due to strength gradient = $E_n N_c b k z_a^2 / 2T_a$;

z_a = depth of padeye below mudline;

x = horizontal coordinate;

z = vertical coordinate;

E_n = chain multiplier;

N_c = bearing factor for anchor line;

b = anchor line diameter;

S_{u0} = soil strength at mudline;

k = soil strength gradient;

T_a = anchor-line tension at padeye; and

θ_0 = angle between line and horizontal at mudline.

2.2.2 Anchor models

Both limit equilibrium and plasticity-based solutions have been developed for anchors during drag.

2.2.2.1 Limit equilibrium models

There are numerous limit equilibrium models that have been developed for drag anchors in clay (e.g., Stewart 1992). An example of a recent model is by Zhang et al. (2014) (Figure 2.7). They derive the following equations to calculate the bearing and shear forces:

$$T_a = \frac{1}{\cos(\theta_a - \theta_m)}[F_b + F_s - Wsin(\theta_0 - \theta_m)] \qquad Equation\ (2.6)$$

$$F_b = N_p S_u A_b \qquad Equation\ (2.7)$$

$$F_s = N_s S_u A_s \qquad Equation\ (2.8)$$

Where: θ_a = drag angle to the top surface of the fluke at the padeye

θ_0 = fluke orientation to the horizontal

θ_m = angle of the movement direction to the top surface of the fluke

F_b and F_s = total end bearing and total shear force in the movement direction on the angle

W = submerged anchor weight

N_p = bearing capacity factor for the anchor

N_s = shear capacity factor for the anchor

A_b = effective bearing area of the anchor

A_s = effective shear area of the anchor

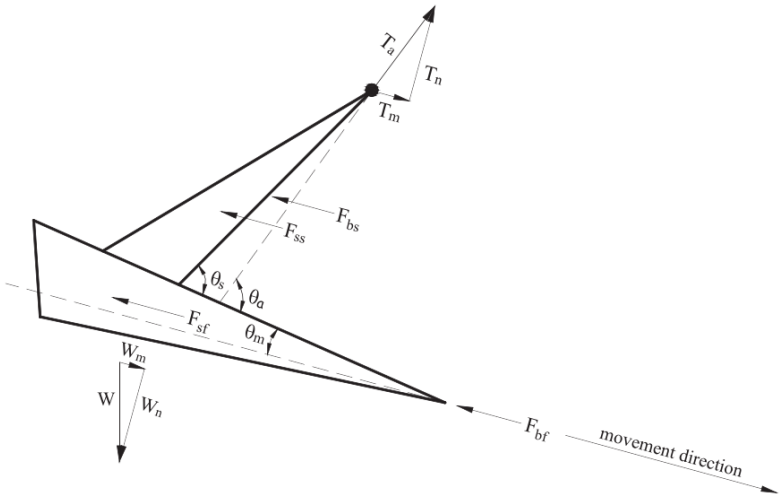

Figure 2.7 Free body diagram of a drag embedment anchor (Zhang et al. 2014)

2.2.2.2 Plasticity models

O'Neill et al. (2003) proposed a plasticity-based solution to model the interaction between anchor and clay during drag. The solution produced an associated plastic failure locus for combined loading conditions. The locus for a rectangular fluke could be reasonably approximated as a mathematical function of bearing capacity to a normal load V, a shear load H, and a pitch moment M:

$$f = \left(\frac{V}{V_{max}}\right)^{q} + \left[\left(\frac{M}{M_{max}}\right)^{m} + \left(\frac{H}{H_{max}}\right)^{n}\right]^{\frac{1}{p}} - 1 = 0 \quad Equation\ (2.9)$$

Where V_{max}, M_{max}, and H_{max} are the capacities in pure loading and n, m, p, and q are interaction coefficients determined from finite element analyses (e.g., Table 2.1).

Interaction factor	Yang et al. (2010)	Elkhatib and Randolph (2005)	Bransby and O'Neill (1999)
m	1.56	2.58	1.26
n	4.19	3.74	3.72
p	1.57	1.09	1.09
q	4.43	1.74	3.16

Table 2.1 Interaction factors for strip anchor with a thickness 1/7 of its width (from Aubeny and Chi 2013)

In order to calculate the normal δv, parallel δh, and rotational $\delta\beta$ movements of the anchor as it moves through the soil, O'Neill et al. (2003) proposed establishing the plastic movement from the yield locus (Figure 2.8). If there is no applied moment (as in the case of the Flying Wing Anchor), then the yield locus is two-dimensional and the normal to the yield surface governs the ratio of δh and δv at failure:

$$\frac{\delta v}{\delta h} = \frac{\frac{\delta f}{\delta V}}{\frac{\delta f}{\delta H}} \qquad Equation\ (2.10)$$

where: δv = plastic normal displacement of the anchor at failure; δh = plastic parallel displacement of the anchor at failure; and $f = f(V, H) = 0$ is the yield surface. Gilbert et al. (2009) and Aubeny et al. (2011) extended this approach to square plates and to shapes similar to drag anchors.

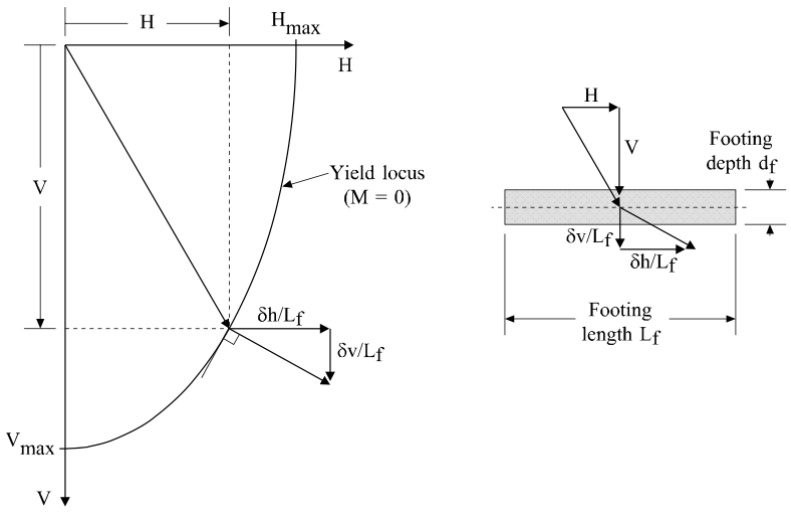

Figure 2.8 The yield locus and plastic potential function (O'Neill et al. 2003)

2.2.3 Coupled anchor line and anchor models

The most commonly used commercial model for coupling the anchor line and the anchor behavior during drag is called DIGIN (e.g., Eklund and Strom 1998 and Dahlberg 1998); however, this model is proprietary and the details of the model have not been published. Aubeny and Chi (2010), Aubeny et al. (2011) and Aubeny and Chi (2013) have developed plasticity-based models that couple the line catenary model (Equation 2.5) and the anchor displacement model (Equations 2.9 and 2.10). An example of this coupling is for a Vertically Loaded Anchor (Figure 2.9): (Stage 1) Drag embedment with shank fixed to fluke and (Stage 2) Normal loading with shank released from fluke. The recursive algorithm they implemented to couple the anchor line and anchor during drag embedment (Stage 1) was the following:

1) For the current line-fluke angle θ_{af} and bearing factors (N_n, N_m, N_t), the ratio of anchor rotation to tangential translation ($R_{rt} = \beta L_f / v_t$) and the ratio of normal to tangential motion ($R_{nt} = v_n / v_t$) were calculated.
2) A distance Δs parallel to the fluke was assumed and the horizontal and vertical increment were computed from it:

$$\Delta x = \Delta s\left(cos\theta_f + R_{nt}sin\theta_f\right) \qquad Equation\ (2.18)$$

$$\Delta z = \Delta s\left(sin\theta_f + R_{nt}cos\theta_f\right) \qquad Equation\ (2.19)$$

3) The change of the line-padeye angle $\Delta\theta_a$ was calculated from R_{nt}.
4) The location (coordinates x and z) and the orientation (θ_a) of the anchor were updated.
5) The soil strength was updated with the new location.
6) The anchor-line tension T_a was updated with the new soil strength and bearing factors.
7) Steps 1-6 were repeated to obtain the desired drag distance or depth of embedment.

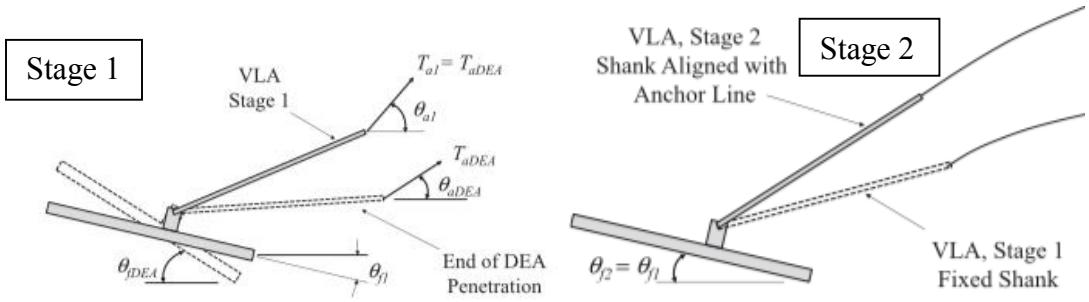

Figure 2.9 Stage 1 and Stage 2 of VLA deployment (Aubeny and Chi, 2013)

2.3 PHYSICAL MODEL TESTS FOR DRAG ANCHORS

Physical model tests have been conducted with anchor lines and drag anchors in clay to calibrate predictive models. Neubecker and Randolph (1995) investigated their predictive model for the anchor line tests performed by Degenkamp and Dutta (1989) (Figure 2.10). Aubeny et al. (2011) and McCarthy (2011) conducted model-scale tests in test beds of clay using a magnetometer to track the location and orientation of the anchor during drag (Figures 2.11 to 2.14). Deke (2011) conducted model anchor drag tests in a transparent soil, laponite, in order to track the location and orientation of the anchor (Figure 2.15). Large-scale anchor tests were described by Aubeny et al. 2013 to compare with prediction results (Figure 2.16).

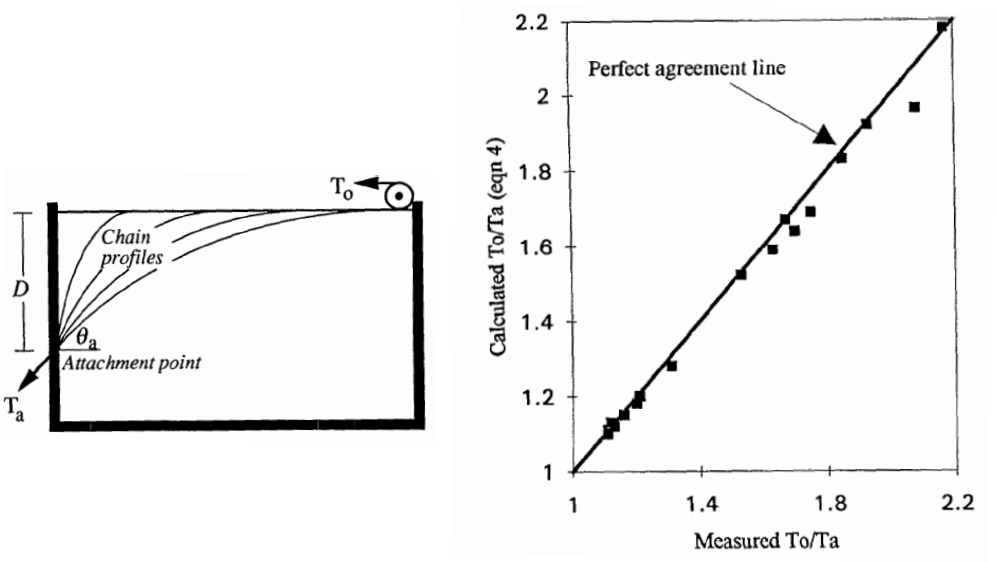

Figure 2.10 Chain model tests (Neubecker and Randolph 1995)

.

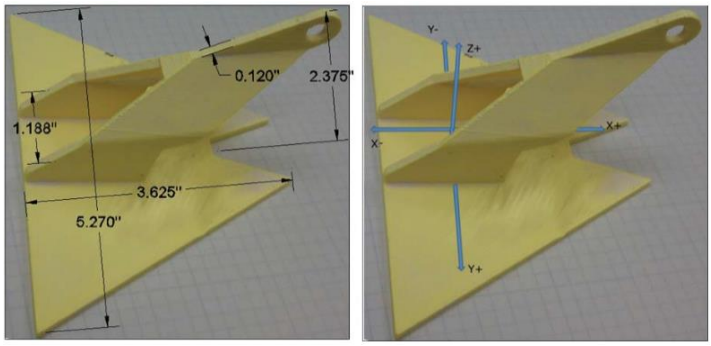

Figure 2.11 Dimensions of scale model anchor and axes of motion (McCarthy 2011)

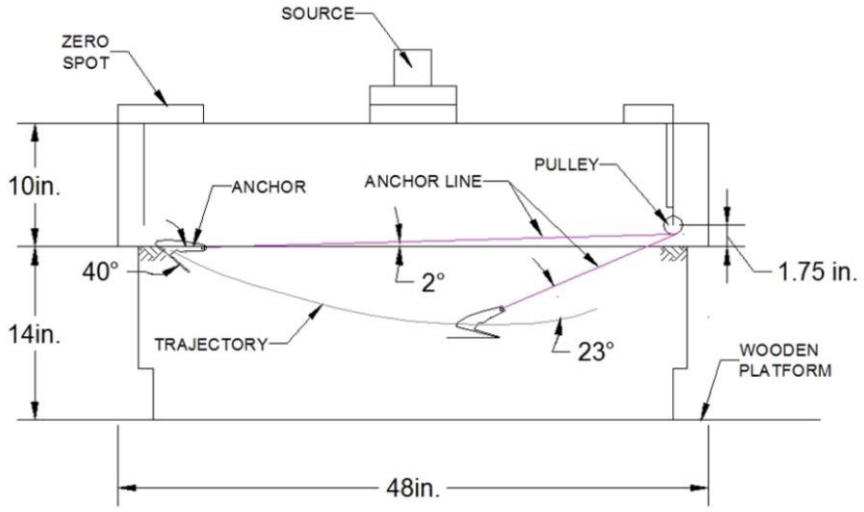

Figure 2.12 Test configuration for anchor model test (McCarthy 2011)

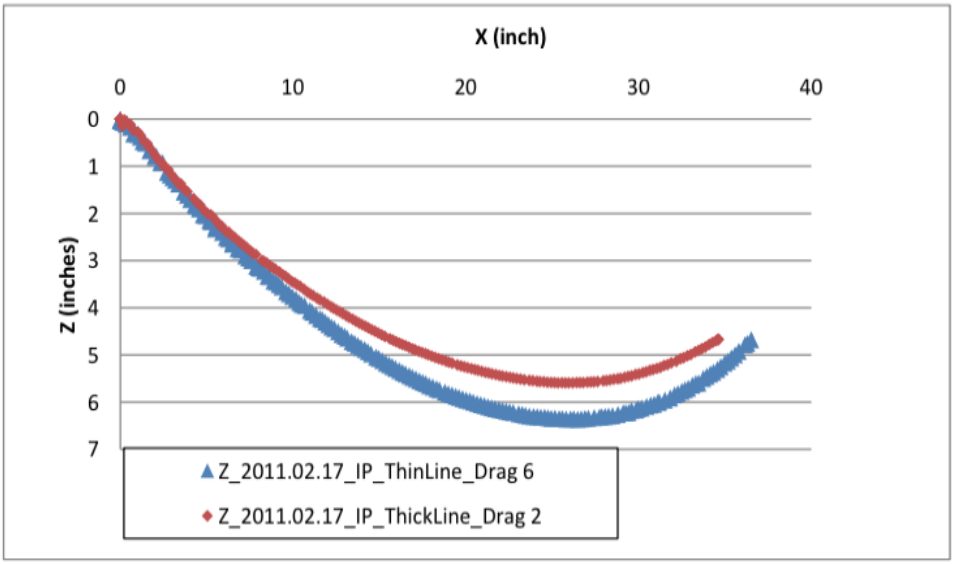

Figure 2.13 Comparison trajectories for thin and thick lines (McCarthy 2011)

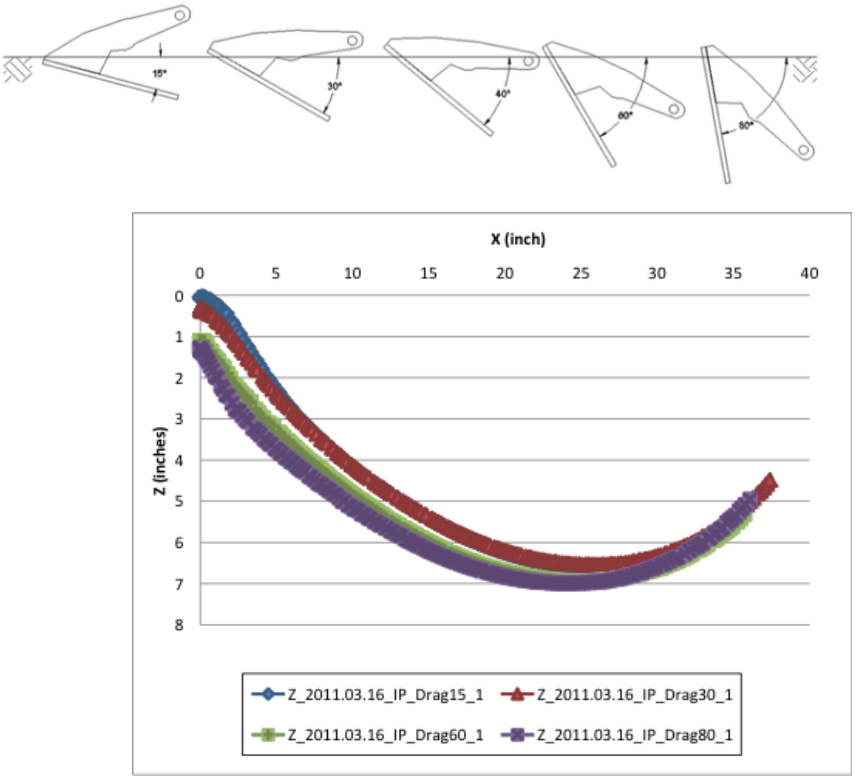

Figure 2.14 Comparison trajectories for different initial pitch angles (McCarthy 2011)

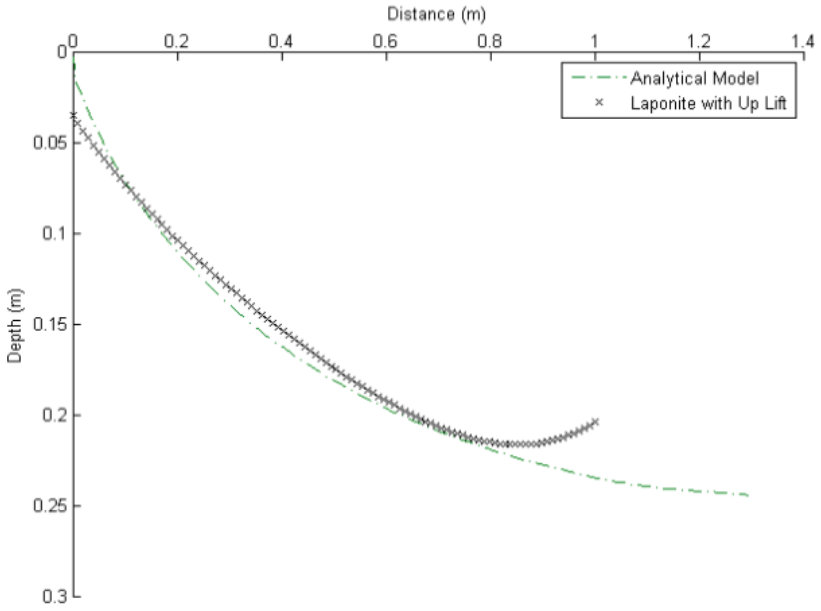

Figure 2.15 Example model anchor drag tests in transparent soil (Deke 2011)

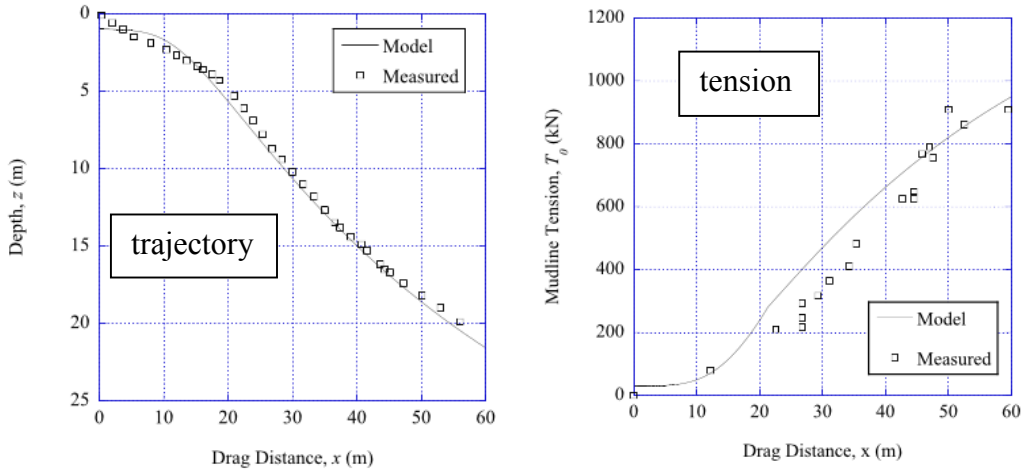

Figure 2.16 South Timbalier DENNLA tests: trajectory and line tension (Aubeny and Chi 2013)

Chapter 3: Simplified Predictive Model

The first part of this chapter describes a procedure to develop a numerical model for predicting the trajectory of the new anchor after it has penetrated after free fall (Figure 3.1). The numerical model consists of two components: (1) a line model describing the shape of the line in the function of the tension in line and the strength of the soil and (2) a plasticity solution describing the rotation of the anchor (dive initiation) and the normal and shear displacements (dive trajectory) as a function of the anchor line tension. The individual components are first described and the methodology for coupling them is presented. The detailed codes for the simplified predictive model are provided in Appendix I.

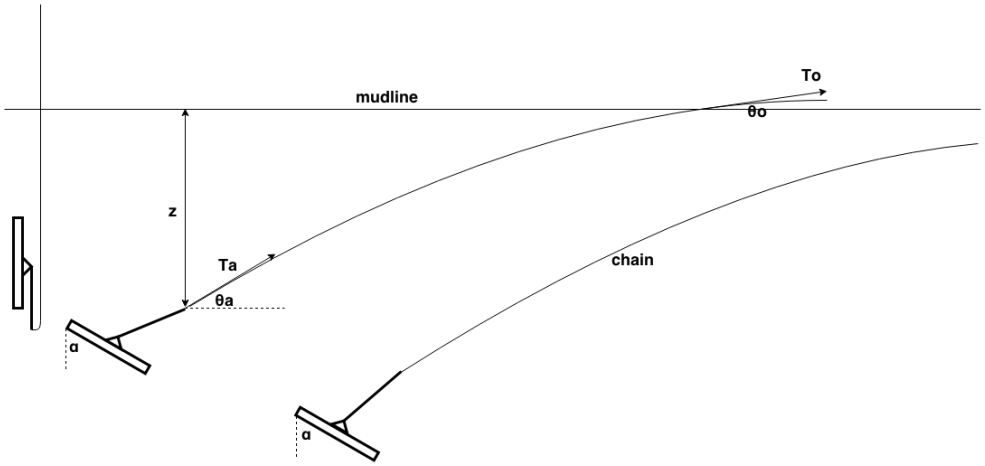

Figure 3.1 Illustration of the trajectory of a Flying Wing Anchor (patent pending)

The second part of this chapter investigates the sensitivity of the anchor trajectory to the parameters in the simplified predictive model. There are four influencing factors we are interested in: (1) the angle at which the shank is released from the fluke and the anchor transitions from pitch rotation to dive translation; (2) the profile of undrained shear strength versus depth for the clay; (3) the diameter of the anchor line or chain; and (4) the depth of initial embedment of the anchor after free fall.

3.1 LINE MODEL MODULE

3.1.1 Line model algorithm

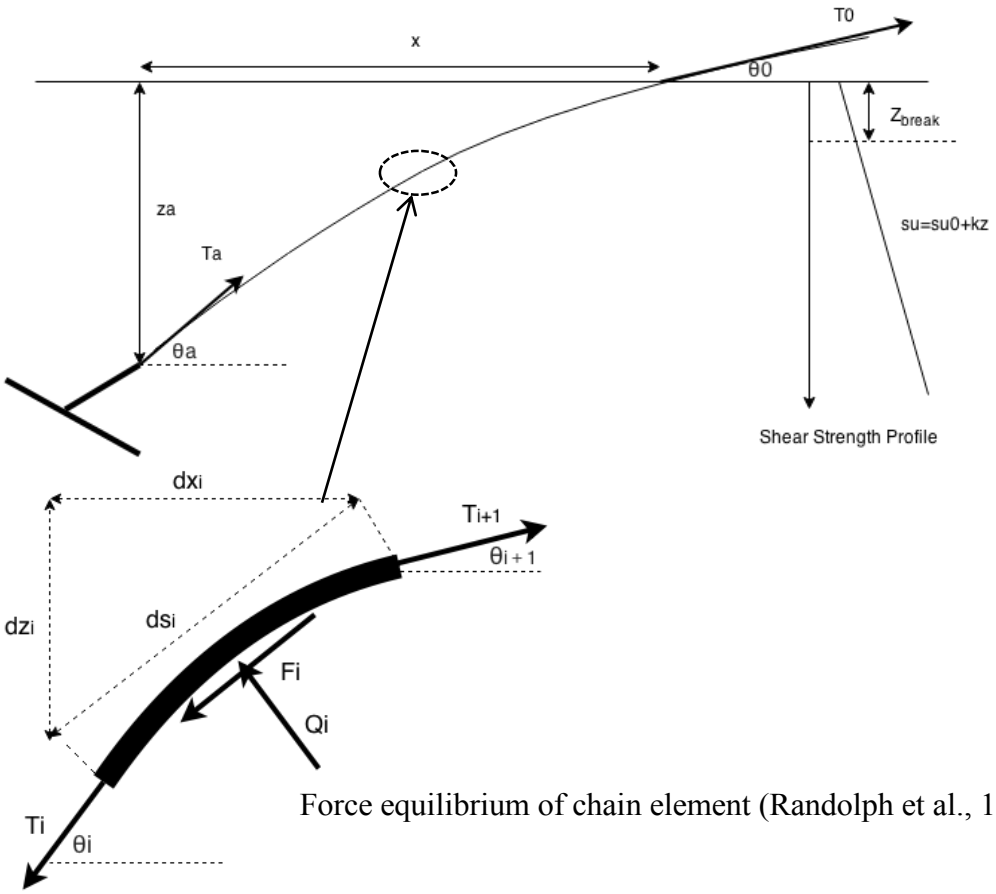

Force equilibrium of chain element (Randolph et al., 1995)

Figure 3.2 Definition sketch for the line model

The line model in this study (Figure 3.2) is based on the Aubeny model, which provides the profile of the line in the soil for a specified angle at the mudline, θ_0, and tension at the padeye, T_0. To calculate the angle of the line at the padeye, θ_a, and the tension in the line at the mudline, T_0, in the line at mudline, a finite difference algortihm was developed based on limit equilibrium (Figure 3.2). The number of the elements is n.

Solving the equilibrium of the element i in Figure 3.2, the following equations are obtained:

$$ds = \sqrt{dx^2 + dz^2} \qquad Equation\ (3.1)$$

$$Q_i = N_c S_u b * ds \qquad Equation\ (3.2)$$

$$F_i = Q_i * \mu \qquad Equation\ (3.3)$$

$$T_{i+1} = T_i + F_i \qquad Equation\ (3.4)$$

$$\theta_a = \text{atan}\left(\frac{dz_1}{dx_1}\right) \qquad Equation\ (3.5)$$

$$T_0 = T_a + \sum_{i=1}^{n} F_i \qquad Equation\ (3.6)$$

These equations assume that $d\theta$ $(d\theta = \theta_i - \theta_{i+1})$ is small enough so that the orientations of T_{i+1}, T_i, and F_i are on the same line and all perpendicular to Q_i.

The input parameters to the line model algorithm are: (1) the type of the line (wire or chain), (2) the bearing capacity of the line N_c, (3) the diameter of the line d, (4) the profile of the soil (su_0 and gradient k) , (5) the depth of the bearing capacity meeting the maximum value z_{break}, (6) the depth of the padeye z_a, (7) the tension at the padeye T_a, (8) the angle at the mudline θ_0, and (9) the friction coefficient μ. Using these input parameters, the following results are calculated: (1) the shape of the line; (2) the tension at the mudline T_0; (3) the angle at the padeye θ_a.

The profile of the line is computed by the following algorithm:

1) The padeye depth z_a is divided into n equivalent increments $\Delta z = z_a/n$.

2) n+1 depth elements are generated by the increment, the first element is $z_0 = 0$, the second element is $z_1 = z_0 + \Delta z$, and the third element is $z_2 = z_1 + \Delta z$. Following the generation rule, $z_i = z_{i-1} + \Delta z$ until $z_n = z_a$.
3) Each z_i is transformed to $z_i^* = z_i / z_a$.
4) The normalized soil resistances are calculated: $Q_1 = E_n N_c s u_o z_a / T_a$ and $Q_2 = E_n N_c d k z_a^2 / 2T_a$ where N_c is depends on the depth.
5) Each x_i^* is calculated by Equation (2.5) for each z_i^*.
6) Each x_i^* is transformed to $x_i = z_a x_i^*$.

The angle at the padeye θ_a and the tension of the line T_0 at the mudline are then calculated by the following algorithm:

1) n length elements are generated by the n+1 depth elements, the first element is $l_1 = \sqrt{\Delta z^2 + (x_1 - x_0)^2}$, the second element is $l_2 = \sqrt{\Delta z^2 + (x_2 - x_1)^2}$. Following the generation rule is applied, $l_i = \sqrt{\Delta z^2 + (x_i - x_{i-1})^2}$, until i equals to n.
2) The soil force Q_i applied on the l_i element is calculated by Equation (3.2).
3) The friction force F_i generated by the soil force Q_i is calculated by Equation (3.3).
4) The tension in the line at the muddling is calculated from Equation (3.6).
5) The angle of the line at the padeye is calculated from $\theta_a = \text{asin}\left(\frac{\Delta z}{l_n}\right)$ since the nth element is the element attached on the padeye.

3.1.2 Sensitivity study for line model

This section studies trajectory changes with the shear strength profile, the tension and angle at the mudline, the diameter of the line, and the depth of embedment. We divide the line into 100 elements.

1) To study the sensitivity of shear strength profile, we use the gradient k as 0, 8, and 16 Kpa/m. Figure 3.3 shows that with the increase of the gradient k the catenary of the line increases.

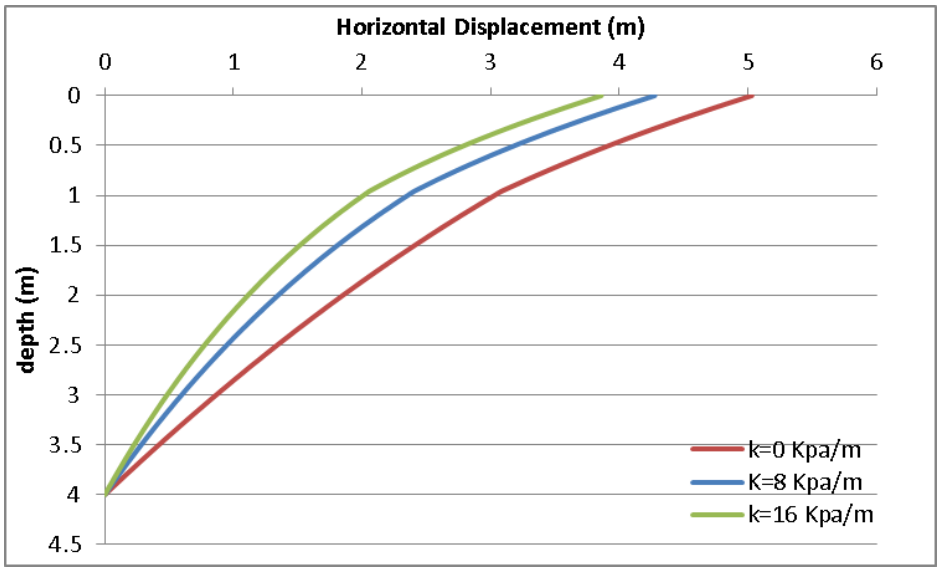

Figure 3.3 Comparison profile of the line in different gradient k

2) To study the sensitivity of the tension at the padeye, we use T_a values of 100, 200, 400, 800, and 1600 KN. Figure 3.4 shows that the tension at the padeye T_a reduces the catenary the line becomes more taut.

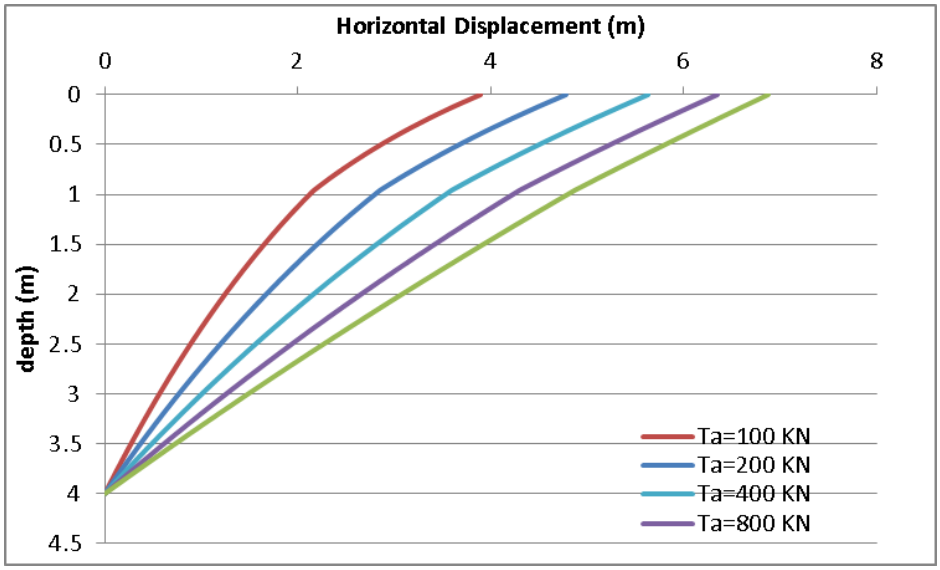

Figure 3.4 Comparison profile of the line in different T_a

3) To investigate the influence of the angle at the mudline θ_0, we use θ_0 equal to 5, 10, and 30 degrees. Figure 3.5 shows that increasing the angle at the mudline θ_0 reduces the catenary for the same line tension.

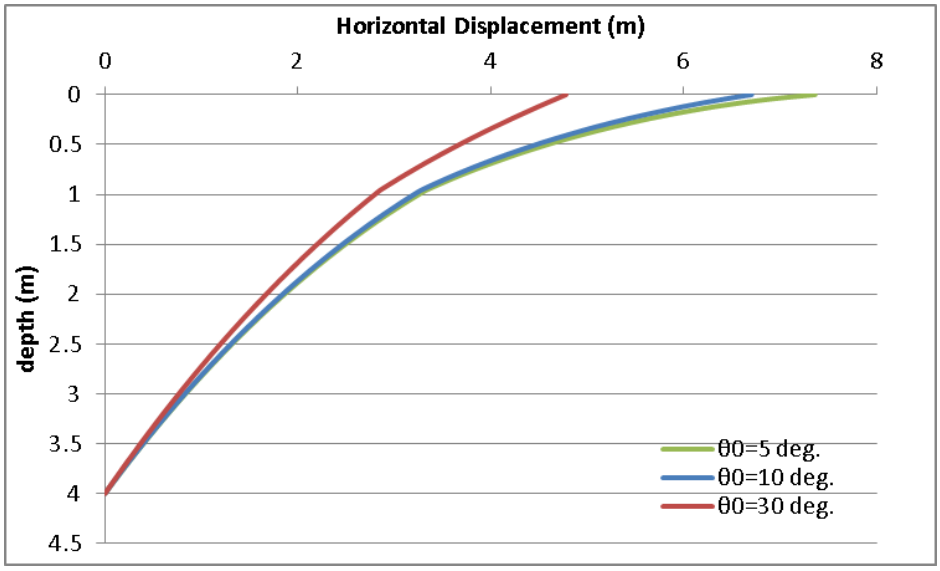

Figure 3.5 Comparison profile of the line in different θ_0

4) We change the diameter d to equal 0.1, 0.2, and 0.4 meters to study the influence of the diameter of the line. Figure 3.6 shows with the increase of the diameter of the line d, the catenary increases.

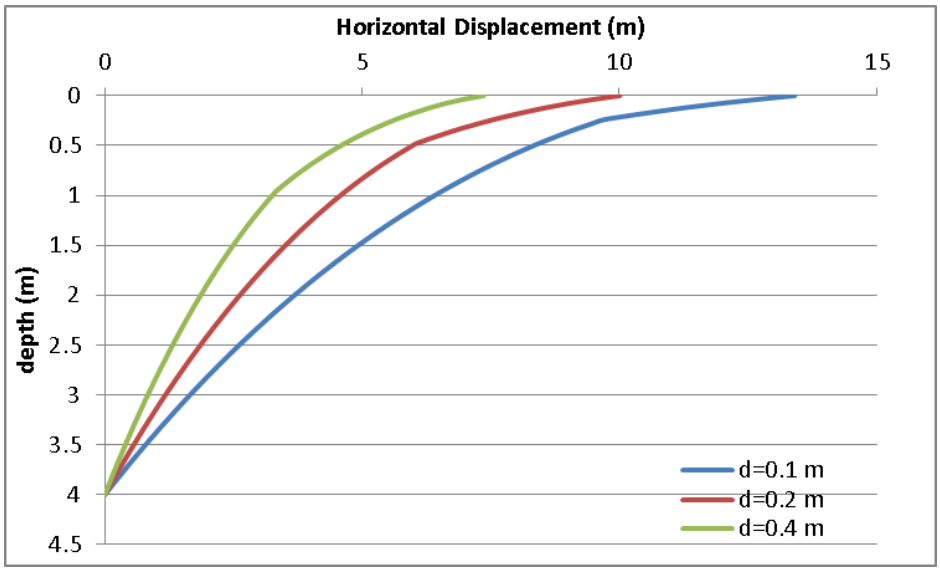

Figure 3.6 Comparison profile of the line with different diameters

5) We change the padeye embedment depth z_a to be 2, 4, and 8 meters to study its influence. Figure 3.7 shows with the increase of the z_a, the catenary of the line increases and the angle of the line at the padeye increases for the same line tension.

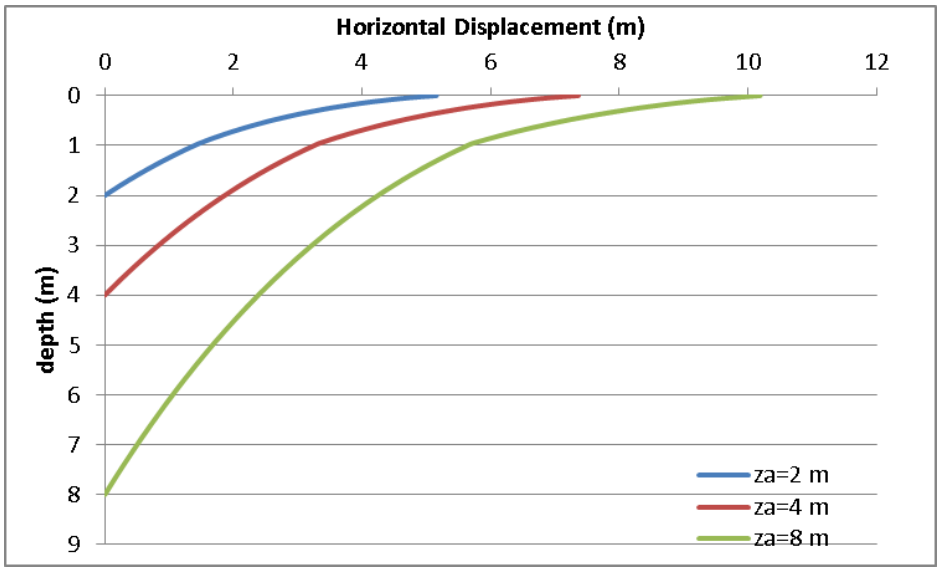

Figure 3.7 Comparison profile of the line in different z_a

6) We study how the tension at the mudline T_0 increases with the tension at the padeye T_a in two different mudline angle θ_0 conditions. Figure 3.8 shows that the tension at the padeye is essentially proportional to that at the mudline, and that it increases faster with increasing tension at the mudline when the angle at the mudline is flatter.

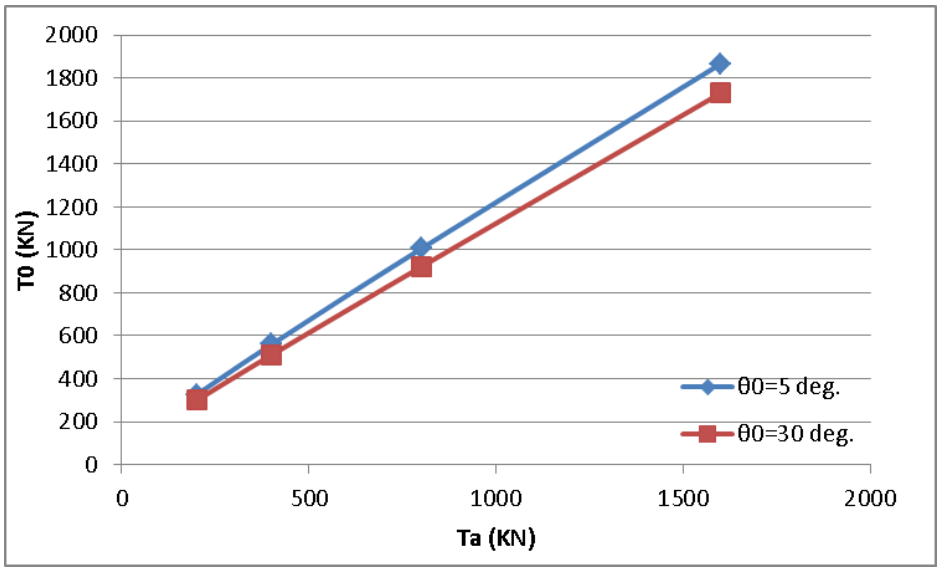

Figure 3.8 Proportional relationships between T_a and T_0 in two θ_0 conditions

3.2 Dive Initiation Module

A simplified representation of the Flying Wing Anchor with definitions is presented by Figure 3.9: α is the angle between the fluke and the vertical direction; L is the length of the fluke; the area of the fluke is A; e is the length of the shank; z_a is the depth of the padeye from the mudline; β is the angle between the line and the direction perpendicular to the fluke; and θ_a is the angle between the line and the horizontal. In modeling the anchor, we assume that the hinge between the shank and fluke is at the center of the fluke so that there is no moment applied when the shank is released and the bearing resistance of the shank to rotation is negligible because its bearing area is much smaller than the fluke.

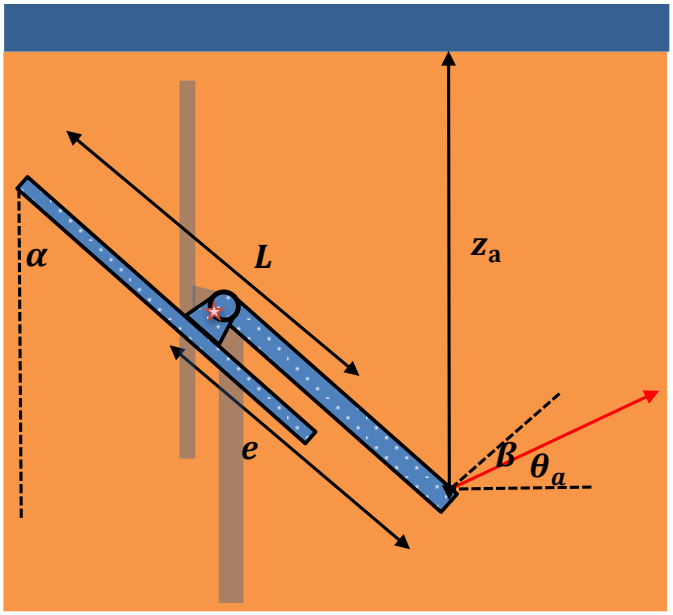

Figure 3.9 Simplified representation of Flying Wing Anchor (patent pending)

The dive initiation sequence consists of the following steps: (1) pitch rotation of the anchor with the shank attached to the fluke; (2) release of the shank from the fluke when a threshold angle between the line and the fluke is exceeded; and (3) initiation of dive (Figure 3.10).

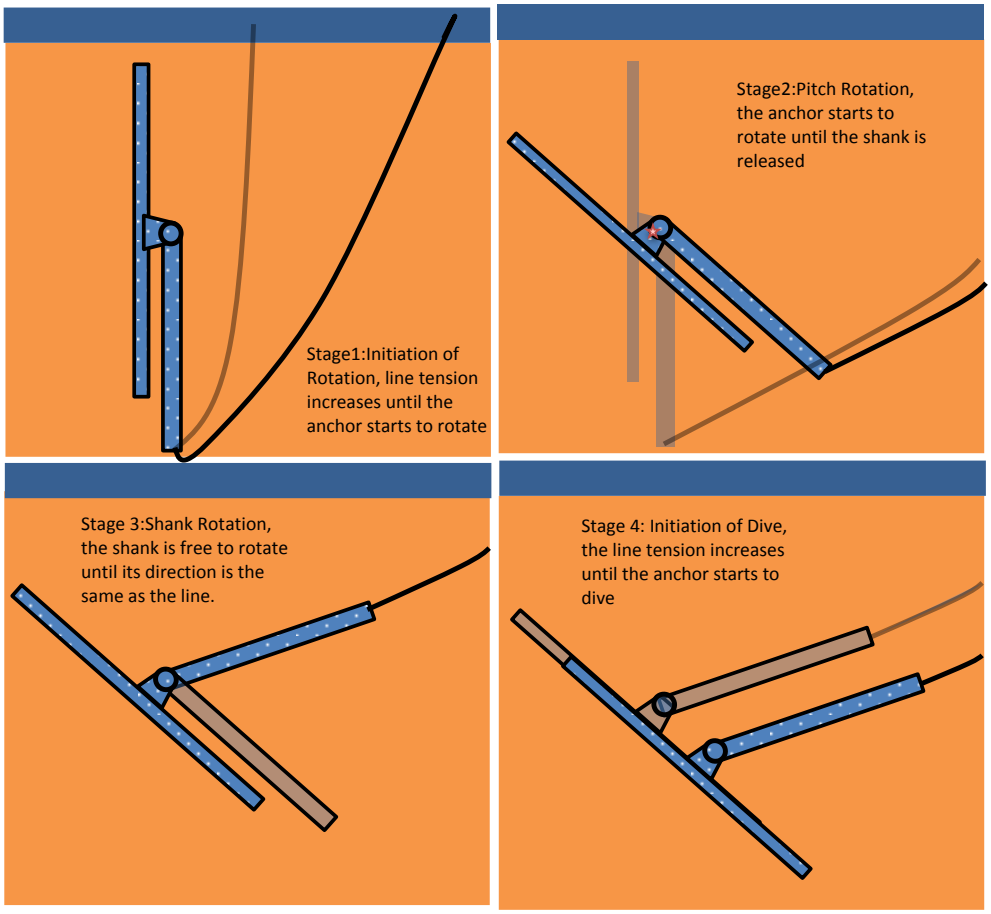

Figure 3.10 Dive initiation process

The Dive Initiation module has the following input parameters: (1) normal, shear and moment bearing capacity factors N_{nmax}, N_{tmax} and N_{mmax}, respectively; (2) area of the fluke A; (3) length from centroid to padeye in closed position e; (4) depth of the initial embedment z_a; (5) the angle between line and the fluke normal at shank release $\beta_{threshold}$; (6) the diameter of the line; and (7) the profile of undrained shear strength versus depth for the soil.

(1) Initiation of Rotation

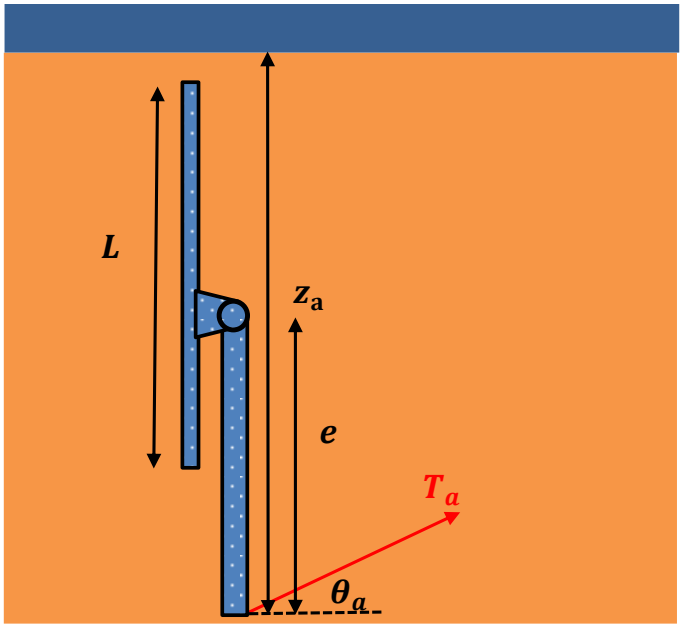

Figure 3.11 Free body diagram of the anchor at initiation of pitch rotation

Figure 3.11 shows the initial state of the anchor when it stops penetrating into the soil after free fall. The orientation of the anchor is vertical. The moment M driving the anchor to rotate is due to T_{ah}, which is the horizontal component force of the T_a. The anchor starts to rotate when M is larger than the ultimate moment capacity, which means that the soil fails when the ratio $\frac{M}{M_{\max}}$ is larger 1.0.

The objective of the Initiation of Rotation module is to find the combination T_a and θ_a that cause the anchor to rotate. We slowly increase T_a to find M until it is equal to the moment capacity. The algorithm of the Initiation of Rotation module is the following:

1) Start from $T_a^* = 0$.
2) Use $T_a = (su * A) * T_a^*$ to calculate the Ta.
3) Use function calthetaa(Nc, b, su_0, k, z_a, T_a, θ_0) to calculate θ_a corresponding to T_a and θ_0.

4) Use $T_{ah} = T_a * \cos\theta_a$ to calculate the horizontal tension T_{ah}.

5) Use $M = T_{ah} * e$ to calculate M and calculate $M_{max} = N_{mmax} * su * A * e$.

6) Compare the utilization ratio in moment $um = \frac{M}{M_{max}}$ with one. If $\frac{M}{M_{max}} > 1$, output the T_a and θ_a and stop calculation; if $\frac{M}{M_{max}} < 1$, $T_a^* = T_a^* + \Delta T_A^*$ and go to Step 2.

Function calthetaa(Nc, b, su_0, k, z_a, T_a, θ_0) is based on the Line Model Module to calculate θ_a; the VBA code of this function is shown in Appendix I.

(2) Pitch Rotation

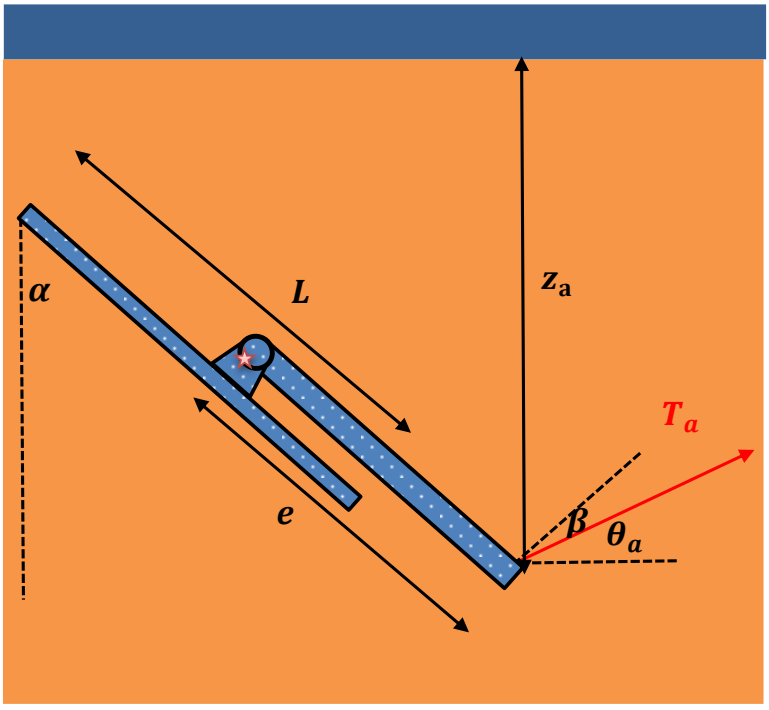

Figure 3.12 Free body diagram of the anchor at pitch rotation

Figure 3.12 shows the rotation of the anchor before the shank is released where β is the angle between the tension at padeye and the direction perpendicular to the fluke. We assume the tension T_a on padeye is constant during rotation. The ratio of the moment to ultimate moment capacity $\frac{M}{M_{\max}}$ is larger than 1 during rotation because the soil is in a failure state. The design of the hinge includes a trigger to release the shank (patent pending) when $> \beta_{threshold}$.

The objective of the Pitch Rotation module is to find α when β reaches $\beta_{threshold}$ by slowly increasing α to increase β. The algorithm for the Pitch Rotation module is the following:

1) Establish T_a and θ_a based on output from the Initiation of Rotation module.
2) Start from $\alpha = 0\ deg.$
3) Calculate β through $\beta = \alpha - \theta.$
4) Compare β with $\beta_{threshold}$. If $\beta > \beta_{threshold}$, output the α and exit the calculation; if $\beta < \beta_{threshold}$, $\alpha = \alpha + \Delta_\alpha$ and go to Step 3.

The goal in setting is $\beta_{threshold}$ is for α to be smaller than 90 degrees when the shank is released so that the anchor will dive into the soil rather out of the soil.

(3) Initiation of diving

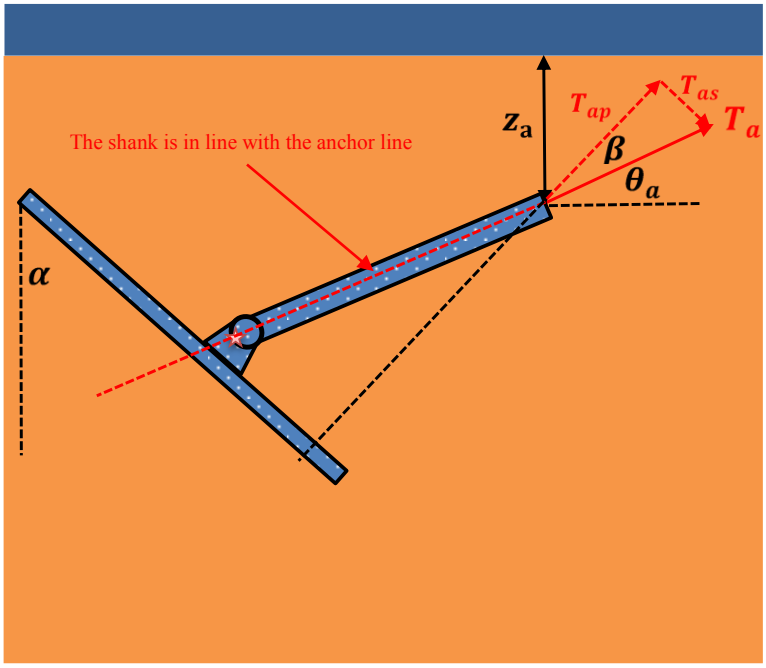

Figure 3.13 Free body diagram of anchor at initiation of dive

The shank will stop rotating when it is parallel to the anchor line since the shank is free to rotate about the fluke. The force applied to the fluke is divided into a bearing component $T_{ap} = T_a cos\beta$ and a shear component force $T_{as} = T_a sin\beta$. The anchor will yield and being to dive when the combination of T_{ap} and T_{as} reach the yield interaction surface (Figures 3.14 and 3.15).

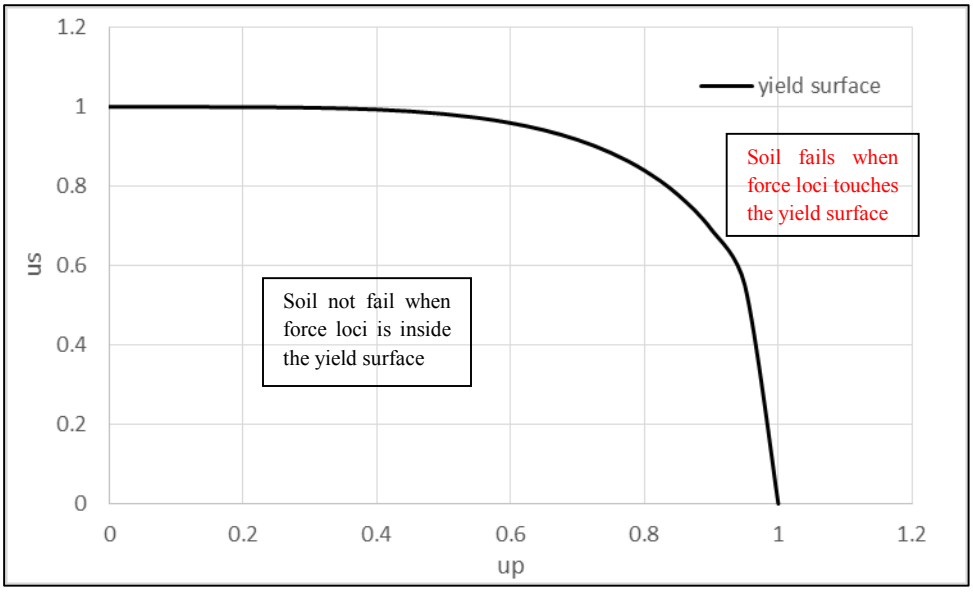

Figure 3.14 Yield surface drawn based on yield function (Equation 3.11)

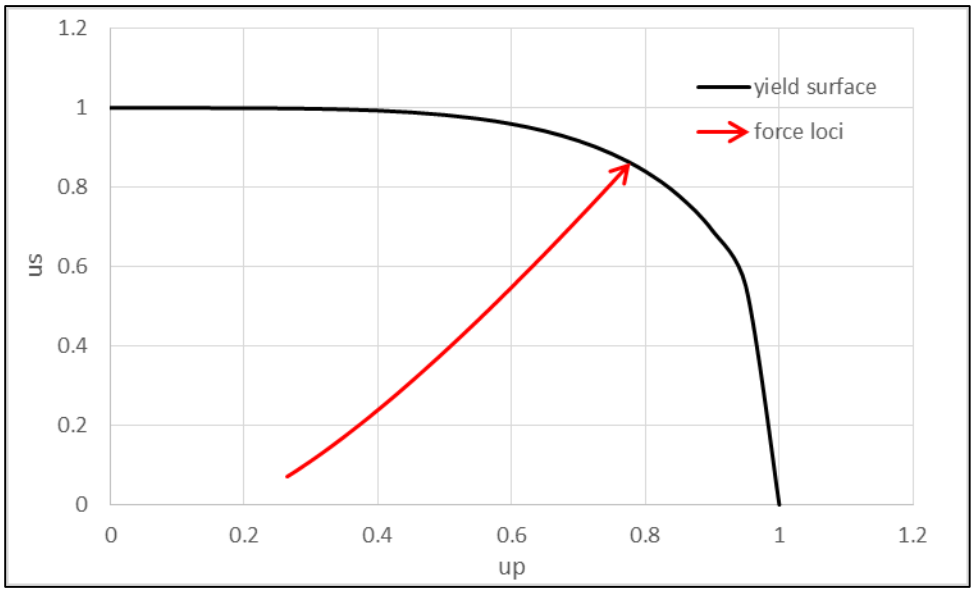

Figure 3.15 An example of force (loci) moving to the yield surface

The following equations describe the tension in the line when the yield surface is reached and the anchor will start to dive:

$$T_{as} = T_a sin\beta \qquad Equation\ (3.7)$$

$$us = \frac{T_{as}}{S_u A * N_{t,max}} = \frac{H}{H_{max}} \qquad Equation\ (3.8)$$

$$T_{ap} = T_a cos\beta \qquad Equation\ (3.9)$$

$$up = \frac{T_{ap}}{S_u A * N_{n,max}} = \frac{V}{V_{max}} \qquad Equation\ (3.10)$$

where us is the utilization ratio in shear loading, up is the utilization ratio in normal loading, V is normal load, H is shear load, and M is pitch moment. We then use the yield surface, Equation 2.9 with $\frac{M}{M_{max}} = 0$ since the shank and fluke are freely hinged, to calculate for a given value of up the value of shear utilization that touches the yield surface, us*:

$$us^* = [1 - (up)^q]^{\frac{p}{n}} \qquad Equation\ (3.11)$$

The objective of the Initiation of Dive module is to find the line tension, T_a and θ_a, that will cause the anchor to start diving. We slowly increase T_a until the forces on the anchor lie on the yield interaction surface. The algorithm of the Initiation of Dive module is the following:

1) Read the initial values of α, β, and T_a from the output of the Pitch Rotation module when the shank is released.
2) Calculate a normalized line tension $T_a^* = T_a/(A * su)$.
3) Use function calthetaa$(Nc,\ b,\ su_0,\ k,\ z_a,\ T_a,\ \theta_0)$ to calculate θ_a corresponding to T_a and update β.

4) Calculate the bearing component of line tension $T_{ap} = T_a cos\beta$ and the shear component of line tension $T_{as} = T_a sin\beta$.
5) Use Equations (3.8), (3.10) and (3.11) to calculate us, up, and us^*.
6) Compare us and us^*. If $us > us^*$, the anchor starts to dive and the calculation stops. If $us < us^*$, increase $T_a^* = T_a^* + \Delta_{T_a^*}$, calculated $T_a = T_a^* * A * su$, and go to Step 2.

3.3 TRAJECTORY PREDICTION MODULE

The objective of the Trajectory Prediction module is to calculate the trajectory of the anchor (horizontal and vertical displacement) versus the tension in the line at the mudline (Figure 3.16). The theoretical basis is to use the plasticity-based approach described in Chapter 2. For a given increment of movement parallel to the fluke, ds, the corresponding increment of movement perpendicular to the fluke, dn, is found from the normal to the yield surface:

$$\frac{dn}{ds} = \frac{\frac{\delta f}{\delta up}}{\frac{\delta f}{\delta us}} \qquad Equation\ (3.12)$$

where $f = f(up, us) = 0$ is the yield function

$$f(up, us) = us - [1 - (up)^q]^{\frac{p}{n}} = 0 \qquad Equation\ (3.13)$$

and up is the utilization ratio in normal loading and us is the utilization ratio in shear loading.

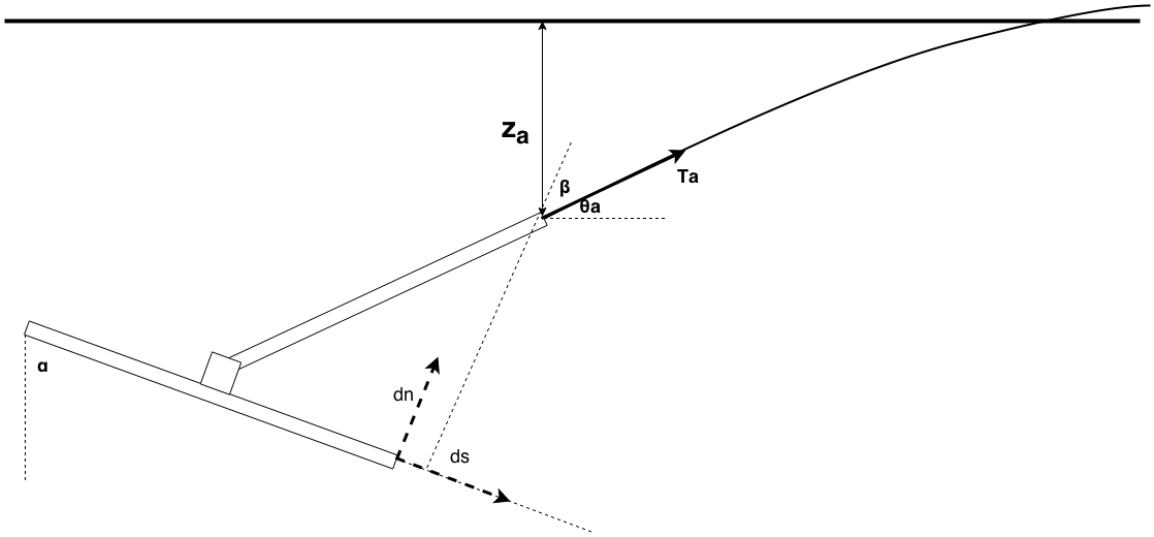

Figure 3.16 Plasticity solution for Flying Wing Anchor

Since there is no moment applied to the fluke, the fluke angle α is constant during diving. The anchor trajectory is solved for numerically by applying a small incremental displacement ds and then calculating dn from Equation (3.12). In this way, the center of the fluke is tracked as the tension in the line increases until the anchor pulls out from the ground in relatively pure bearing.

The Trajectory Prediction module implements the following algorithm to calculate the trajectory of the anchor as the tension in the anchor line increases at the mudline (Figure 3.17):

1) Input an incremental shear displacement Δs.
2) The initial depth $z = z_a$ and horizontal location x of the center of the fluke (i.e., the hinge point with the shank) is input.
3) For the anchor at (x, z), numerically iterate to find T_a such that $f(up, us) = 0$.
4) Calculate the ratio of normal to shear displacement $^{\mathrm{dn}}/_{\mathrm{ds}}$ for the anchor at (x, z) from Equation (3.12) based on finite-difference derivatives to find the normal to the yield function at (up, us):

$$\frac{\delta f(up,us)}{\delta up} = \frac{pq}{n}(1-up^q)^{\frac{p}{n}-1}up^{q-1} \qquad Equation\ (3.14)$$

$$\frac{\delta f(up,us)}{\delta us} = 1 \qquad Equation\ (3.15)$$

Where: $f(up,us)$ is Equation (3.13).

5) Calculate $\Delta n = \Delta s * {}^{dn}/_{ds}$.
6) Calculate a horizontal displacement increment: $\Delta x = \Delta s * sin\alpha + \Delta n * cos\alpha$; and calculate vertical displacement increment: $\Delta z = \Delta s * cos\alpha - \Delta n * sin\alpha$.
7) Update the anchor location (x_{new}, z_{new}) by calculating $x_{new} = x + \Delta x$ and $z_{new} = z + \Delta z$.
8) Go to Step 3 setting $x = x_{new}$ and $z = z_{new}$ until $\Delta z < \Delta z_{threshold}$.

The numerical iteration in Step 3 is accomplished with the Goal Seek function in Excel as follows:

1) Guess a value for T_a (use value from previous Step in Trajectory algorithm)
2) Calculate the corresponding θ_a with the line model function calthetaa.
3) Calculate the components of T_a: $T_{ap} = T_a * \sin(90 - \alpha + \theta_a)$ and $T_{as} = T_a * \cos(90 - \alpha + \theta_a)$.
4) Calculate normalized tension components: $T^*_{ap} = \frac{T_{ap}}{A*su}$ and $T^*_{as} = \frac{T_{as}}{A*su}$.
5) Calculate utilization ratios: $up = T^*_{ap}/N_{nmanx}$ and $us = T^*_{as}/N_{tmanx}$.
6) Calculate the yield function $target = |f(up,us) - 1|$. If $target < 10^{-3}$, output T_a and stop calculation. If $target > 10^{-3}$, guess another T_a and go to Step 2.

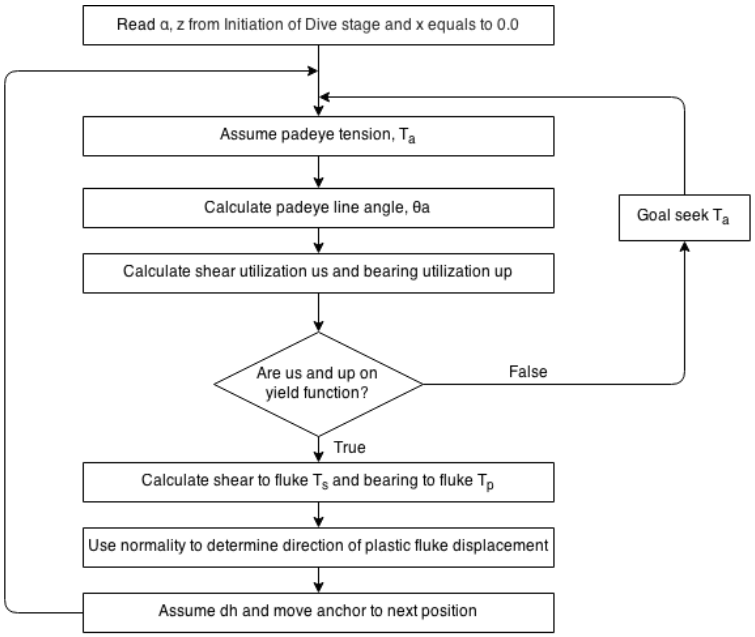

Figure 3.17 Analysis flowchart for trajectory prediction

3.4 SENSITIVITY ANALYSIS ON A FULL-SCALE ANCHOR EXAMPLE

In this section, a prototype anchor is analyzed using the predictive model. We assume the fluke length L is 4 meters and ratio of the shank length e to fluke length L equals one. The parameters of the prototype anchor are shown in Table 3.1. It is analyzed both with a catenary mooring system (θ_0 is equal to 5 degrees) and a taut mooring system (θ_0 is equal to 35 degrees). The following factors are considered in the sensitivity analysis: (1) the shank release angle, $\beta_{threshold}$; (2) the profile of undrained shear strength versus depth, s_{u0} and k; (3) the diameter of the anchor line or chain, b; (4) and the depth of initial embedment, z_a (Figure 3.18).

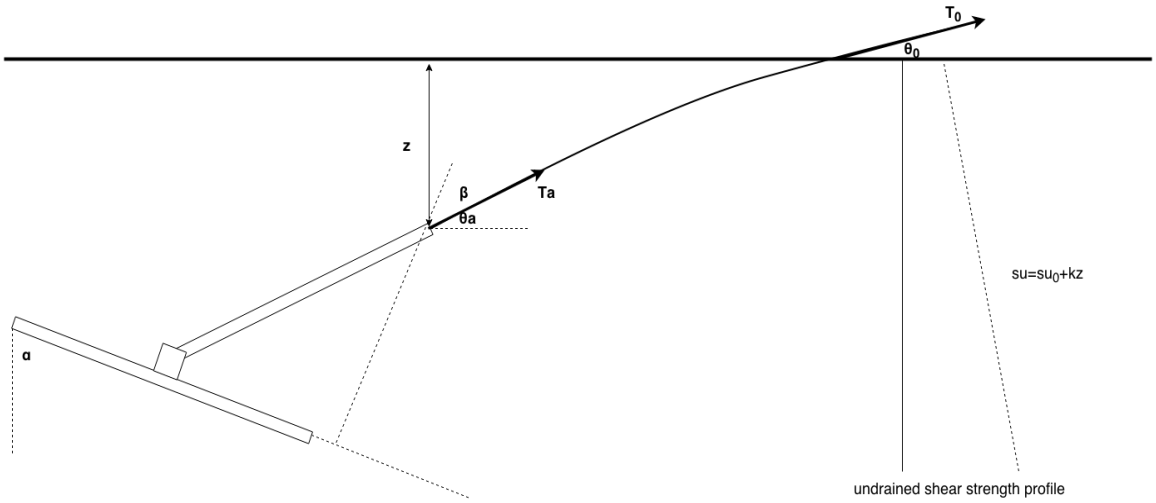

Figure 3.18 Parameters definition for trajectory program

Before conducting the sensitivity analysis, we establish an appropriate incremental shear displacement Δs to use for calculating the dive trajectory (Figure 3.19). For this problem, a value of $\Delta s \leq 8\,m$ or $\Delta s \leq 2L$ provides stable results.

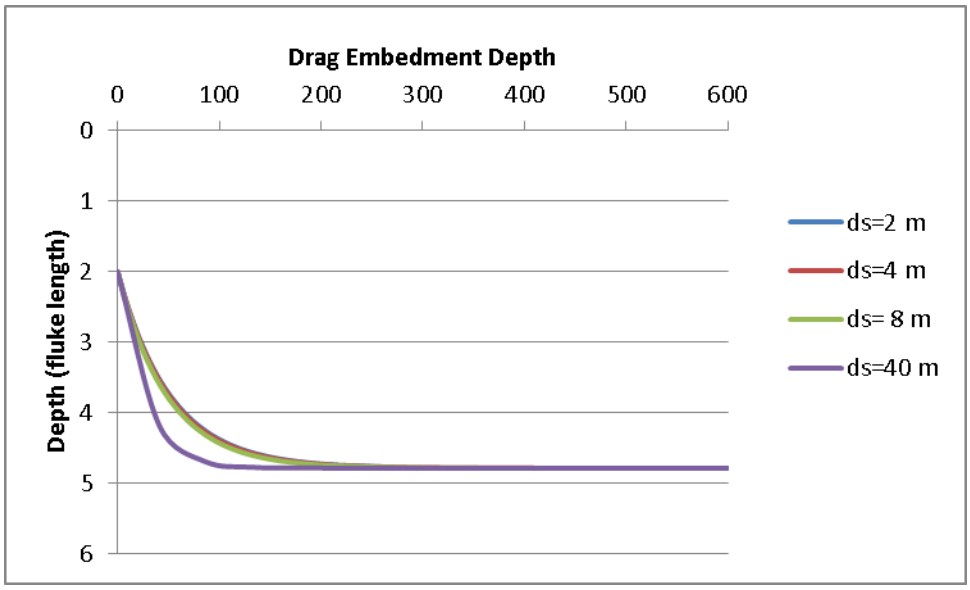

Figure 3.19 Sensitivity of trajectory to Δs in catenary mooring system

Input Share		
Soil Parameters		
su_0 (Kpa)	10	undrained shear strength at mudline
k (Kpa/m)	1.5	gradient of profile
Line Parameters		
Type	1	1: wire 2: chain
En	1	chain multiplier, 1 for wire, 2.5 for chain
d(mm)	400	diameter of line
b(mm)	400	effective diameter of line = E_nd
d(m)	0.4	diameter of line
b(m)	0.4	effective diameter of line
Nc_mudline	5.1	bearing capacity factor at mudline
Nc_break in	7.6	bearing capacity factor below depth of 2.4b
μ	0.4	friction coefficient
θ_0 (degree)	5	angle at mudline
Anchor Parameters		
z_a (m)	8	initial embedment depth
A (m^2)	16	the area of fluke
e/A^0.5	1	Length from centroid to padeye in closed position
q	4.43	yield surface interaction factor
n	4.19	yield surface interaction factor
p	1.57	yield surface interaction factor
Ns	4	moment bearing capacity factor
Np	12.5	shear bearing capacity factor
Nm	2.5	normal bearing capacity factor

Table 3.1 Input parameters for prediction example

3.4.1 Different release angles, $\boldsymbol{\beta_{threshold}}$

Figure 3.20 shows the proportional relationship between the $\beta_{threshold}$ and the inclination of the fluke when the shank is released, α, from the output of the Dive Initiation module. This relationship is helpful in understanding how $\beta_{threshold}$ affects the trajectory.

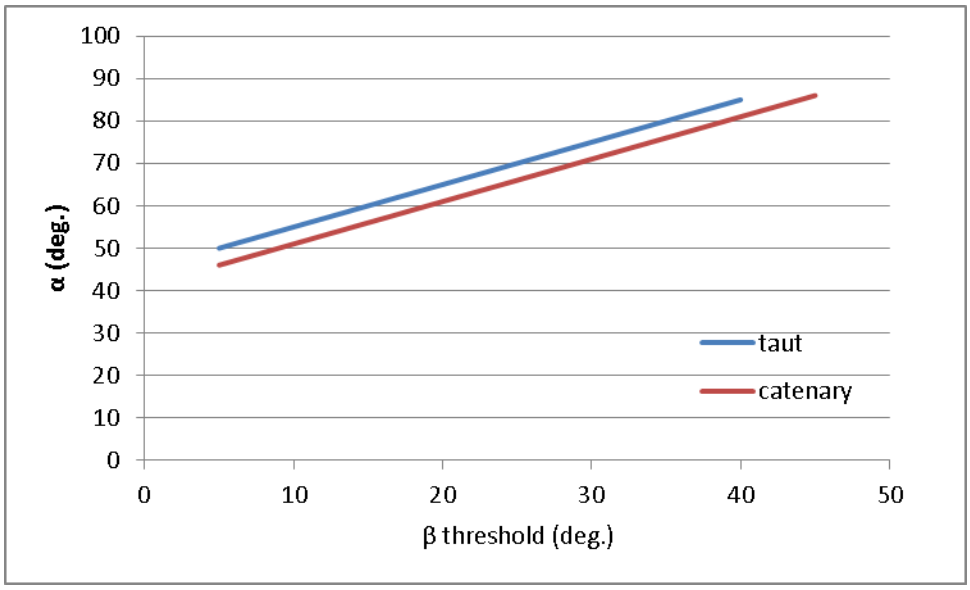

Figure 3.20 Relationship between $\beta_{threshold}$ and α

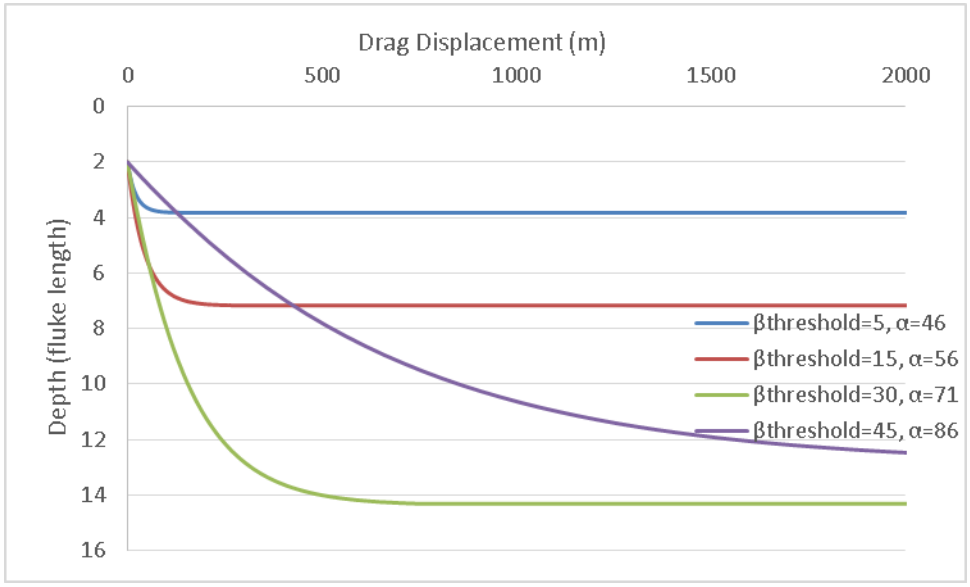

Figure 3.21 Trajectories with different $\beta_{threshold}$ for the catenary mooring system

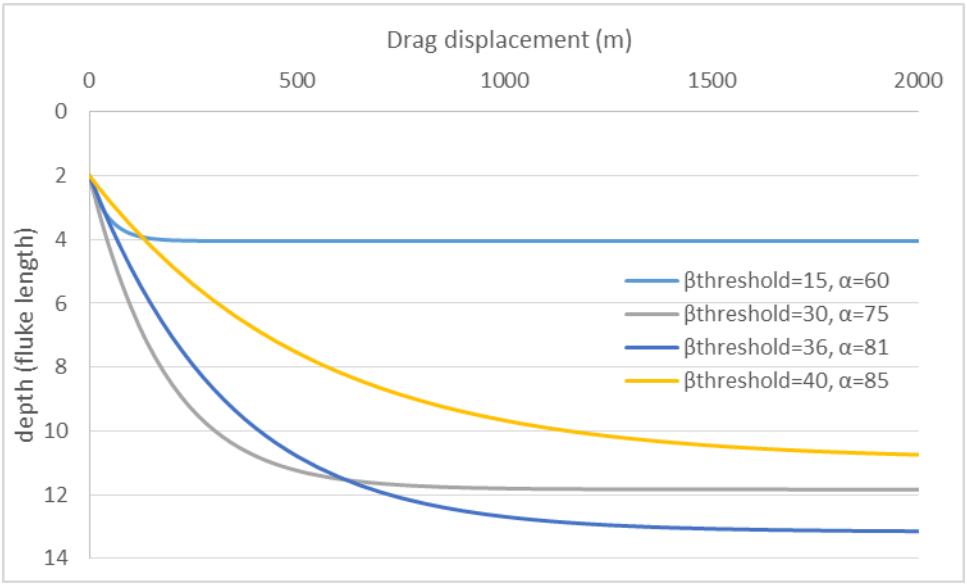

Figure 3.22 Trajectories with different $\beta_{threshold}$ for the taut mooring system.

For the catenary mooring system, the ultimate depth of the trajectory increases with increasing $\beta_{threshold}$ for $\beta_{threshold}$ values from 5 to 30 degrees; however, the ultimate depth with $\beta_{threshold} = 45°$ is smaller than that of the $\beta_{threshold} = 30°$ (Figure 3.21). The taut system shows similar results (Figure 3.22). These results highlight the balance between releasing the shank too early, in which case the line force on the fluke is oriented more in the normal than the shear direction causing the anchor to pull up in bearing, and releasing the shank too late, in which case the anchor tends to slide horizontally rather than dive. Based on these results for this prototype anchor, a value of $\beta_{threshold}$ of between 30° and 40° produces optimal behavior.

To explain the theoretical basis for the results in Figures 3.21 and 3.22, it is helpful to revisit the plasticity solution (Equations 3.12 and 3.13). By separating dv and dh into vertical and horizontal directions (Figure 3.23), we could obtain the following equations:

$$dx = dh * \sin(\alpha) + dh * \frac{\frac{\delta f}{\delta up}}{\frac{\delta f}{\delta us}} * \cos(\alpha) \qquad Equation\ (3.16)$$

$$dz = dh * \cos(\alpha) - dh * \frac{\frac{\delta f}{\delta up}}{\frac{\delta f}{\delta us}} * \sin(\alpha) \qquad Equation\ (3.17)$$

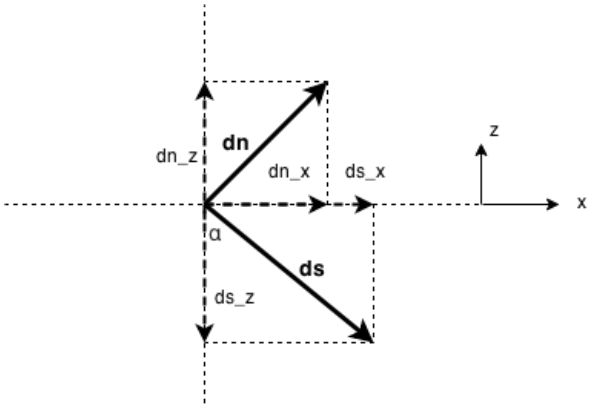

Figure 3.23 Component forces in vertical and horizontal directions

The differential movement in the vertical direction, dz in Equation (3.17), controls how the trajectory evolves to the ultimate depth where dz approaches zero. The yield surface gradient component of dz, $\frac{\frac{\delta f}{\delta up}}{\frac{\delta f}{\delta us}}$, increases with increasing depth z for different values of α (Figure 3.24) and therefore $\beta_{threshold}$ (Figure 3.20).

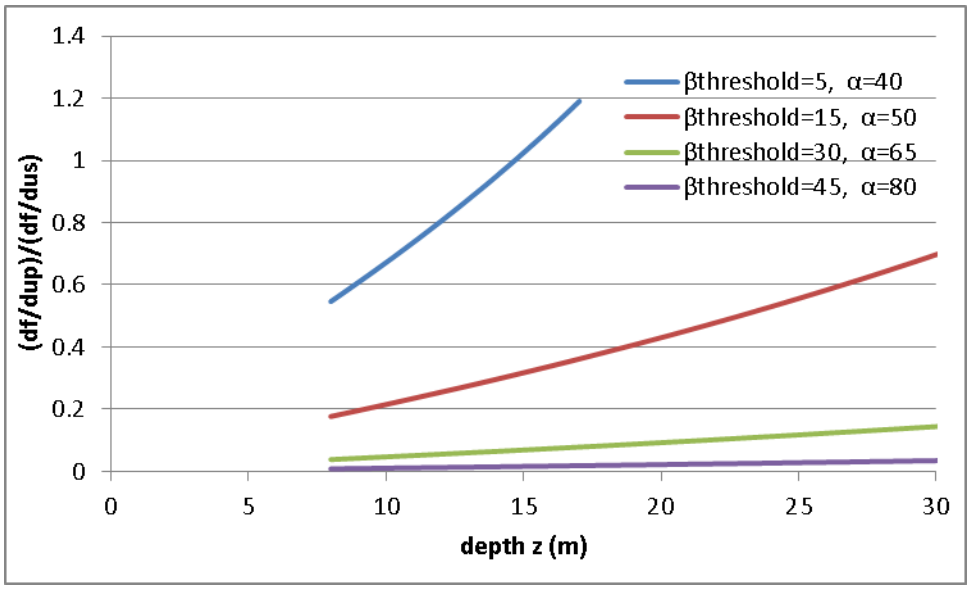

Figure 3.24 Relationship between yield surface gradient and depth in different α ($\theta_0 = 5°$)

For convenience of notation, define the yield surface gradient , $\frac{\frac{\delta f}{\delta up}}{\frac{\delta f}{\delta us}}$, as a function of z and α, F(z, α). This gradient increases with depth, meaning that the yield point on the yield interaction surface is moving in a counterclockwise direction with increasing depth (Figure 3.25). For a given depth, this gradient decreases with increasing fluke pitch (α), meaning that the starting yield point on the yield surface moves in a clockwise direction as α increases further away from a bearing failure (Figure 3.25). Also, the change in the yield surface gradient with increasing depth decreases as α increases (Figure 3.24).

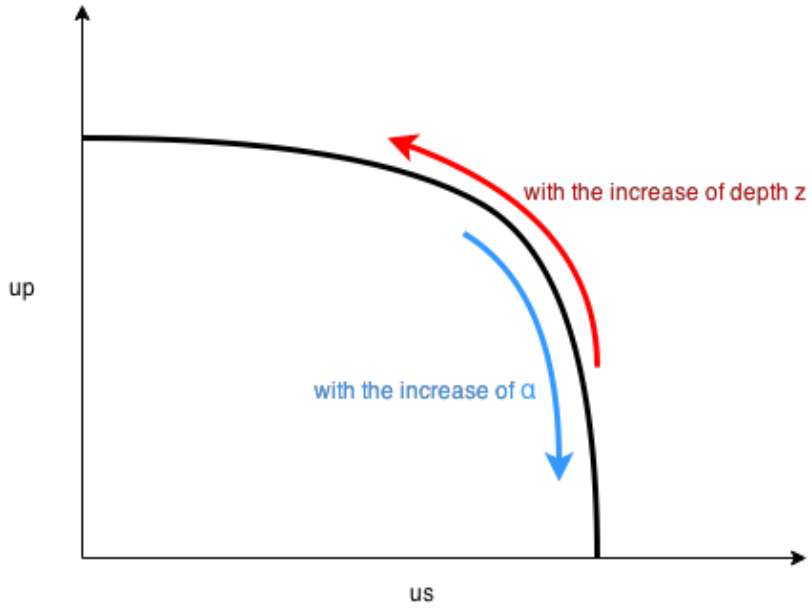

Figure 3.25 Yield surface

If we substitute F(z, α) into Equation (3.17):

$$dz = dh * \cos(\alpha) - dh * F(z, \alpha) * \sin(\alpha) \qquad Equation\ (3.18)$$

This equation shows that when $F(z, \alpha)$ is small, the $\cos(\alpha)$ and $\sin(\alpha)$ terms will control dz. Furthermore, as α increases, dz and the strength of diving decrease. Conversely, when $F(z, \alpha)$ is large (i.e., small α or large z), it will control dz and the anchor will tend to fail in the bearing direction and not dive.

From Figure 3.24, we see that when the pitch of the fluke is shallow when the shank is released ($\alpha = 71°$ and $\alpha = 86°$), the F(a, α) values are relatively small and the smaller α (greater pitch at shank release) will result in a deeper dive (Figures 3.21 and 3.22). Conversely, when pitch of the fluke is steep when the shank is released, the F(a, α) values are relatively large and a larger α will result in a deeper dive (Figures 3.21 and 3.22). The resulting relationship between the depth of the dive and the threshold release angle is shown in Figure 3.26.

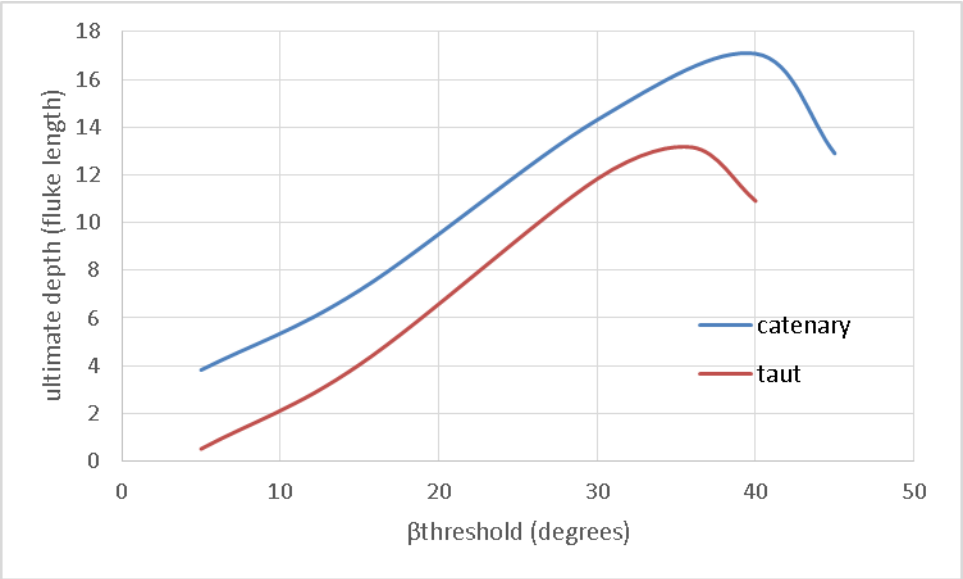

Figure 3.26 The relationship between $\beta_{threshold}$ and ultimate depth

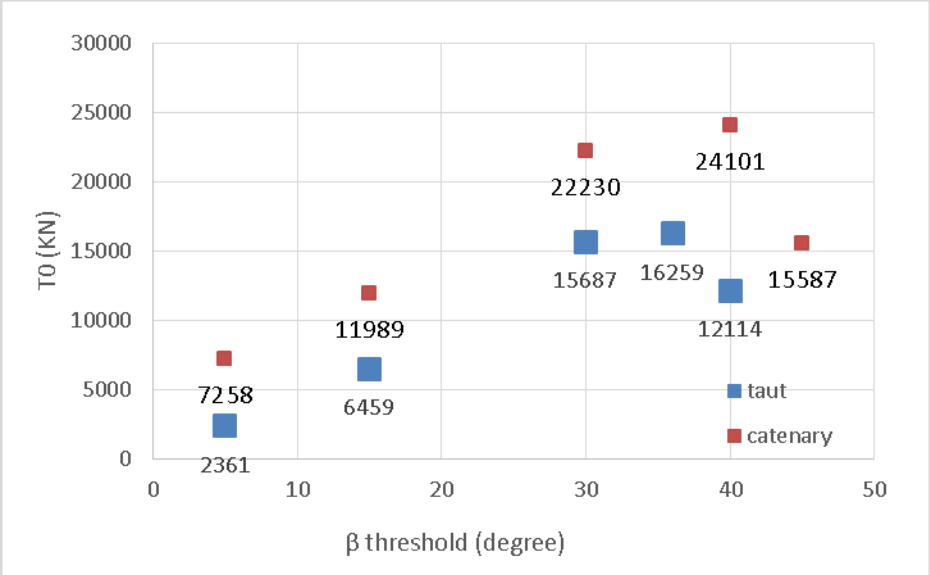

Figure 3.27 The relationship between $\beta_{threshold}$ and ultimate capacity

The ultimate capacity T_0 changes with the release angle $\beta_{threshold}$ (Figure 3.27) in a way similar to the how the ultimate depth changes with release angle (Figures 3.21 and 3.22).

3.4.2 Different profiles of undrained shear strength

The following profiles of undrained shear strength versus depth were considered: su_0 of 10 Kpa and k of 0, 0.5, 1.0, 1.5, 2, 2.5 kPa/m. These profiles are representative of underconsolidated to overconsolidated clays.

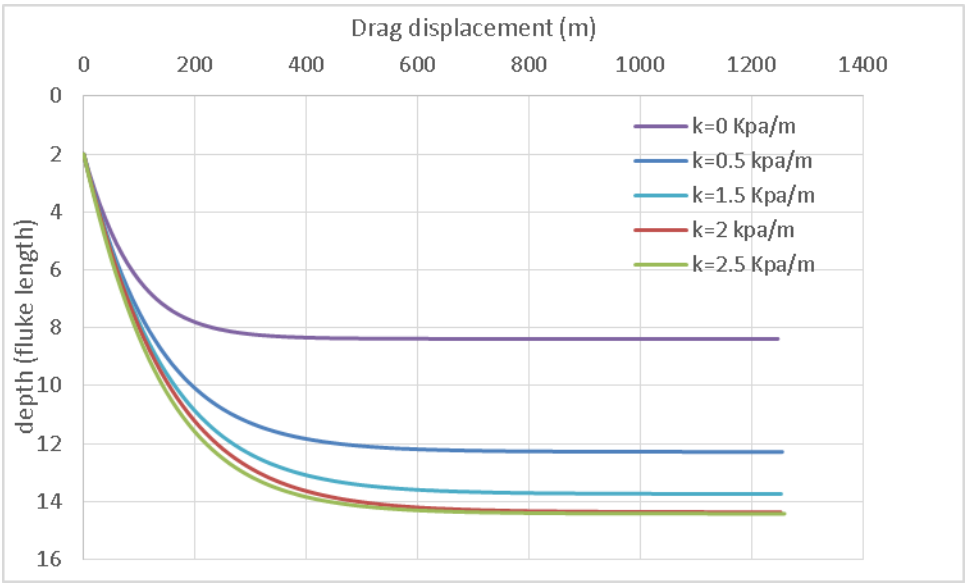

Figure 3.28 Trajectories of different su profiles for catenary mooring system

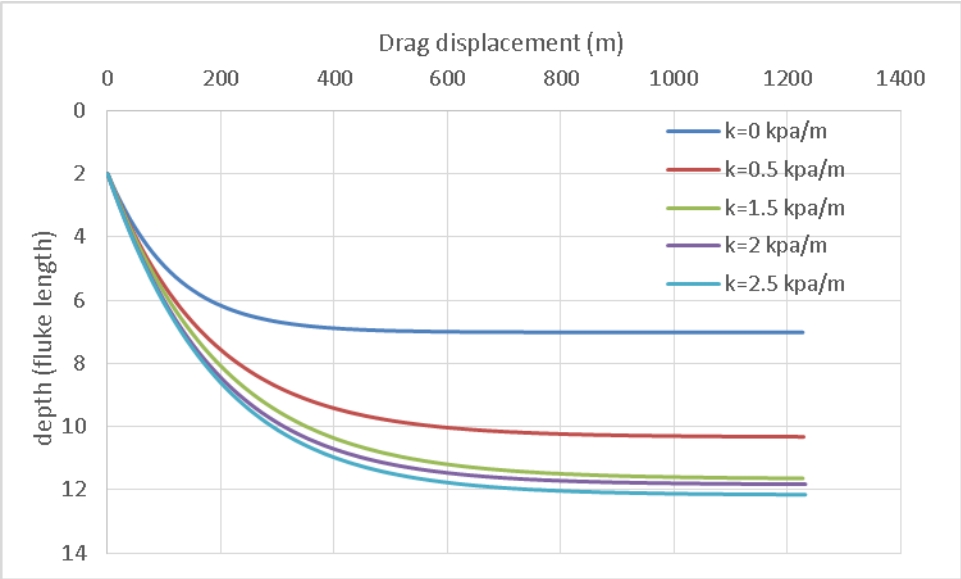

Figure 3.29 Trajectories of different su profiles for taut mooring system

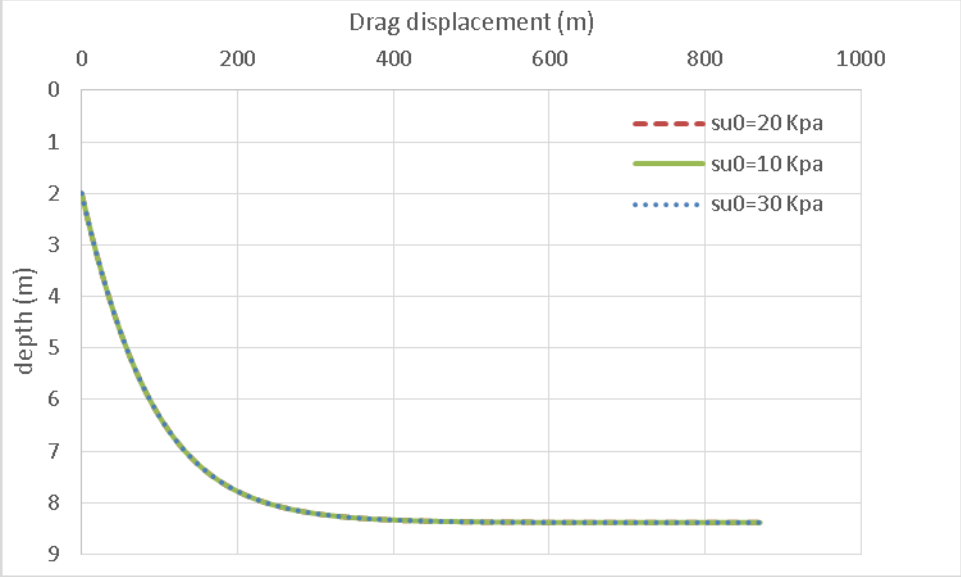

Figure 3.30 Trajectories of different su0 (k=0) for catenary mooring system

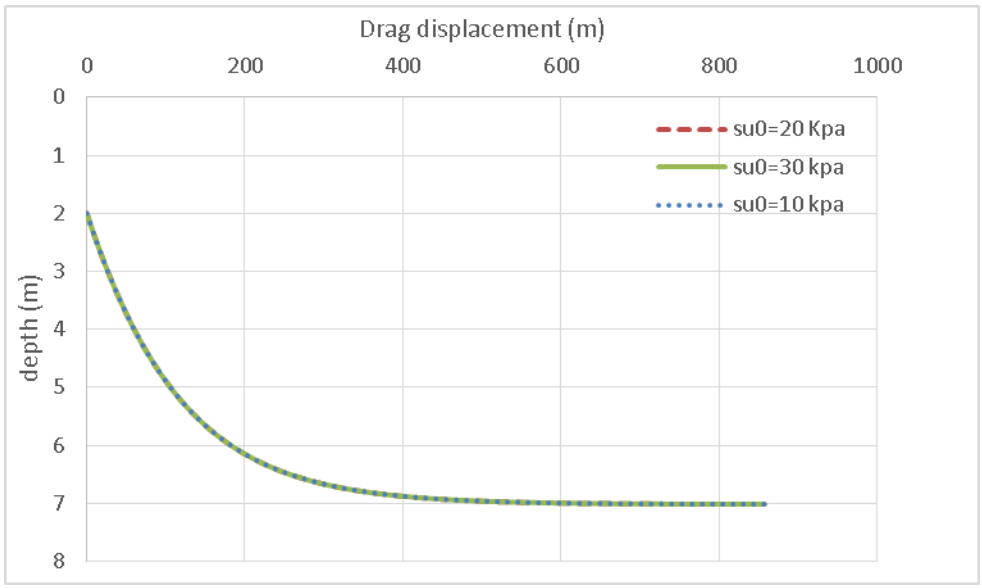

Figure 3.31 Trajectories of different su0 (k=0) for taut mooring system

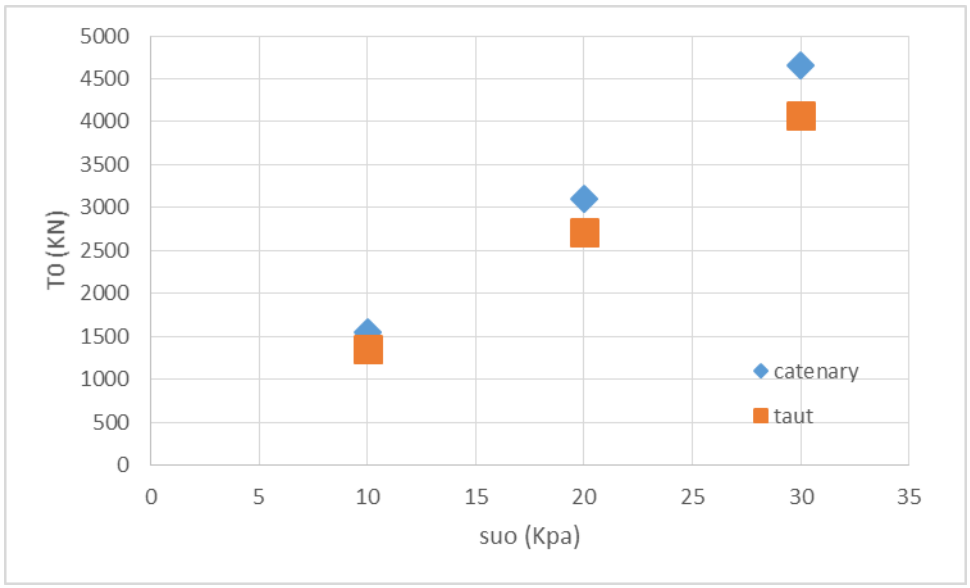

Figure 3.32 The relationship between su_0 and ultimate capacity

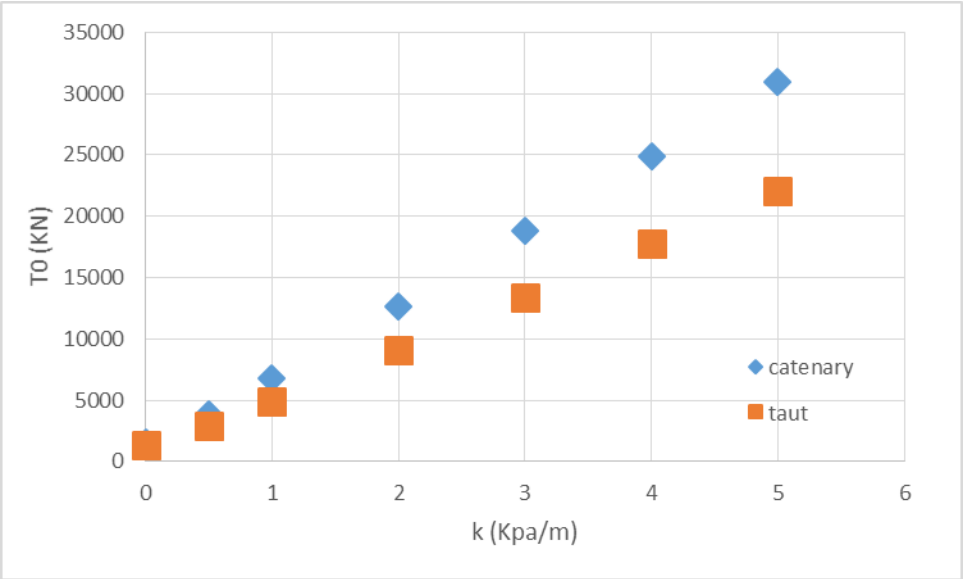

Figure 3.33 The relationship between k and ultimate capacity

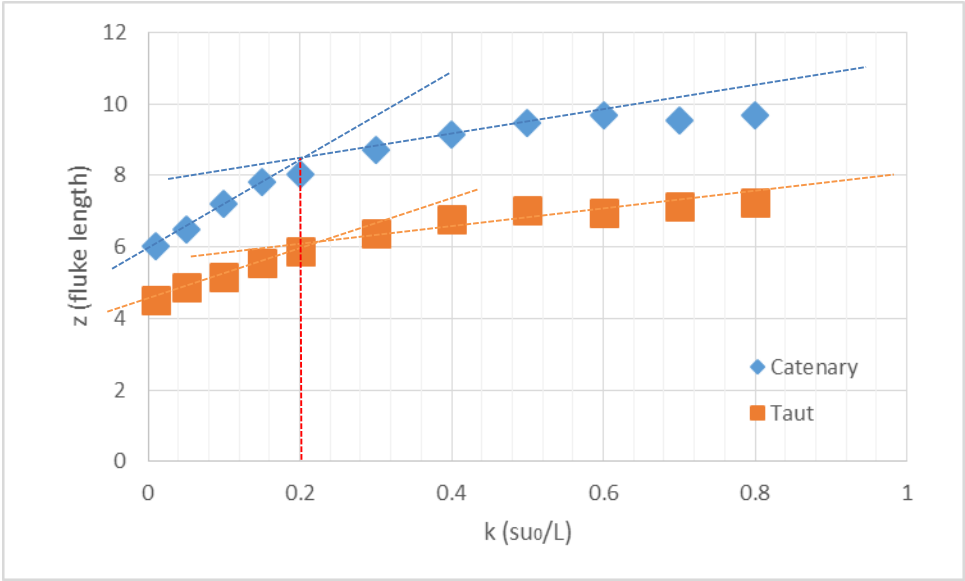

Figure 3.34 The relationship between $k$and ultimate depth

For small values of the strength gradient [$k \leq 0.5\ kPa/m\ or\ (1/5)(su_0/L)$], the dive depth is independent of the strength gradient and independent of the strength intercept

(Figures 3.30 and 3.31). In this case, the ultimate capacity is proportional to the strength intercept (Figure 3.32). As the strength gradient becomes large enough relative to the intercept [$k \geq 1.5\ kPa/m\ or\ (3/5)(s_{u0}/L)$, which is typical for a normally consolidated clay], the dive depth is a constant that is deeper than for a constant strength with depth (Figures 3.28 and 3.29) and the holding capacity is proportional to the strength gradient (Figure 3.33).

3.4.3 Different diameters of the chain

We analyzed the sensitivity of the anchor performance to a line (200-mm diameter line) versus a chain (400-mm diameter line). The ultimate dive depth and ultimate capacity increase as the diameter of the line decreases; however, the relative increase in capacity is not as great that for depth because the frictional capacity along the length of the anchor increases with an increasing diameter.

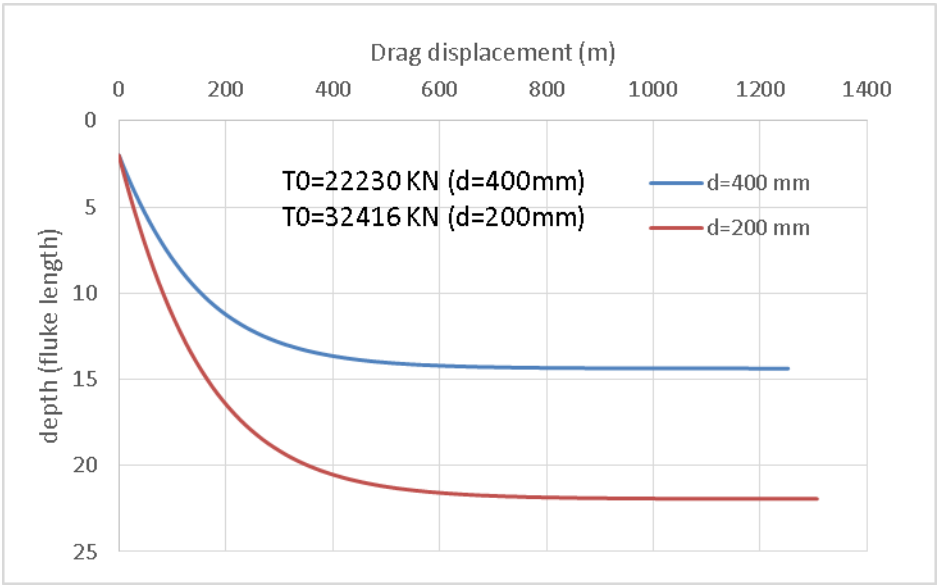

Figure 3.35 Trajectories of different diameters of the chain for the catenary mooring system

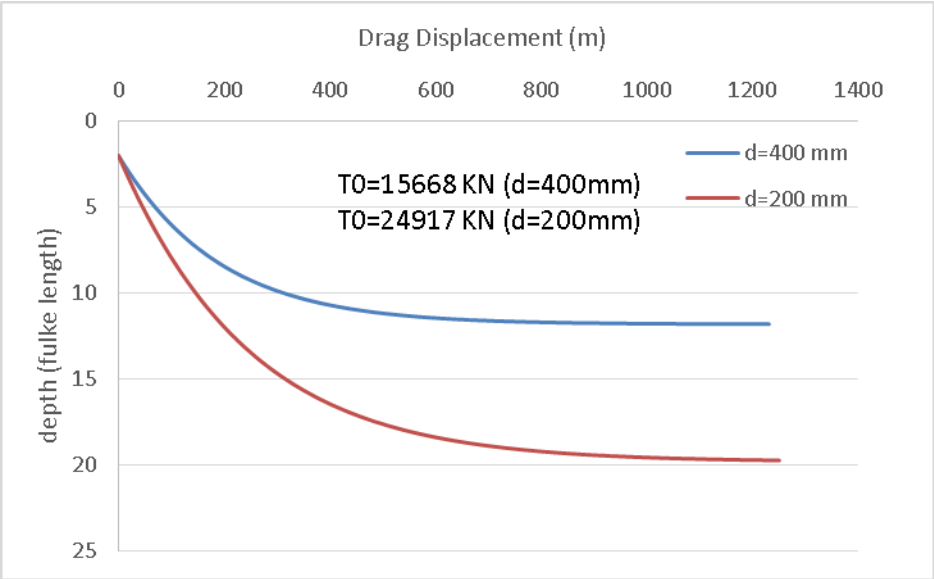

Figure 3.36 Trajectories of different diameters of the chain for the taut mooring system

3.4.4 Different initial embedment depth

In this study, we analyzed the influence of different initial embedment depths after free fall: 4 m, 8 m, 12 m, 16 m. The deeper the initial embedment, the deeper the dive trajectory (Figures 3.37 and 3.38) and the greater the holding capacity (Figure 3.39).

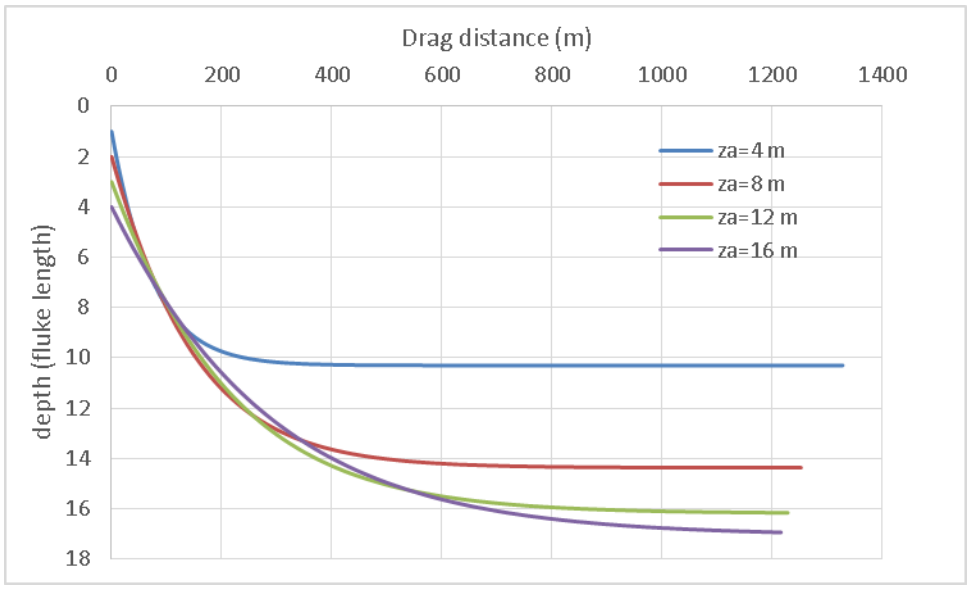

Figure 3.37 Trajectories of different initial embedment depths for the catenary mooring system

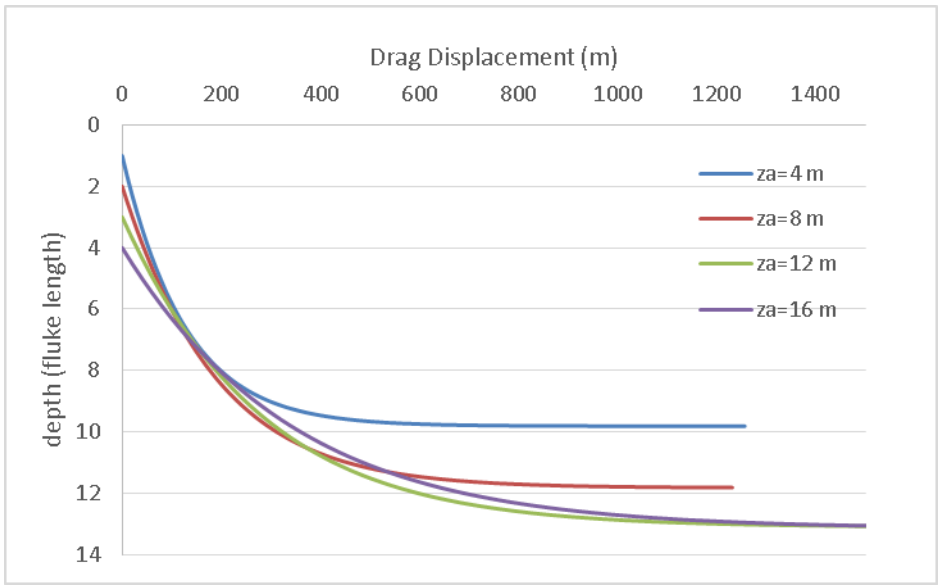

Figure 3.38 Trajectories of different initial embedment depths for taut mooring system

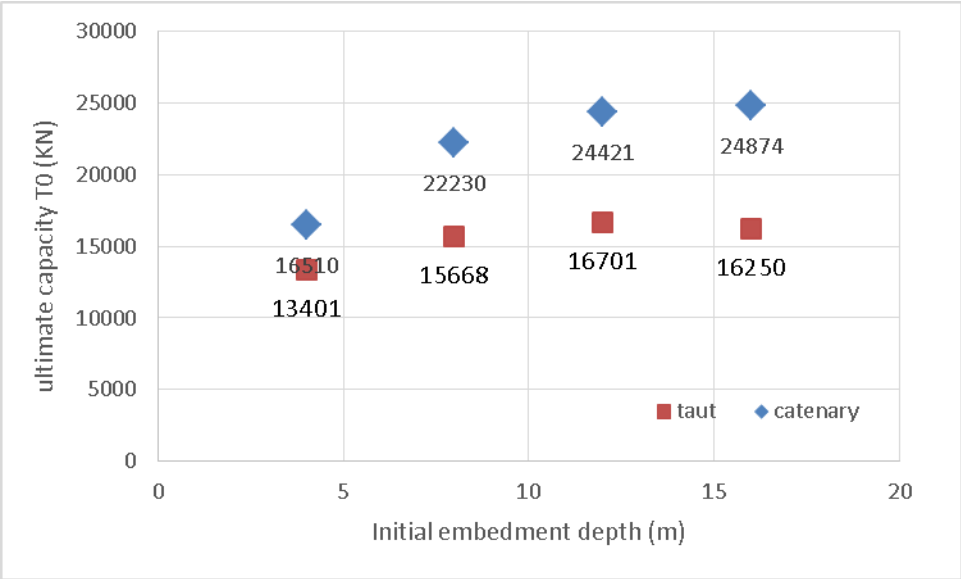

Figure 3.39 The relationship between initial embedment depth and ultimate capacity

3.5 SUMMARY OF SIMPLIFIED PREDICTIVE MODEL

The simplified predictive model predicts the trajectory of the anchor based on the geometry of the anchor and the anchor line and the shear strength of the soil. The trajectory model consists of four modules: (1) input module, (2) line model module, (3) dive initiation module and (4) dive trajectory module. The parameters input in the input module are shared in all the other modules. The line model module describes the shape of the line, the angle θ_a at the padeye, and the tension T_0 at the mudline. The dive initiation module figures out the orientation of the anchor before diving. With the result from the dive initiation module, the trajectory module calculates the trajectory of the anchor and holding capacity (line tension at mudline) during diving.

The release angle $\beta_{threshold}$, the profile of the soil, the diameter of the line, and the initial embedment depth all influence the trajectory and holding capacity.

(1) The ultimate dive depth and holding capacity are maximized when the shank is released from the fluke at a line angle with respect to the fluke normal ($\beta_{threshold}$) of about 30 degrees.
(2) For a constant undrained shear strength with depth, the dive depth is a constant independent of the strength and the holding capacity is proportional to the strength. At the other extreme for a linearly increasing strength with depth with a small intercept, the dive depth is a constant that is deeper than for a constant strength and the holding capacity is proportional to the strength gradient.
(3) The anchor dives deeper and the ultimate capacity increases as the diameter fo the anchor line decreases.
(4) The deeper the initial embedment depth after free fall, the deeper the dive trajectory and the greater the holding capacity.

Chapter 4: Design Plan for Experimental Tests

In this chapter, we design experimental tests to study the behavior of the Flying Wing Anchor during drag. The first phase of the plan consists of tests to measure the pure normal bearing factor, the pure shear bearing factor, and the pure moment bearing factor. The second phase of the plan consists of tests to calibrate the simplified model to predict the trajectory of the anchor after it has been embedded by free fall (Chapter 3).

4.1 BEARING FACTORS

The pure normal bearing factor $N_{nmax} = \frac{N_{max}}{s_u A}$, pure shear bearing factor $N_{tmax} = \frac{T_{max}}{s_u A}$, and pure moment bearing factor $N_{mmax} = \frac{M_{max}}{s_u A\sqrt{A}}$ depend on the characteristic of the anchor. The objective of the first phase of model testing is to measure the bearing capacities for the model-scale anchor.

4.1.1 Pure normal bearing factor for the anchor

Figure 4.1 shows the experimental test configuration for measuring the pure normal bearing capacity of the anchor. The rod is connected to the gravity center of the anchor and is perpendicular to the plate of the anchor, which prevents the rotation of the anchor during pulling out. The load cell is connected to the upper side of the rod to measure the resistance force when the electric motor moves in a constant speed. The speed of being pulled out is controlled by the electric motor. The initial embedment depth of the anchor is set to be at least 2.5L (fluke length) below the mudline where the anchor is deep enough to make the soil be fully constrained.

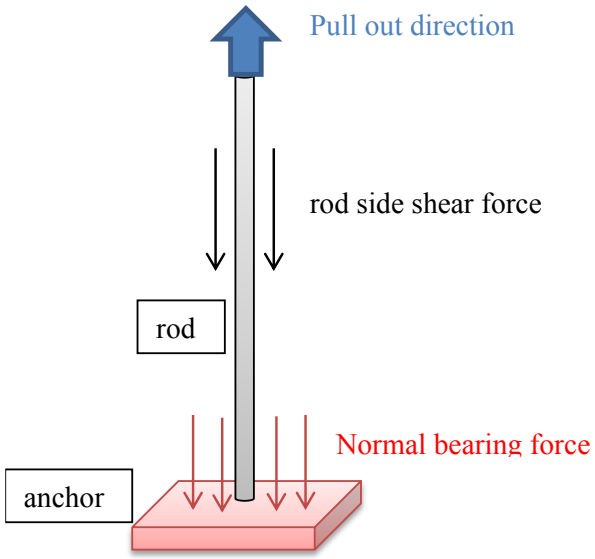

Figure 4.1 Test configuration for measuring the pure normal bearing factor

We have following equation to calculate the pure normal bearing factor:

$$N_{nmax} = \frac{F_{rod+anchor} - F_{rod} - W'_{anchor}}{S_u * A_f} \qquad Equation\ (4.1)$$

Where: $F_{rod+anchor}$ = resistance normal force of the anchor with the rod

F_{rod} = resistance shear force of the separate test on the rod

W'_{anchor} = submerged weight of the anchor

S_u = undrained shear strength

A_f = area of fluke

To measure the F_{rod}, we need to a separate test on the steel rod to measure the side shear force on the rod. The procedure of measuring the pure normal bearing capacity factor is the following:

(1) Push the anchor model into the target depth

(2) Set a constant speed on motion control system to pull out the rod

(3) Use Data Acquisition system to read the normal bearing force with the rod from the load cell

(4) Take off the anchor from the rod

(5) Measure the side shear force on the rod from the same depth

(6) Calculate the pure normal bearing factor N_{nmax}

4.1.2 Pure shear bearing factor for the anchor

Figure 4.2 shows the experimental test configuration for measuring the pure shear bearing factor of the anchor. In this test, the rod is attached parallel to the face of the fluke. The attached point is the gravity center of the anchor. The load cell is rigged with the rod directly and wired with the electric motor through pulleys. The electric motor moves as a constant rate to pullout the rod. This system makes the shear direction stay the same during the test.

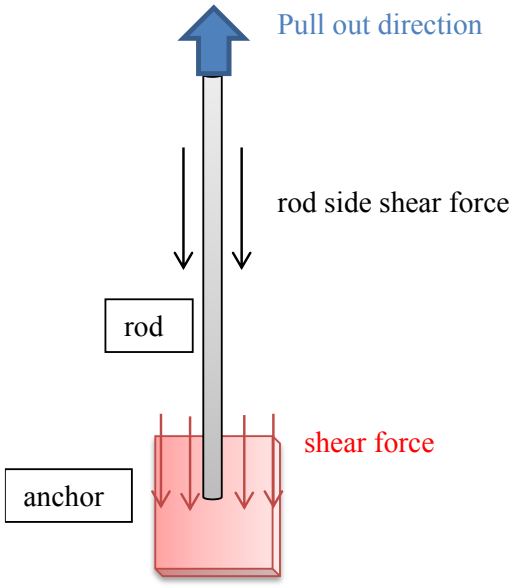

Figure 4.2 Test configuration for measuring the pure shear bearing factor

We have the following equation to calculate the pure shear bearing factor:

$$N_{tmax} = \frac{F_{rod+anchor} - F_{rod} - W'_{anchor}}{S_u * A_f} \qquad Equation\ (4.2)$$

Where: $F_{rod+anchor}$ = resistance shear force of the anchor with the rod

F_{rod} = resistance shear force of the separate test on the rod

W'_{anchor} = submerged weight of the anchor

S_u = undrained shear strength

A_f = area of fluke

The procedure for measuring the pure shear bearing factor is kept the same as pure normal bearing factor test.

4.1.3 Pure moment bearing factor for the anchor

Figure 4.3 shows the experimental test configuration for measuring the pure moment bearing factor of the anchor. The anchor and a pulley are connected by the rod. One side of the rod the attached parallel on the face of the anchor and the other side of the rod is rigged with the center of the pulley. The electric motor pulls the line to generate a drive force on the pulley. A pitch moment is produced by the drive force and equals to the force multiplying the radius of the pulley. The pitch moment capacity is equal to the resistance moment acting on the anchor.

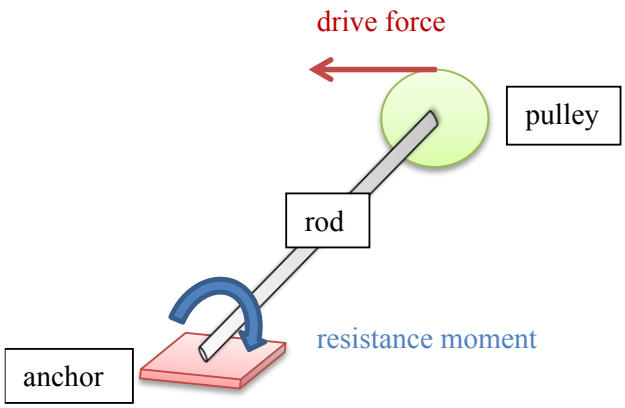

Figure 4.3 Test configuration for measuring the pure moment bearing factor

The following equation is used to calculate the pure moment bearing factor:

$$N_{mmax} = \frac{M_{anchor+rod} - M_{rod}}{S_u * A_f * L_f} \qquad Equation\ (4.3)$$

Where: $M_{rod+anchor}$ = resistance moment force of the anchor with the rod

M_{rod} = resistance moment force of the separate test on the rod

S_u = undrained shear strength

A_f = area of fluke

L_f = length of the fluke

Moment is calculated by the following equation:

$$M = F_{drive} * r \qquad Equation\ (4.4)$$

Where: F_{drive} = the force to rotate the anchor

r = radius of the pulley

The procedure for measuring the pure moment bearing factor is kept the similar as pure normal bearing factor test except the rod is rotated by the pulley but not be pulled out.

4.1.4 Previous tests

Ganjoo (2010) conducted similar tests on measuring N_{nmax}, N_{tmax}, and N_{mmax}. Ganjoo (2010) used two anchor models: an original anchor model and a wider anchor model (Figure 4.4). The soil test bed was Kaolinite.

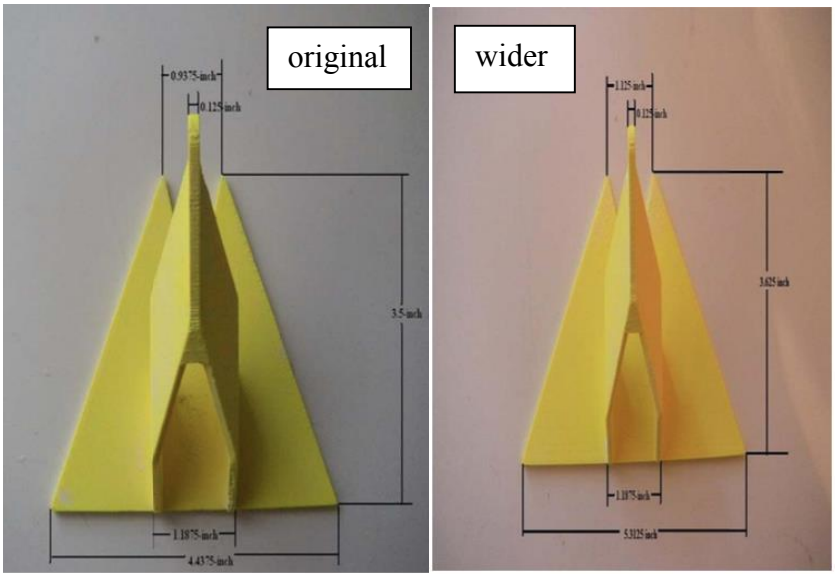

Figure 4.4 Two anchor models used by Ganjoo (2011)

The results of pure normal bearing factors tests are summarized in Tables 4.1 to 4.6. The average N_{nmanx} for the original anchor model is 11.5 (Table 4.1), and the average N_{nmanx} for the wider anchor model is 10.9 (Table 4.2). The average N_{tmanx} for the original anchor model is 5.4 (Table 4.3), and the average N_{tmanx} for the wider anchor model is 5.3 (Table 4.4). The average N_{mmanx} for the original anchor model is 2.4 (Table 4.5), and the average N_{mmanx} for the wider anchor model is 2.4 (Table 4.6).

Test ID	Approximated Su (psf)	F_{max}-W'$_{anchor}$ (lbs)	N_P
2010.02.19_B_pullout1	18.9	14.4	12.2
2010.02.19_B_pullout2	18.3	13.6	11.9
2010.02.19_B_pullout3	18.2	11.9	10.5
2010.06.17_B_pullout1	11.6	8.2	11.4
2010.06.17_B_pullout2	11.6	8.2	11.4
2010.06.17_B_pullout3	11.6	8.3	11.5

Table 4.1 Normalized bearing factors for original model (Ganjoo, 2010)

Test ID	Approximated Su (psf)	F_{max}-W'$_{anchor}$ (lbs)	N_P
2010.06.14_C1_pullout1	10.58	8.15	10.7
2010.06.14_C1_pullout2	10.58	8.23	10.8
2010.06.14_C1_pullout3	10.58	7.99	10.5
2010.06.14_C1_pullout4	10.58	8.02	10.5
2010.06.14_C1_pullout5	10.58	8.20	10.8
2010.06.14_C1_pullout6	10.93	8.20	10.4
2010.06.17_C1_pullout1	11.48	9.94	12.0
2010.06.17_C1_pullout2	11.45	9.34	11.3
2010.06.17_C1_pullout3	11.45	9.33	11.3

Table 4.2 Normalized bearing factors for wider model (Ganjoo, 2010)

Test ID	Approximated S_u (psf)	F_{max}-W'$_{anchor}$ (lbs)	N_{S1}
2010.06.17_B_shearA_1	12.4	4.2	5.4
2010.06.17_B_shearA_2	12.4	4.2	5.4
2010.06.17_B_shearA_3	12.4	4.2	5.4

Table 4.3 Normalized shear bearing factors for original model (Ganjoo, 2010)

Test ID	Approximated S_u (psf)	F_{max}-W'$_{anchor}$ (lbs)	N_{S1}
2010.06.14_C1_shearA_1	11.73	4.59	5.4
2010.06.14_C1_shearA_2	11.73	4.39	5.2
2010.06.14_C1_shearA_3	11.73	4.52	5.4
2010.06.14_C1_shearA_4	11.73	4.44	5.3

Table 4.4 Normalized shear bearing factors for wider model (Ganjoo, 2010)

Test ID	Approximated S_u (psf)	Moment (Mmax) (in-lbs)	$N_{m,p}$ (square fluke)	$N_{m,p}$ per unit width (ft)
2010.06.11_B_pitch_1	11.40	5.26	2.46	0.62
2010.06.11_B_pitch_2	11.40	5.18	2.42	0.61
2010.06.11_B_pitch_3	11.40	5.13	2.40	0.60
2010.06.11_B_pitch_4	11.40	5.12	2.40	0.60
2010.06.11_B_pitch_5	11.40	5.08	2.38	0.59
2010.06.11_B_pitch_6	11.40	5.10	2.39	0.60

Table 4.5 Normalized pitch rotation factors for original model (Ganjoo, 2010)

Test ID	Approximated s_u (psf)	Moment (Mmax) (in-lbs)	$N_{m,p}$ (square fluke)	$N_{m,p}$ per unit width (ft)
2010.06.11_C1_pitching_2	9.97	5.75	2.49	0.67
2010.06.11_C1_pitching_3	9.97	5.49	2.38	0.64
2010.06.11_C1_pitching_4	9.97	5.50	2.38	0.64
2010.06.11_C1_pitching_5	9.97	5.48	2.37	0.64
2010.06.11_C1_pitching_6	9.97	5.50	2.38	0.64

Table 4.6 Normalized pitch rotation factors for wider model (Ganjoo, 2010)

4.2 DRAG EMBEDMENT TEST

The objective of the second phase of model testing is to calibrate the simplified prediction model for the drag trajectory of the anchor. A 12-foot long thermos-plastic tank filled with a test bed of marine clay will be used in these model tests (Figure 4.5). The undrained shear strength of the test bed versus depth will be characterized using an in situ T-bar test (e.g., El Sherbiny 2005 and McCarthy 2011). In the middle of the thermos-plastic tank, a magnetometer source is placed on the top of the tank. The source is used to receive the signal from a magnetometer sensor attached to the anchor to track its position and orientation in all six degrees of freedom (e.g., McCarthy 2011). The loading system consists of an anchor line, the electric motor, a load cell, and pulleys. One end of the anchor line is connected to the anchor at the padeye. The other end of the anchor line passes through the pulley and is connected to the bottom of the load cell. The pulley is located at the ending point of the test and close to the mudline. The load cell is connected with the electric motor, which pulls the anchor line at a constant rate of displacement. As the anchor dives and approaches the pulley, the anchor line will gradually become steeper.

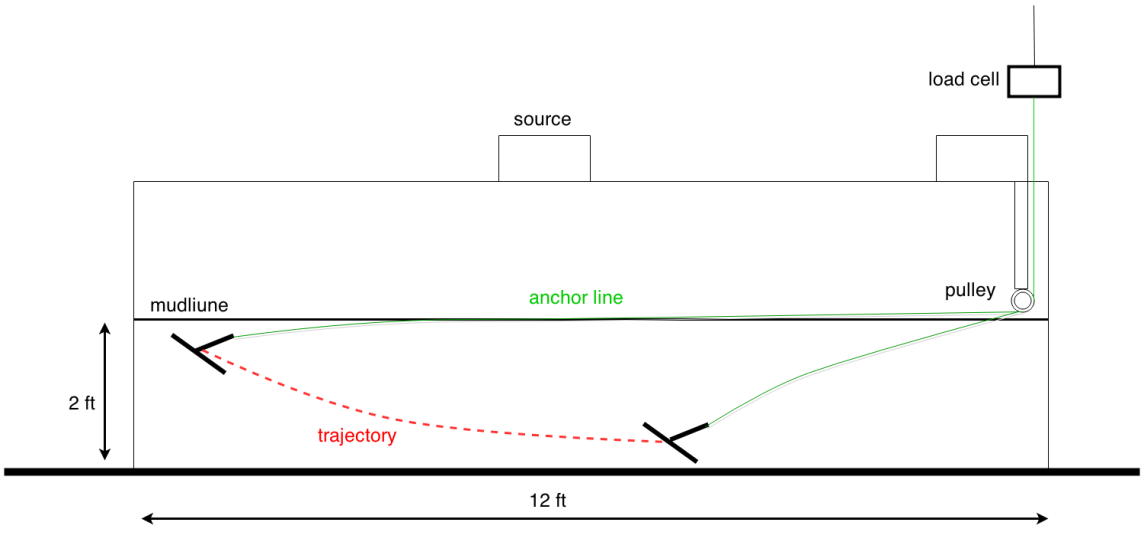

Figure 4.5 Example of a drag embedment test in 12-foot thermo-plastic tank

The variables of interest in a drag test include the location and orientation of the anchor and the load on the anchor line. An example set of results from previous testing on a conventional Drag Embedment Anchor is shown in Figure 2.13 for illustrative purposes.

The coupling with the line model and the shape of the yield interaction surface between normal and shear loading on the anchor are the primary focus of these dive tests. Therefore, the tests are designed with the simplified predictive model by varying the diameter of the line, the area of the fluke, the depth of initial embedment and the initial pitch angle, to capture different points along the yield interaction surface (Figure 4.6). The proposed testing plan is summarized in Table 4.7.

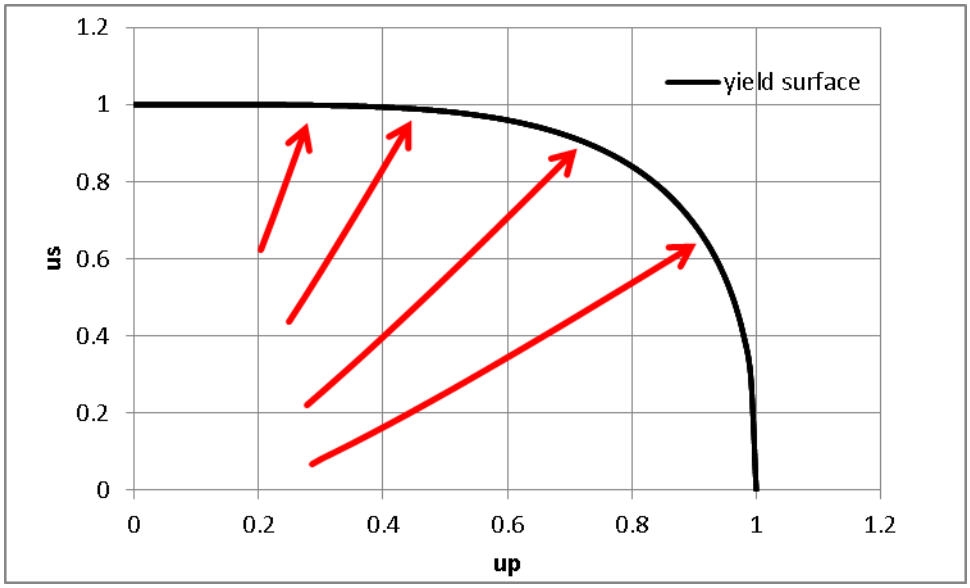

Figure 4.6 Example of drawing yield interaction surface

Test	Target	Reason
Calibration factors test for electric facilities	*Calibration factors used in a new data acquisition system (Chapter 5)*	*The calibration factors are changing a little during different tests. To obtain precise readings from the electric facilities, we need re-calibrate the calibration factors.*
T-bar test (Chapter 5)	*Undrained shear strength of the soil in test bed*	*T-bar test is an in situ test to measure the undrained shear strength of the soil in the test bed*
Drag embedment test in small thermos-plastic tank	*Depth of the test bed, length of test bed*	*Previous tests are needed before the test in the big thermos-plastic tank, which give an insight to see whether the dimension of the test bed is fitted for the size of the anchor model.*
Pure bearing factors tests	N_{nmax}, N_{tmax}, *and* N_{mmax}	*This is the first phase of model testing to measure the bearing capacities for the model-scale anchor.*
Drag test (before anchor starts to dive)	*Exponent factors (q, n, p) in the yield function*	*This test captures different points along the yield interaction surface*
Drag embedment test in large thermos-plastic tank	*Trajectory of the anchor during dive*	*Calibrate the simplified prediction model for the drag trajectory of the anchor*

Table 4.7 Proposed testing plan

A set of parametric analyses have been conducted using the simplified predictive model for drag trajectory in order to establish a testing plan. The testing conditions that can be varied include the anchor line diameter, the initial embedment depth, the initial pitch angle of the anchor and the size of the anchor. The input parameters for this analysis are be found in Table 4.8.

Input Share		
Line Parameters		
shape	1	1: wire 2: chain
En	1	Chain multiplier, 1 for wire, 2.5 for chain
d (inch)	0.40625	diameter of line
b (inch)	0.40625	effective diameter of line
d (ft)	0.033854	diameter of line
b (ft)	0.033854	effective diameter of line
Soil Parameters		
Su0(psf)	10	undrained shear strength at mudline
k (psf/ft)	1	gradient of profile
miu	0.4	friction coefficient
Bearing Capacity Factor		
Nc_mudline	5.1	where Nc increases at the mudline to 7.6 at a depth of z=2.4b
Nc_break in	7.6	
Other		
θ0* (degree)	5	angle at mudline
θ0* (radius)	0.087266	
Z_D (inch)	4	initial embedment depth
A (in.^2)	25	the area of fluke
yield function input		
q	4.43	
n	4.19	
p	1.57	
Ns	4	Moment Bearing Capacity Factor
Np	12.5	Shear Bearing Capacity Factor
Nm	2.5	Normal Bearing Capacity Factor
Dive Initiation input		
e/A^0.5	1	Length from centroid to padeye in closed position
A^0.5/b	7.3846	Square root area of anchor divided by diameter of chain
z/A^0.5	1.3333	modified depth of embedment

Table 4.8 Experimental tests anchor analysis input

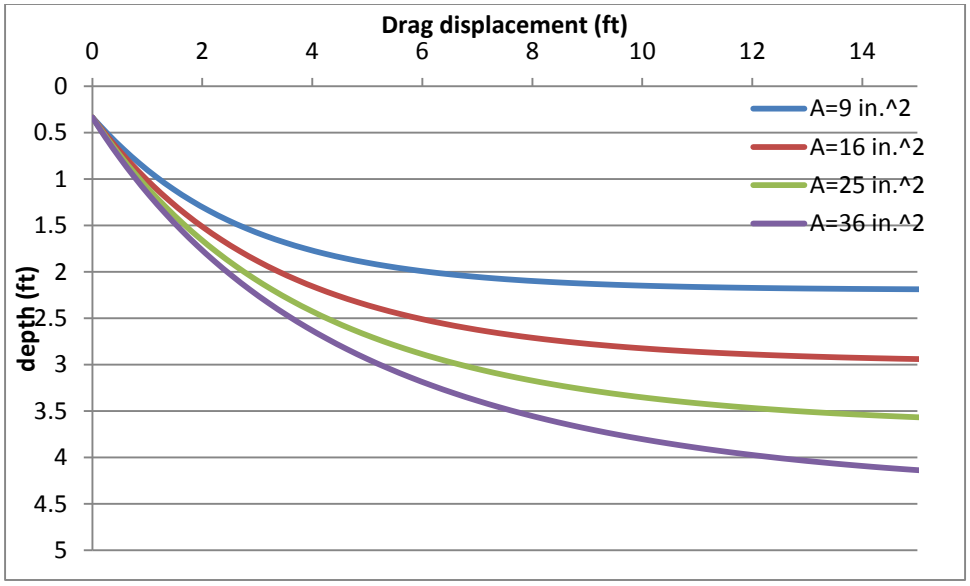

Figure 4.7 Trajectories of different fluke areas with 1/8 inch diameter line

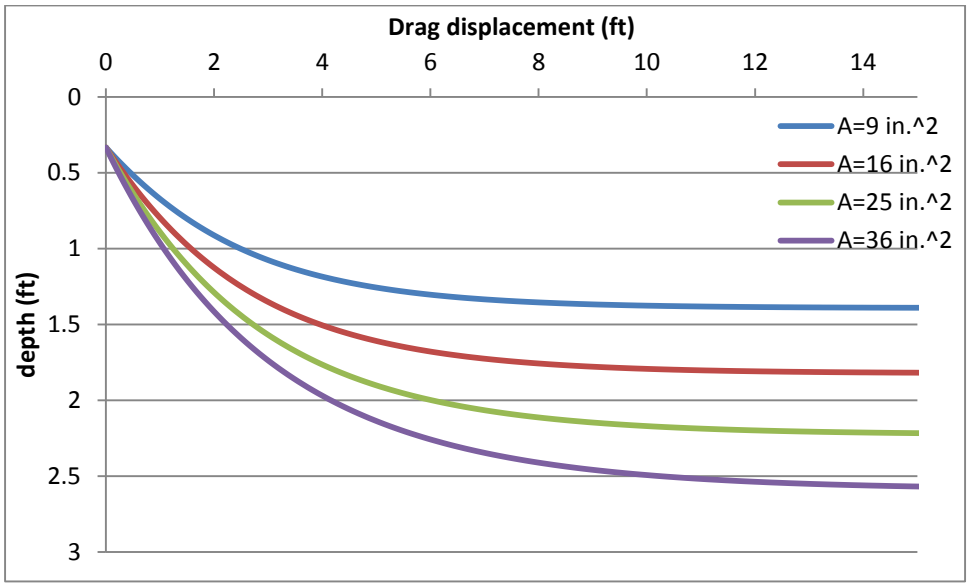

Figure 4.8 Trajectories of different fluke areas with 13/38 inch diameter line

Figure 4.7 and Figure 4.8 shows the trajectories of the anchors with different areas in the thin and thick lines conditions. In Figure 4.7, even the anchor with 9 $inch^2$

fluke dives more than 2 ft. In the thin line condition, 12 ft drag distance is not enough for the anchor with 36 $inch^2$ fluke to reach the ultimate depth and the ultimate depth is much larger than 2 ft. In Figure 4.8, the anchors with 9 $inch^2$ and 16 $inch^2$ dive less than 2 ft. In the thick line condition, four anchors approximately obtain the ultimate depth when the drag distance reaches 12 ft. So the anchor model which has a 16 $inch^2$ area fluke with a 13/38 inch diameter line may be a good first trial for future experimental tests.

Thin Line		**Thick Line**	
$\boldsymbol{A\ (Inch^2)}$	$\boldsymbol{T_o\ (lbs)}$	$\boldsymbol{A\ (Inch^2)}$	$\boldsymbol{T_o\ (lbs)}$
9	6.7	9	6.2
16	12.3	16	11.6
25	19.5	25	18.7
36	28.5	36	27.5

Table 4.9 Ultimate tensions in the thin and thick line conditions

Table 4.3 shows that the ultimate tension is proportional to the area of the fluke. The maximum tension is 28.5 lbs. According to our lab experience, the frame of the experimental system is able to hold the maximum tension. The ultimate tension will not be a factor to limit the area of the fluke.

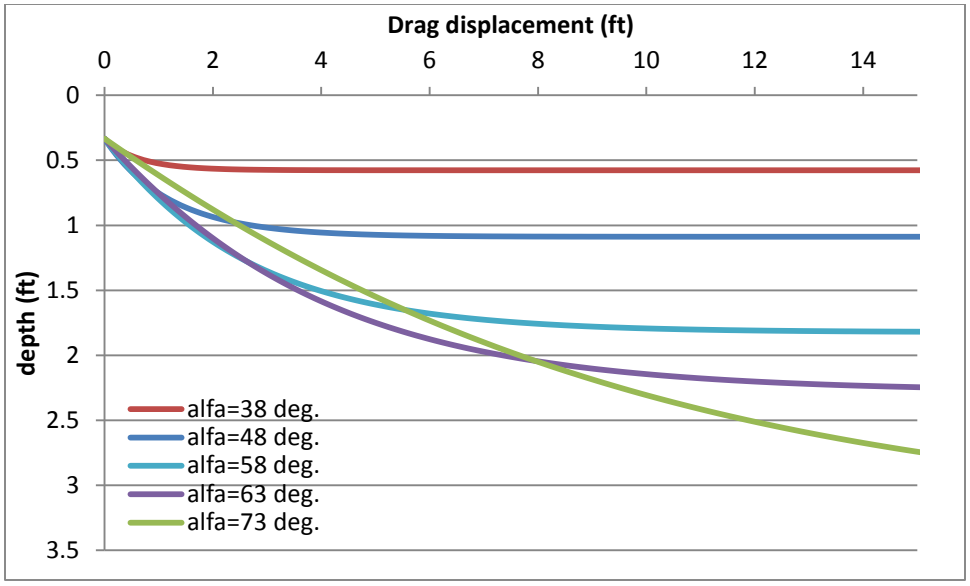

Figure 4.9 Comparison of trajectories with different α in thick line

Figure 4.9 shows the trajectories with different α with 16 $inch^2$ fluke in the thick line condition. The α values, $38°$, $48°$, $58°$, $63°$, $73°$ are corresponded to different $\beta_{threshold}$ $5°$, $15°$, $25°$, $30°$, $40°$.

4.3 Summary of Plan for Experimental Tests

The proposed experimental plan consists of two phases. The first phase includes tests to measure the pure normal bearing factor, the pure shear bearing factor, and the pure moment bearing factor. The second phase of the plan consists of tests to calibrate the simplified model to predict the trajectory of the anchor after it has been embedded by free fall. The specific objectives of the second phase are to (1) calibrate the interaction between the anchor line and the anchor during dive and (2) calibrate the yield interaction surface between shear and normal loading on the anchor during dive. A set of drag tests has been proposed that is intended to satisfy these objectives by varying the diameter of the line, the area of the fluke, the depth of initial embedment and the initial pitch angle.

Chapter 5: Development of Data Acquisition System for Model Tests

In this chapter, the development of a new data acquisition system for performing model tests on the Flying Wing Anchor is presented. First, the experimental facilities are described. Next, two new LabVIEW programs are developed and presented: (1) a Data Acquisition program that records data from measurement sensors to monitor the performance of the anchor and (2) a Motion Control program that controls the movement of the electric motor for loading the anchor. Last, the new data acquisition system is demonstrated with a test.

5.1 Experimental Facilities

The experimental facilities consist of displacement sensors, load cells, an electric motor, a magnetometer sensor.

5.1.1 LVDT displacement sensors

Figure 5.1 Linear Variable Displacement Transducer sensor

The model of the LVDT (Linear Variable Displacement Transducers) is Schaevitz Sensors8 5000 DC-EC (Rami, 2005) (Figure 5.1). These LVDT sensors are used for measuring relatively small displacements ranging from minus five to plus five inches. A needle in the LVDT sensor controls the output voltage (V) to sense the displacement (X). The actural displacement is calculated through the voltage multiplied by the calibration factor (A)

$$X = A * V \qquad Equation\ (5.1)$$

Figure 5.2 shows outputs from the LVDT displacement sensors from a load test on monotonic pile.

F	D:\Box Sync\Lab Tests\2015_04_10\NC_GoM_Clay_M1_Monotonic_Load_Controlled_Test2.txt							
O								
N	TIME	LOAD	R_LOAD	LVDT	R_LVDT	LMT	R_LMT	R_Motion
D	54:29.2	-0.5639	-0.6862	-0.6551	4.7031	0	0	0
D	54:29.4	-0.5608	-0.6864	-0.655	4.7023	0.0002	0	0
D	54:29.6	-0.5602	-0.6864	-0.6551	4.7026	0.0001	0	0
D	54:29.8	-0.5596	-0.6864	-0.655	4.7021	-0.0002	0	0
D	54:30.0	-0.5573	-0.6866	-0.6551	4.7025	0	0	0
D	54:30.2	-0.5567	-0.6866	-0.655	4.7023	-0.0004	0	0
D	54:30.4	-0.5506	-0.687	-0.655	4.7023	0.0005	-0.0001	0
D	54:30.6	-0.5531	-0.6868	-0.655	4.7024	-0.0004	0.0001	0
D	54:30.8	-0.5496	-0.687	-0.6551	4.7025	0.0004	0	0
D	54:31.0	-0.5487	-0.6871	-0.655	4.7021	-0.0009	0.0001	0
D	54:31.2	-0.5496	-0.687	-0.6542	4.6965	0.0005	-0.0001	0
D	54:31.4	-0.555	-0.6867	-0.6512	4.6749	-0.0007	0.0001	0
D	54:31.6	-0.5492	-0.6871	-0.6503	4.6684	0.0006	-0.0001	0
D	54:31.8	-0.5463	-0.6872	-0.6503	4.6681	-0.0008	0.0001	0
D	54:32.0	-0.5439	-0.6874	-0.6503	4.6681	0.0002	0	0
D	54:32.2	-0.5422	-0.6875	-0.6498	4.6647	-0.0004	0.0001	0
D	54:32.4	-0.539	-0.6877	-0.6498	4.6644	0.0002	0	0
D	54:32.6	-0.5334	-0.688	-0.6498	4.6647	-0.0001	0	0
D	54:32.8	-0.5323	-0.6881	-0.6498	4.6646	0.0002	0	0
D	54:33.0	-0.532	-0.6881	-0.6498	4.6646	-0.0005	0.0001	0
D	54:33.2	-0.529	-0.6883	-0.6498	4.6648	0	0	0
D	54:33.4	-0.5281	-0.6884	-0.6498	4.6645	-0.0003	0	0
D	54:33.6	-0.525	-0.6886	-0.6498	4.6649	0.0002	0	0
D	54:33.8	-0.5241	-0.6886	-0.6498	4.6645	-0.0003	0	0
D	54:34.0	-0.5298	-0.6883	-0.647	4.6444	0.0003	0	0

Figure 5.2 Output data of LVDT and load cell in a monotonic pile test

The data in the LVDT column are the real displacements and the data in R_LVDT column are the voltage signals from the LVDT displacement sensor.

5.1.2 LMT displacement sensor

Figure 5.3 Linear Motion Transducer sensor

The model of the LMT (Linear Motion Transducer) is RayecoTM model P-50 (Figure 5.3). The LMT sensor is used for measuring relatively large displacements ranging from 0 to 50 inches. The output voltage (V) of the LMT sensor changes with the

displacement (X) of a steel cube installed on the LMT track. The actural displacement is calculated through voltage multiplied by the calibration factor (A):

$$X = A * V \qquad Equation\ (4.3)$$

Figure 5.4 shows outputs from the LMT displacement sensors from a t-bar test on Gulf of Mexico soil. The data in LMT column are the real displacement and the data in R_LMT column are voltage signal from LMT displacement sensor before calibrated.

F	D:\Box Sync\Lab Tests\2015_04_15\GoM_1hour.txt							
O								
N	TIME	LOAD	R_LOAD	LVDT	R_LVDT	LMT	R_LMT	R_Motion
D	11:43.5	9.6554	-1.3176	-1.1476	8.7402	25.3516	-3.2586	-167521
D	11:43.7	9.5482	-1.3109	-1.1484	8.7465	25.5154	-3.2796	-166670
D	11:43.9	9.4443	-1.3045	-1.1468	8.7339	25.675	-3.3001	-165824
D	11:44.1	9.3546	-1.299	-1.1514	8.7694	25.845	-3.322	-164983
D	11:44.3	9.2627	-1.2933	-1.1546	8.7934	26.004	-3.3424	-164136
D	11:44.5	9.1492	-1.2863	-1.1567	8.8094	26.1833	-3.3655	-163285
D	11:44.7	9.1064	-1.2836	-1.1539	8.7882	26.3623	-3.3885	-162440
D	11:44.9	8.9889	-1.2764	-1.1562	8.8061	26.5329	-3.4104	-161597
D	11:45.1	8.8723	-1.2692	-1.1493	8.7529	26.718	-3.4342	-160747
D	11:45.3	8.7885	-1.264	-1.1498	8.7569	26.8971	-3.4572	-159906
D	11:45.5	8.6441	-1.2551	-1.1437	8.7102	27.0728	-3.4798	-159056
D	11:45.7	8.5496	-1.2492	-1.1409	8.6893	27.249	-3.5024	-158214
D	11:45.9	8.4896	-1.2455	-1.1478	8.742	27.4412	-3.5271	-157363
D	11:46.1	8.4382	-1.2424	-1.1517	8.7717	27.6182	-3.5499	-156520
D	11:46.3	8.337	-1.2361	-1.1529	8.7807	27.7908	-3.5721	-155671
D	11:46.5	8.2236	-1.2291	-1.1501	8.7591	27.9236	-3.5892	-154830
D	11:46.7	8.1552	-1.2249	-1.146	8.7284	28.0973	-3.6115	-153979
D	11:46.9	8.1119	-1.2222	-1.1516	8.7707	28.289	-3.6361	-153138
D	11:47.1	8.0612	-1.2191	-1.1533	8.7839	28.4721	-3.6597	-152291
D	11:47.3	8.0114	-1.216	-1.1443	8.7154	28.6302	-3.68	-151440
D	11:47.5	7.93	-1.211	-1.1529	8.7803	28.8001	-3.7018	-150598
D	11:47.7	7.844	-1.2056	-1.1527	8.7792	28.988	-3.726	-149756
D	11:47.9	7.79	-1.2023	-1.154	8.7893	29.1568	-3.7477	-148901
D	11:48.1	7.7346	-1.1989	-1.1516	8.7706	29.3336	-3.7704	-148065
D	11:48.3	7.6467	-1.1935	-1.1499	8.7581	29.5074	-3.7927	-147219
D	11:48.5	7.5474	-1.1873	-1.153	8.7814	29.6816	-3.8151	-146373
D	11:48.7	7.5288	-1.1862	-1.1505	8.7623	29.849	-3.8366	-145526
D	11:48.9	7.4391	-1.1806	-1.1509	8.7653	30.0132	-3.8577	-144671
D	11:49.1	7.387	-1.1774	-1.1552	8.7981	30.1708	-3.878	-143825
D	11:49.3	7.2904	-1.1714	-1.1524	8.7767	30.3096	-3.8958	-142978

Figure 5.4 Output data of LMT and load cell in a Gulf of Mexico soil test

5.1.3 Load cell

The load cell is manufactured by Lebow Products Inc. and its maximum load capacity is 200 lbs (Figure 5.5). The output voltage of the load cell changes with the magnitude of the force. A compressible force gives a positive voltage and a tensile force gives a negative voltage. The value of the force (F) is calculated by the voltage (V) multiplied with a calibration factor (A). Before being multiplied by the calibration factor, the voltage value needs to be transformed by subtract a zero value (B), which is the voltage when there is no load applied on the load cell:

$$F = A * (V - B) \qquad Equation\ (5.3)$$

Figure 5.5 Load cell

The outputs from the load cell are shown in Figures 5.2 and 5.4. The data in LOAD column are the calibrated loads and the data in R_LOAD column are the voltage signals from the load cell.

5.1.4 Electric motor

Loads are applied using a bilinear motion assembly powered by a Superior Electric SLO-SYN MH112-ff-206 stepper motor (Figure 5.6). The electric motor system consists of four components: (1) two linear actuators; (2) two stepper motors; (3) two translator drivers; and (4) a computer controller card. Loading with this motor system is accomplished entirely with the vertical motion, which has a maximum displacement of 12.5 inches. The rate of movement for the moment is input and the position of the motor is measured and recorded versus time.

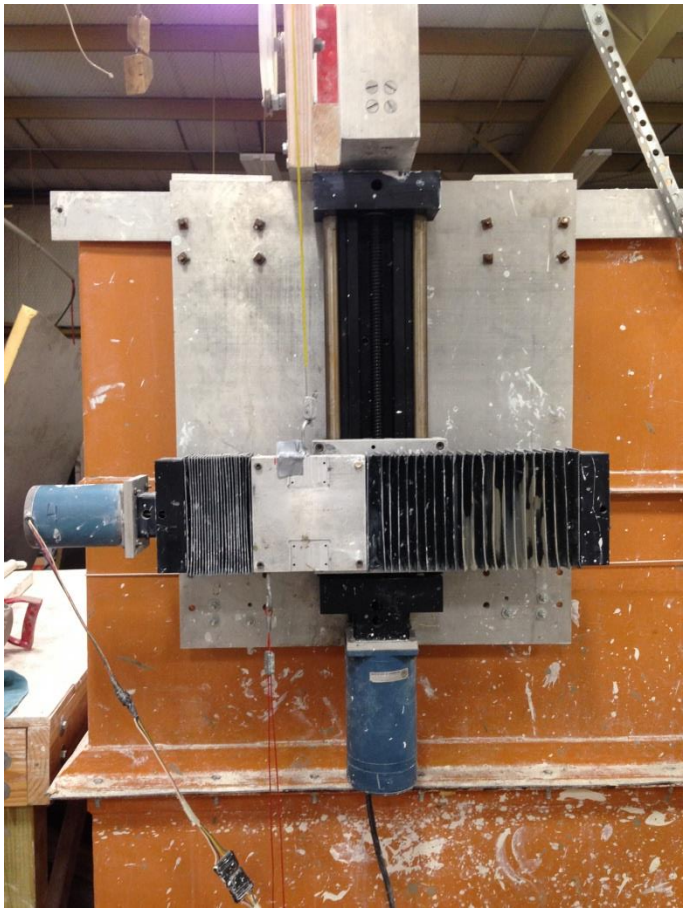

Figure 5.6 Electric motor system

We are able to input target position in inches to drive the electric motor. Figure 5.2 and Figure 5.4 show the output from the electric motor. R_motion is the raw data from the electric motor which is calibrated to obtain the actual displacement.

5.1.5 Magnetometer device

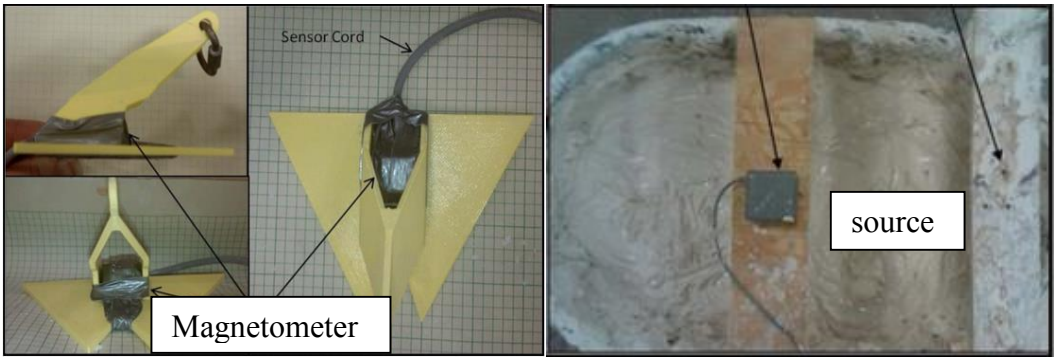

Figure 5.7 Magnetometer sensor system (McCarthy, 2011)

The magnetometer sensor system is used to track the location and the orientation of the anchor. A magnetometer sensor, a source, and a computer program constitute the system of the magnetometer sensor. The magnetometer sensor is located by an electromagnetic wave emitted by the source. The strength and the direction of the electromagnetic wave are detected by the magnetometer sensor. The program "PiMgr" is used to receive the data transformed from the sensor and the source (McCarthy, 2011).

5.2 Data Acquisition and Motion Control Programs

The Data Acquisition (DAQ) hardware and the motor control card are produced by National Instruments. In order to record data from the Data Acquisition hardware and control the electric motor, a data acquisition and motion control system is designed (Figure 5.8). LabVIEW is a development environment for a visual programming developed by National Instruments. Different from other programming languages, such as C+, LabVIEW is a data flow programming language in which its execution is determined by the structure of a graphical block diagram. This structure allows the functions in LabVIEW to be displayed and manipulated with virtual wires that show the data flow direction.

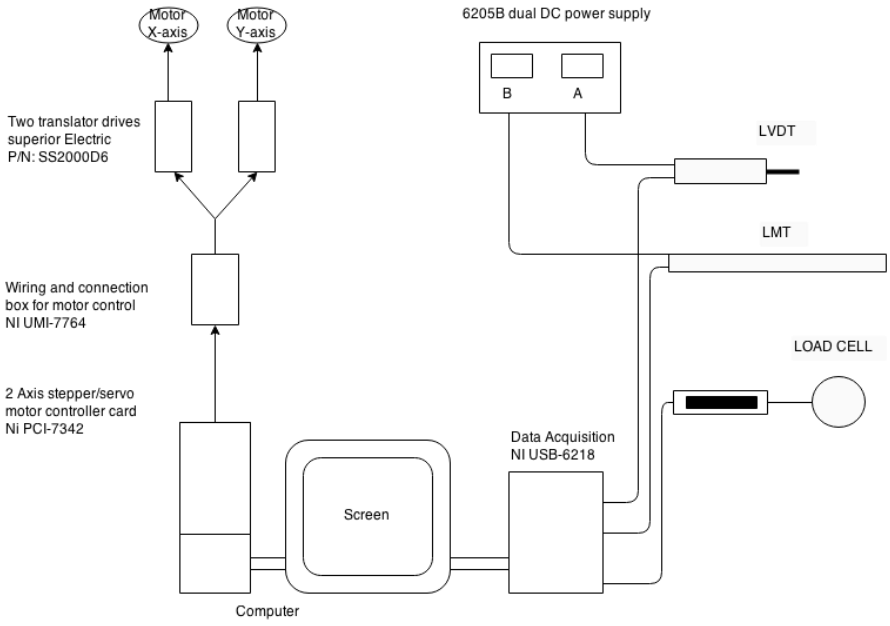

Figure 5.8 Data acquisition and motion control system

5.2.1 Data Acquisition Program

A Data Acquisition program, using LabVIEW programming language, is designed to record the readings from load cells, LVDT sensors, and the LMT sensor. With this program, the sensor measurements are recorded versus time in text data files. The layout of the Data Acquisition program is shown in Appendix II.

5.2.1.1 Data Acquisition program user interface

The user interface for data acquisition is developed using LabVIEW to interface with the DAQ hardware (Figure 5.9). The DAQ user interface is divided into five components (Figure 5.10): (1) control area; (2) file path input area; (3) calibration factors input area; (4) Load, LVDT, and LMT output area; and (5) LOAD-LVDT and LOAD-LMT output area.

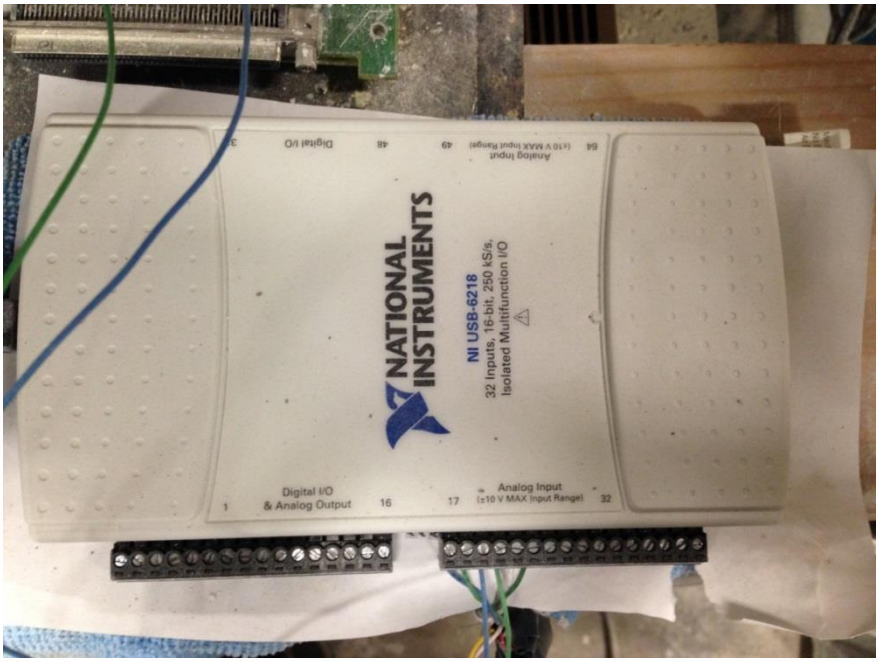

Figure 5.9 Data Acquisition hardware

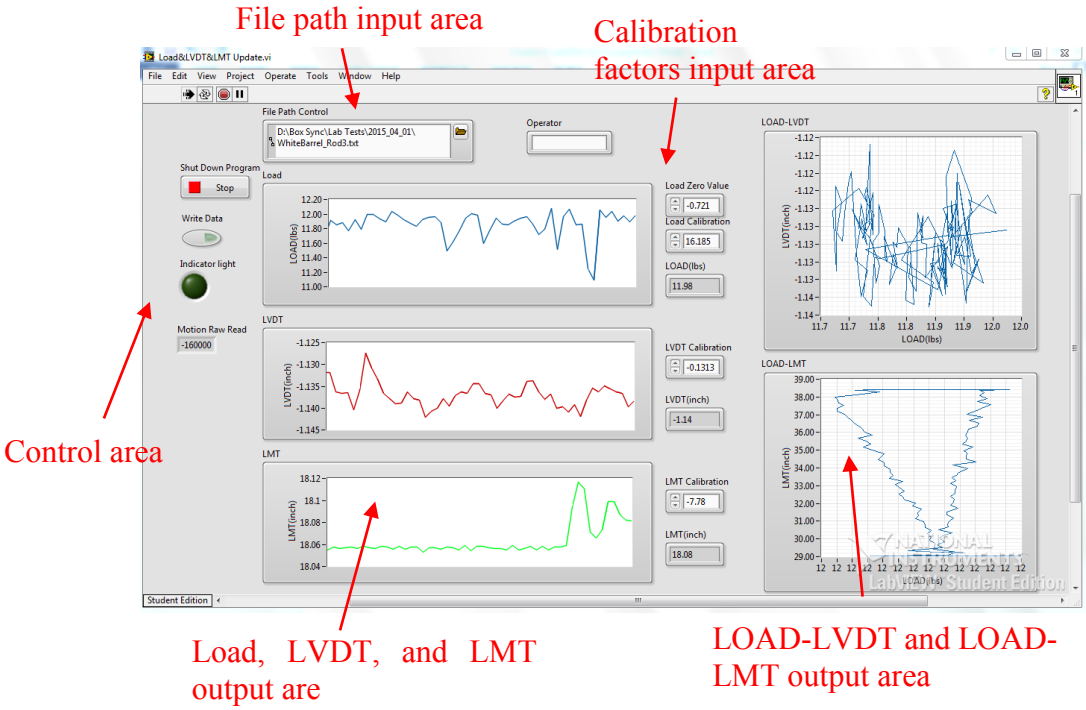

Figure 5.10 User interface of Data Acquisition program

The control area is used to activate commands to begin acquiring data, to write data into text files, and to terminate data acquisition and save the text files. The control area consists of two buttons and an indicator light (Figure 5.11). The “Writing Data” button is a “Switch When Related” button, meaning that it changes states on a button release and remains in that state until another button released. The initial status of “Writing Data” button is False and the indicator light is dark green. When the “Writing Data” button is clicked, it switches to True status, the indicator light shows light green, and LabVIEW starts to write data into a text file. If the “Writing Data” button is clicked again, its status turns back to False, the indicator light shows dark green, and LabVIEW closes the text file with the data. The “Shut Down Program” button is a “Switch Until Released” button that will terminate the program when it is clicked.

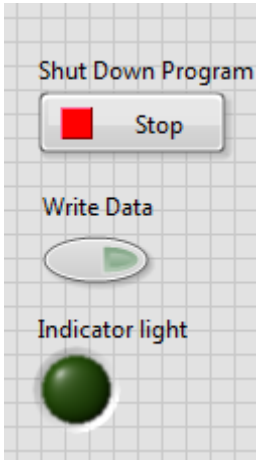

Figure 5.11 Buttons and indicator light used in DAQ user interface

The file path input area is used to input the file path and operator names for the text file containing the data. The default file path at present is: D:/Box Sync/Lab Tests/date/name.txt.

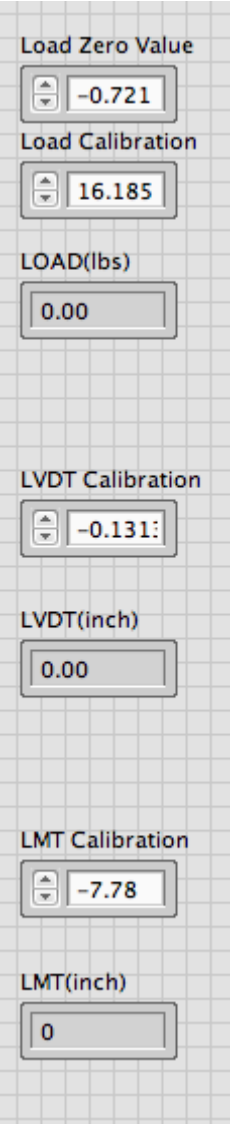

Figure 5.12 Calibration factors input area

The calibration factors input area is used for inputting the calibration factors of the sensors and showing the calibrated values (Figure 5.12). For the load cell, Load Zero Value numerical control represents B and Load Calibration numerical control represents A in Equation (5.3). For the LVDT and LMT sensors, LVDT Calibration numerical control represents A in Equation (5.1) and LMT Calibration numerical control represents the A in Equation (5.2).

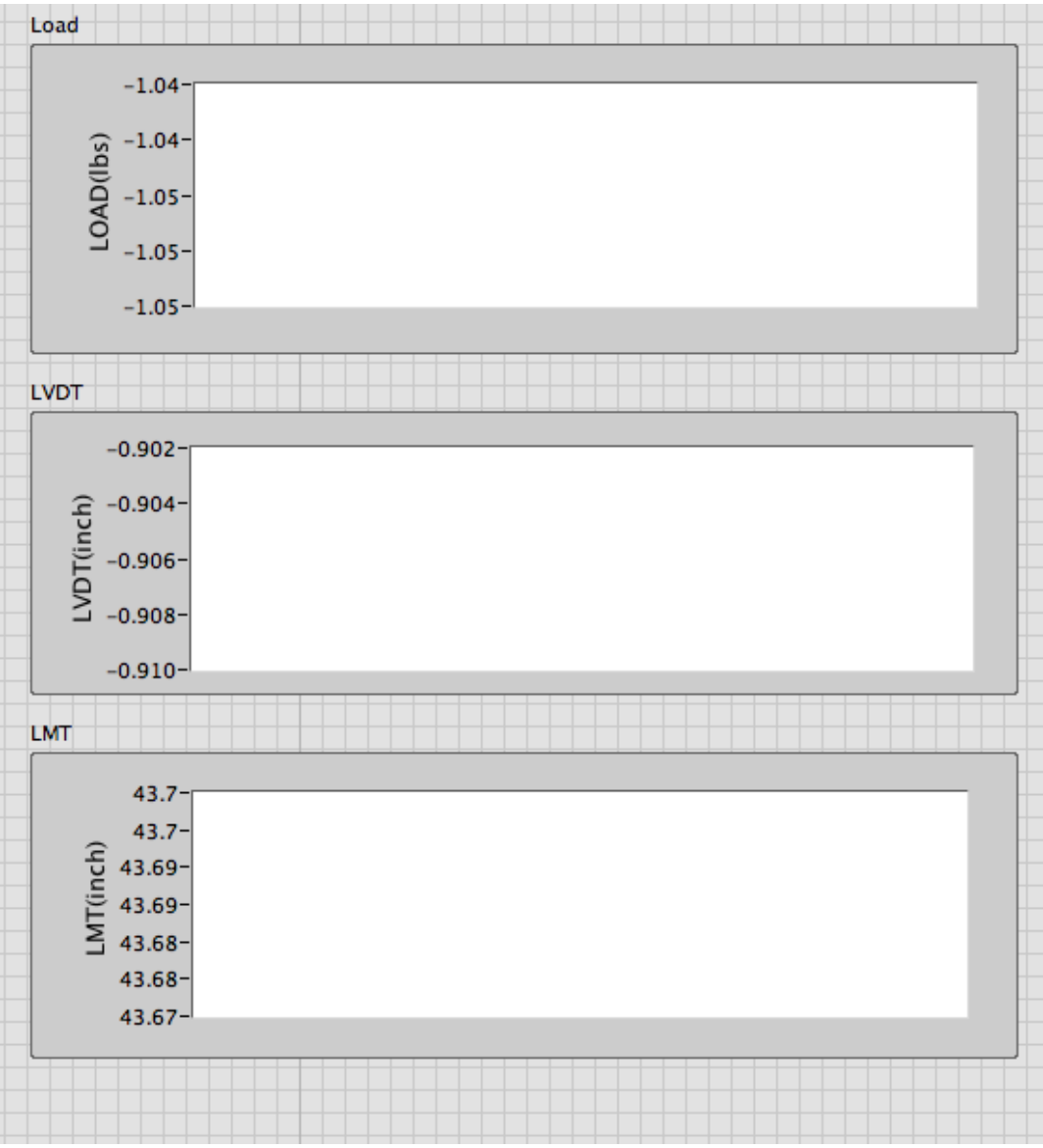

Figure 5.13 Load, LVDT, and LMT output area

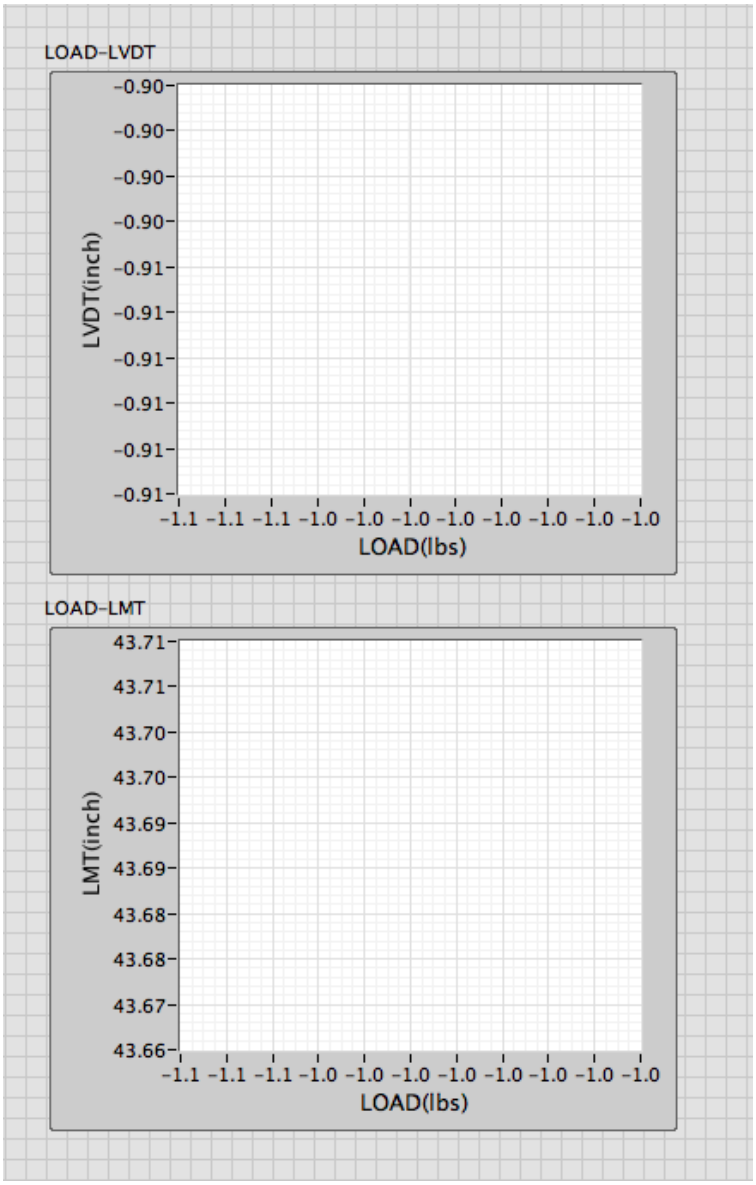

Figure 5.14 LOAD-LVDT and LOAD-LMT output area

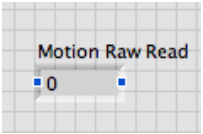

Figure 5.15 Motion Raw Read

The output areas show Load (lbs), LVDT displacement (inch), LMT displacement (inch) as numerical indicators with the calibrated readings. The LOAD, LVDT, and LMT output area shows three strip charges with the calibrated readings versus time (Figure 5.13). The running data are shown continuously scrolling from left to right across the chart. The LOAD-LVDT and LOAD-LMT output area is used to see the relationship between readings during tests synchronously (Figure 5.14). The upper chart shows the relationship between load cell and LVDT displacement sensor readings, while the bottom chart shows the relationship between load cell and LMT displacement sensor readings. Lastly, the Motion Raw Read is a numerical indicator with the step reading from the electric motor at an instant in time (Figure 5.15).

5.2.1.2 Data Acquisition program Block Diagram

To execute the command from the user interface and output data or graph on the user interface, we need to compile graphic code on Block Diagram. Block Diagram presents programming objects and functions in graphic shape. The objects are connected to their corresponding numerical controls and indicators on the user interface (the front panel). The functions are able to obtain signals and do mathematical calculations. The objects and the functions are wired to communicate data. With a combination of objects and functions, we can obtain data from the DAQ and command the movement of the electric motor.

Data Acquisition program Block Diagram consists of two main sections: (1) Data Producer section and (2) Data Consumer section. The Data Consumer section has three subsections: (1) Calibration section, (2) Chart Output section, and (3) Write Data to File section. The following relationships show the connections between these sections and the areas on user interface:

Calibration section --- Calibration factors input area and Load, LVDT, and LMT output area

Chart Output section --- LOAD-LVDT and LOAD-LMT output area

Write Data to File section --- file path input area

5.2.1.2.1 Introduction of functions and data type

Basic functions and concepts are available from LabVIEW to build the algorithms in the Data Acquisition sections:

VI (Virtual Instrument) – a program or subprogram in LabVIEW

Physical Channels – terminals receive or generate analog or digital signals (Figure 5.17)

DAQ Assistant function – a VI receives signal from target physical channels in a specific frequency

Read Position function – a VI reads and output position signal from the electric motor

Wait Until Next ms Multiple function – a VI controls the time interval to read signal from the physical channels

Build Array function – append element to the end of a array

Dynamic data - denote information that is asynchronously changed as further updates to the information become available.(Wikipedia)

Cluster – group different data elements

5.2.1.2.2 Data Producer loop

A Data Producer loop is used for obtaining data from DAQ and the electric motor in a required frequency (Figure 5.16). The algorithm of the Data Producer loop is the following:

1) DAQ Assistant function obtains the voltage readings from LVDT, LMT, and load cell sensors.
2) Read Position function reads the position signal from the electric motor.
3) The signals are combined as dynamic data for sustaining updating.
4) The dynamic data of signals are transferred to Data Consumer loop.

Figure 5.17 shows the user interface of DAQ Assistant function. The Time Settings, at the bottom of the interface, control the frequency for reading signals. The Add Channels, at the top of the interface, sets the target physical channels connected to the sensors. Figure 5.18 shows the configuration of the physical channel connections.

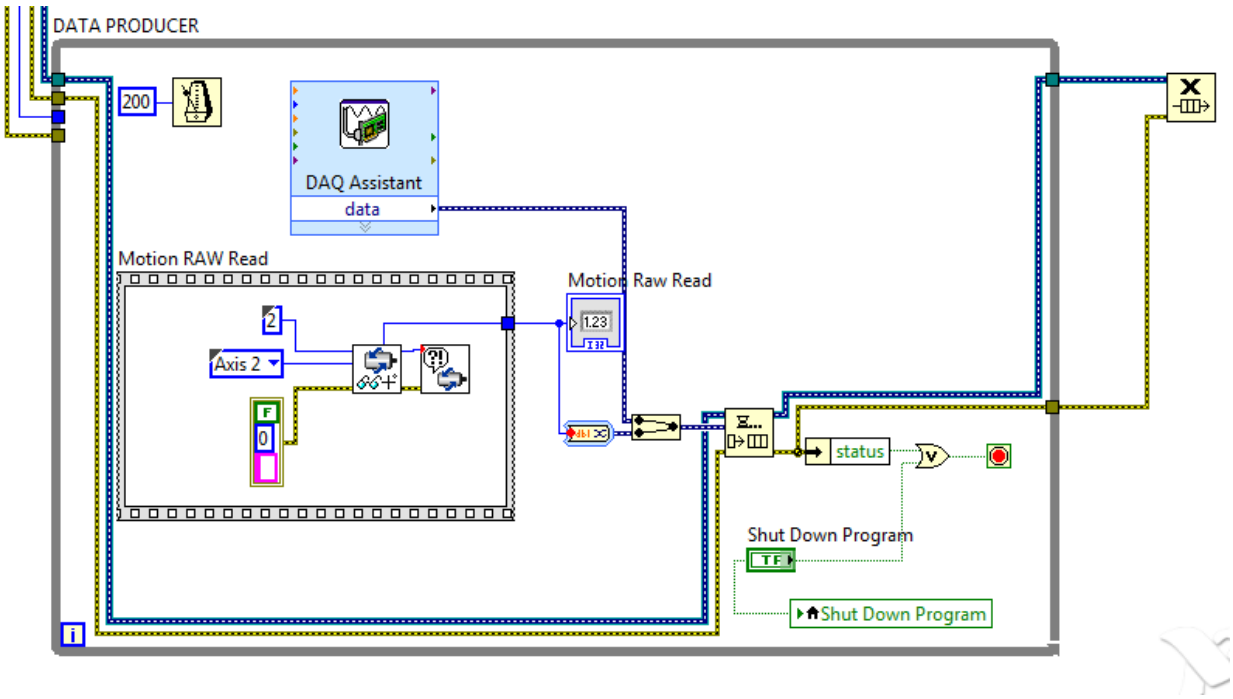

Figure 5.16 Data Producer loop

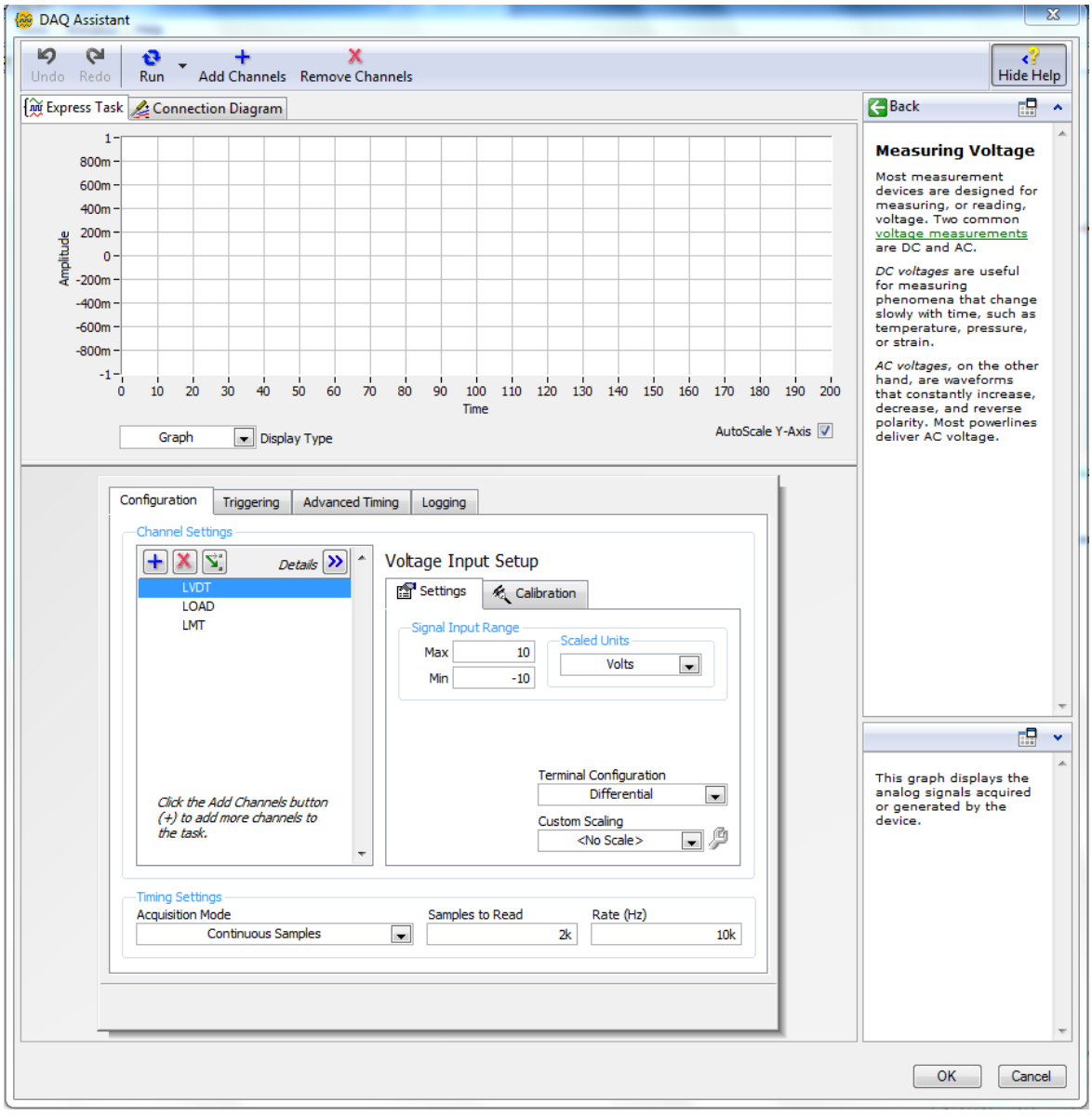

Figure 5.17 DAQ Assistant user interface

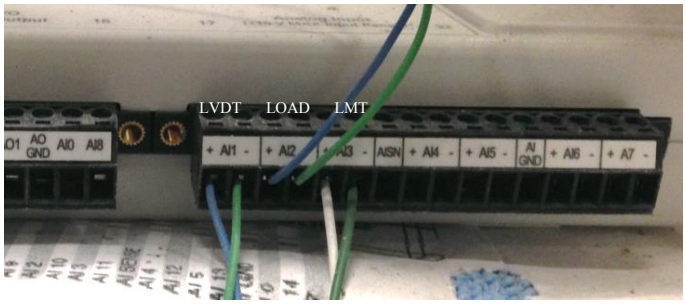

Figure 5.18 Channels connections

5.2.1.2.3 Calibration section

The Calibration section combines the raw data and the calibrated data into one cluster. The procedure of the Calibration section is the following:

1) Split the voltage value from dynamic data and transfer each voltage value to a one-dimensional array.
2) Use the mean function to obtain an average of the data in the one-dimensional array.
3) Multiply the average value with the calibration factor to obtain calibrated value.
4) Combine the voltage value and calibrated values from the LVDT, LMT, and load cells and the electric motor position value into a cluster.

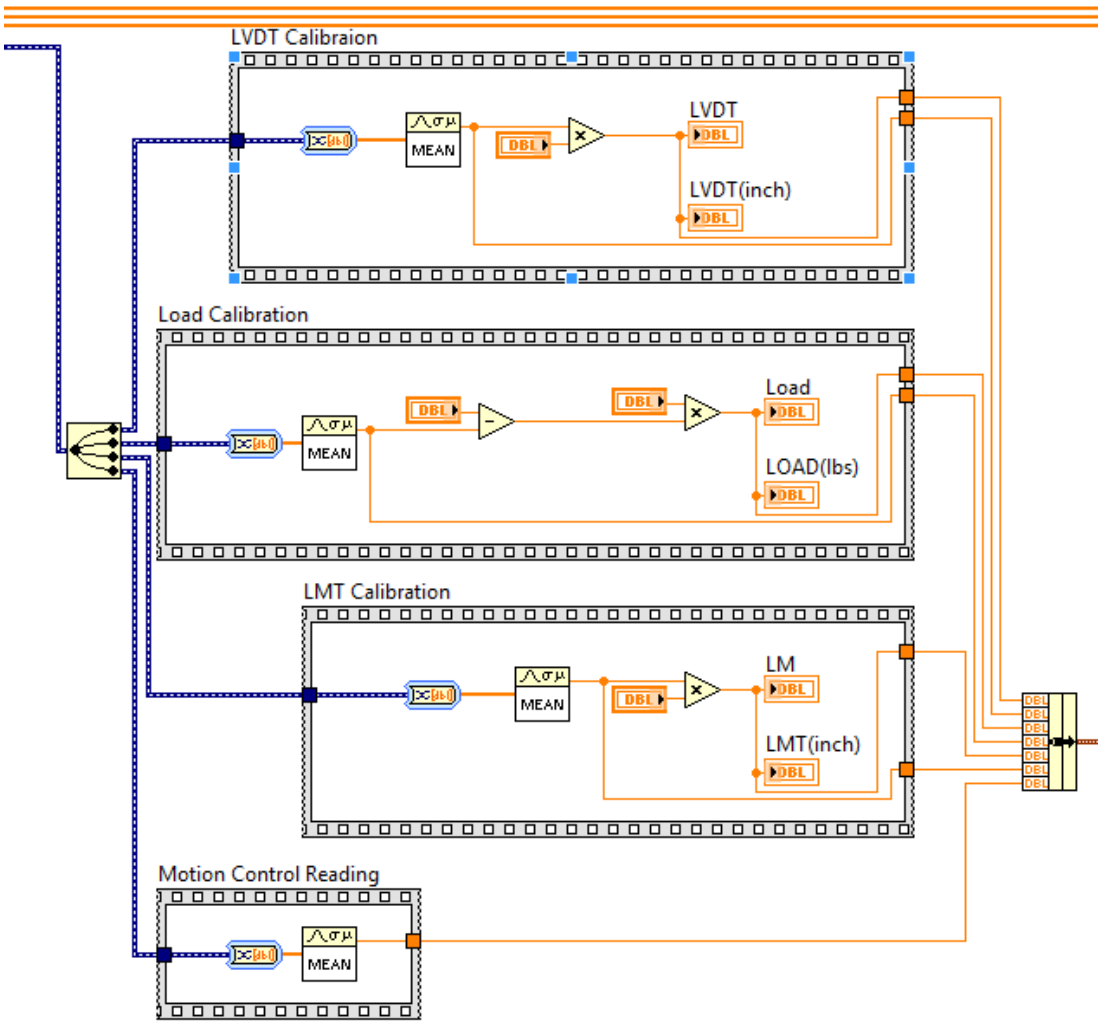

Figure 5.19 Calibration procedures

5.2.1.2.4 Chart Output section

The Chart Output area section provides the input data for the LOAD-LVDT chart and the LOAD-LMT chart (Figure 5.20). Below is the procedure for drawing these two charts:

1) Unbundle the real readings of LVDT, LMT and Load out of the cluster;
2) Use a Build Array function to generate LVDT, LMT and LOAD arrays.

3) Combine the LOAD array and LVDT array together into XY graph function and set LOAD as horizontal axis and LVDT as vertical axis.
4) Combine LOAD array and LMT array together into XY graph function and set LOAD as horizontal axis and LMT as vertical axis.

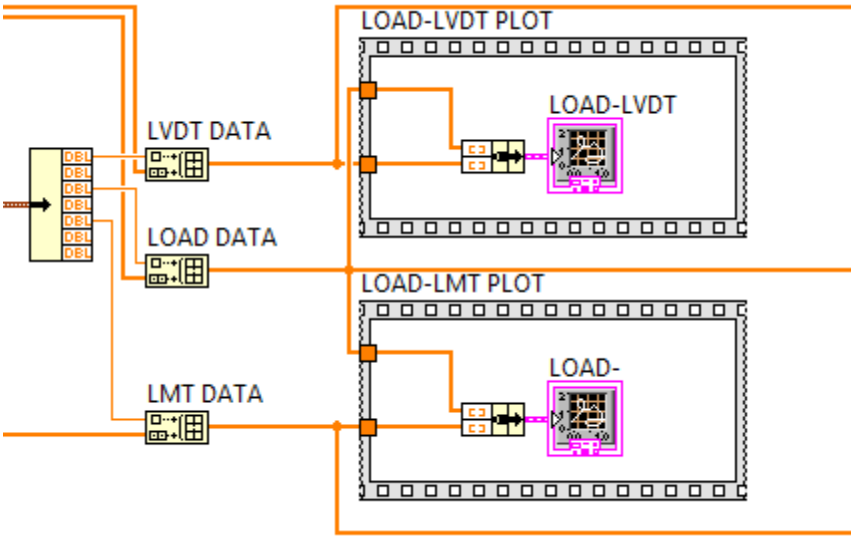

Figure 5.20 Chart Output section

5.2.1.2.5 Writing Data to File section

The Writing Data to File section (Figure 5.21) creates a text file in the computer, writes the data into the file in a specific format and saves the file to the File Path Control location. The Writing Data to File section has two phases: (1) create the file and the head titles and (2) append the data under the head titles.

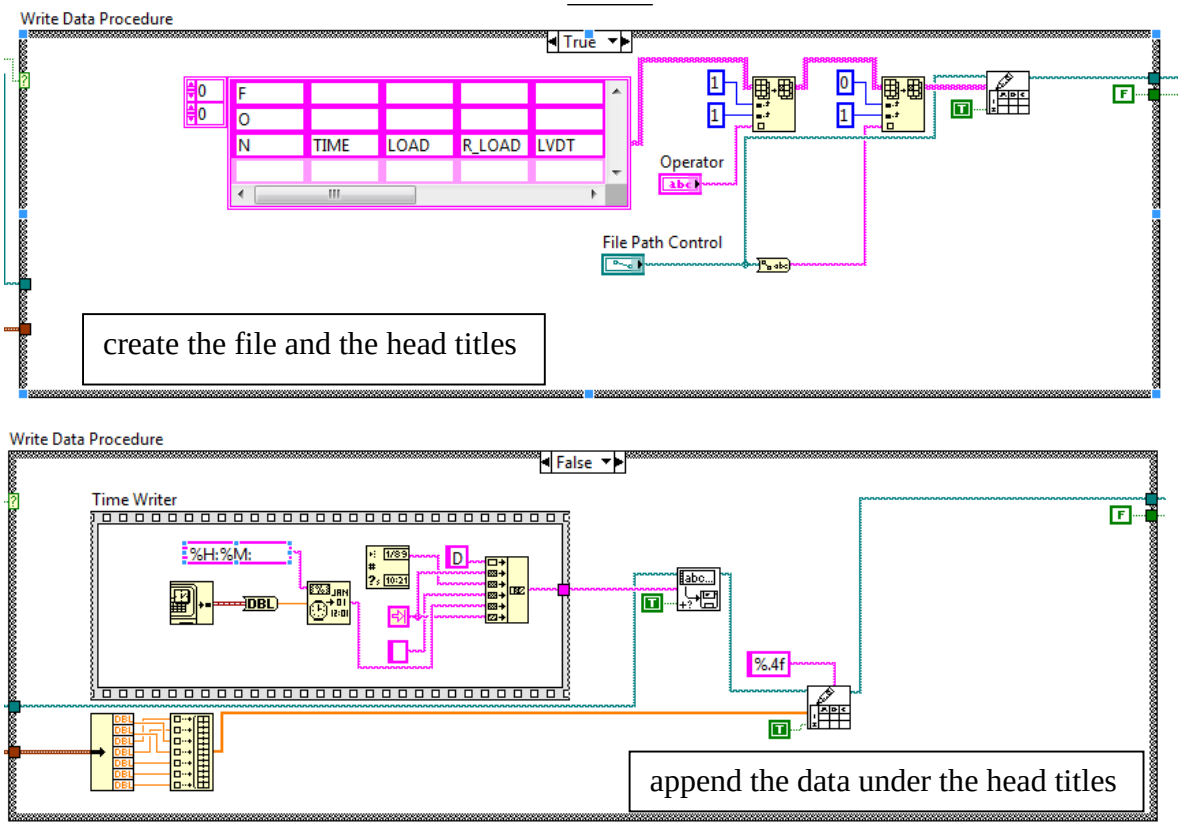

Figure 5.21 Writing Data to File section

5.2.2 Motion Control program

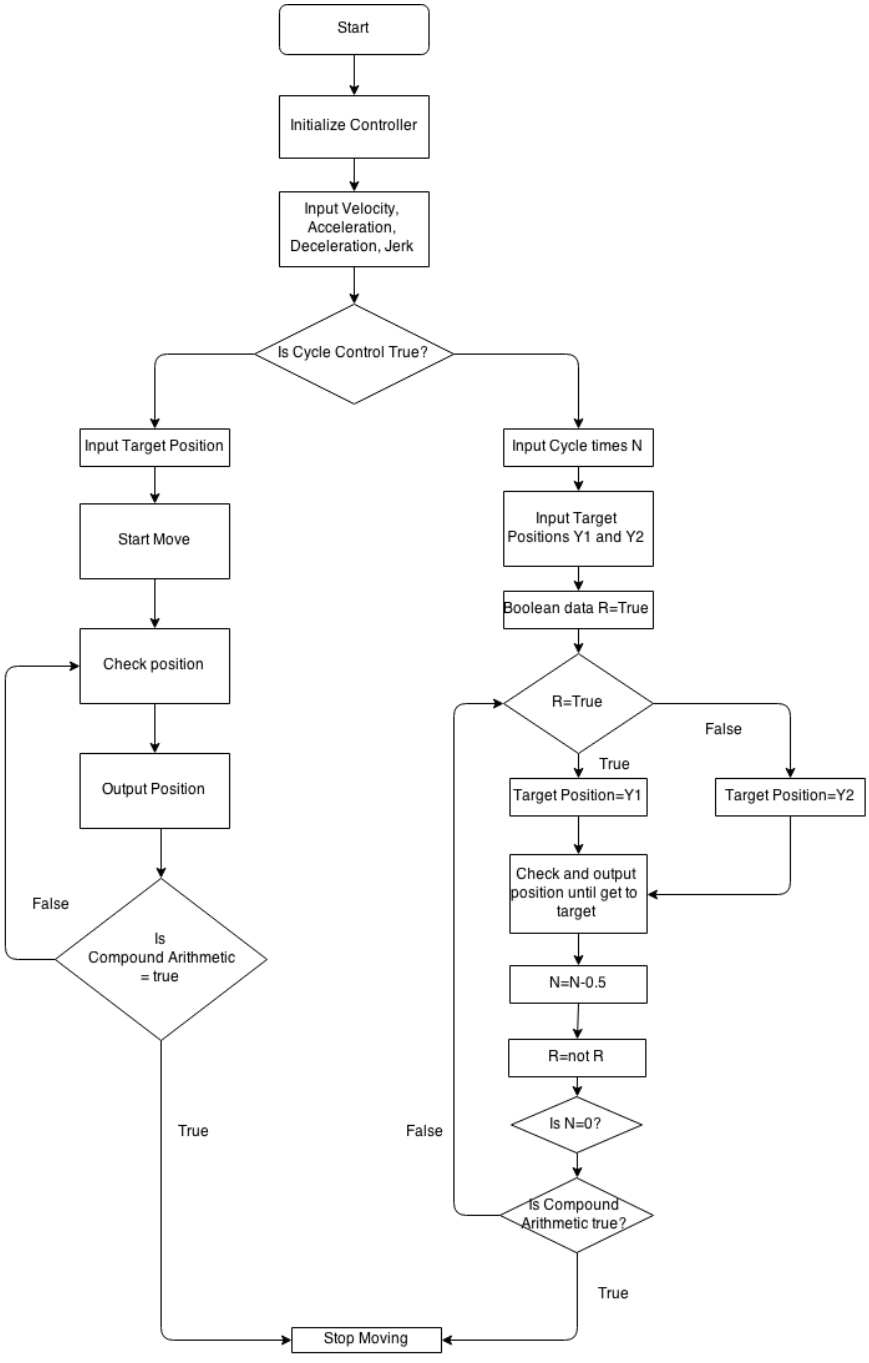

Figure 5.22 Flow chart of motion control program

5.2.2.1 Motion Control program user interface

The Motion Control program user interface is divided into three areas (Figure 5.23): Control area, One Move area, and Cycle Moves area. The Control area gives the command to move or stop the electric motor. The type of both the Move and Stop buttons is Latch When Released, which changes their state on a button release and changes it back when the control is read by LabVIEW. The Move button is used to start the motor and Stop button is used to stop the motor.

The One Move area allows operators to input parameters to control the movement: (1)Target Position: the position the electric motor goes to;(2) Velocity: the speed of the electric motor during moving; (3) Acceleration: the rate of the change of Velocity when start moving; (4)Deceleration: the rate of the change of Velocity when stop; (5) Jerk: the rate of the change of Acceleration and Deceleration . After clicking the Move button, the electric motor moves from the current position to the Target Position. The only output is the Current Position indicator, which is shown in the user interface indicator during movement.

The Cycle Moves area is used to execute the cycle moves command. Three numerical controls, a numerical indicator, and a Cycle Control button constitute this area. Cycle Y1 and Cycle Y2 define the range of cycle movement. Target Cycles sets the number of cycle times. Cycles Now indicator in the user interface shows the remaining number of cycle times. The Cycle Control button is a Switch When Released button that shows green when the electric motor is executing the cycle command.

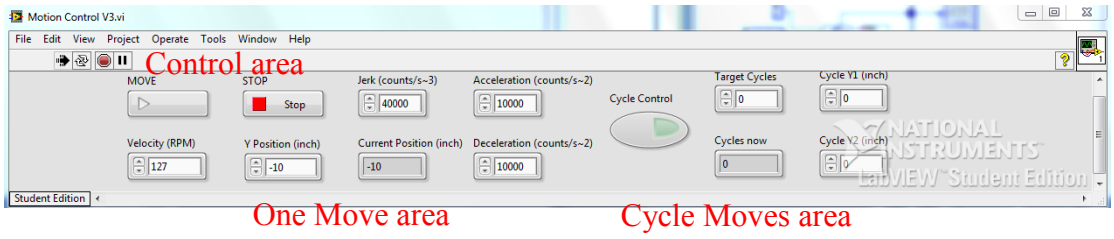

Figure 5.23 Motion Control user interface

5.2.2.2 Motion Control program Block Diagram

The layout of the Motion Control program Block Diagram is shown in Appendix II. The type of the loop used in Motion Control is the case structure. Case structure consists of several cases and chooses one of the cases to execute during execution. The Motion Control program consists of No Move case, One Move case, and Cycle Moves case. The No Move case is the default case when the electric motor stopped.

Motion Control program has following phases:

1) Decision Phase – decide which case the program executes: No Move case, One Move case, or Cycle Moves case.
2) Input Parameters Phase – input the parameters from the user interface.
3) 1D Straight-line Move Control Phase– execute input parameters and check the movement of the electric motor.
4) Stop Phase – decide when to stop the electric motor.

5.2.2.2.1 Decision Phase

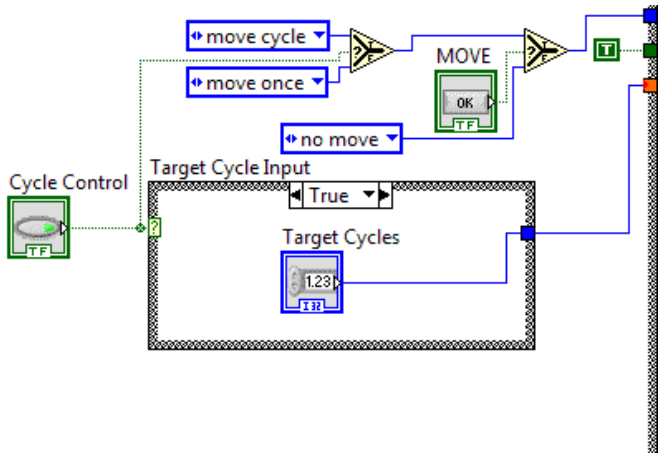

Figure 5.24 Decision Phase

Figure 5.24 shows the Decision Phase in Block Diagram. Before conducting the Data Parameters structure, the program chooses which case is to be used. If the electric motor is stopped, the program will choose the No Move case. If the operator wants to make

the motor move one time, the program will choose the One Move case. If the operator wants to make to motor move multiple times, the program will choose the Cycle Moves case.

Here is the algorithm of the Decision Phase:

1) The first decision is to choose whether to use One Move case or Cycle Moves case.

2) The second decision structure is to detect the status of the MOVE bottom. If the status of MOVE is False, go to Step 3. If the status of MOVE is True, go to Step 4

3) The program chooses the No Move case and the electric motor is stopped; go to Step 1.

4) If the first decision in Step 1 is One Move case, then the electric motor will move to the target position once; if the first decision in Step 2 is Cycle Moves case, then the electric motor will move between two target positions a specified number of times. After finishing the move, the program returns to Step 1.

5.2.2.2.2 Input Parameters Phase

Input Parameters Phase reads the Target Position, Velocity, Acceleration, Deceleration, and Jerk from the user interface. Then the phase combines the reads into a cluster and transfer it to 1D Straight-line Move Control Phase. Only Y position input is calibrated because the unit of Y position is needed to be transferred to inches from counts.

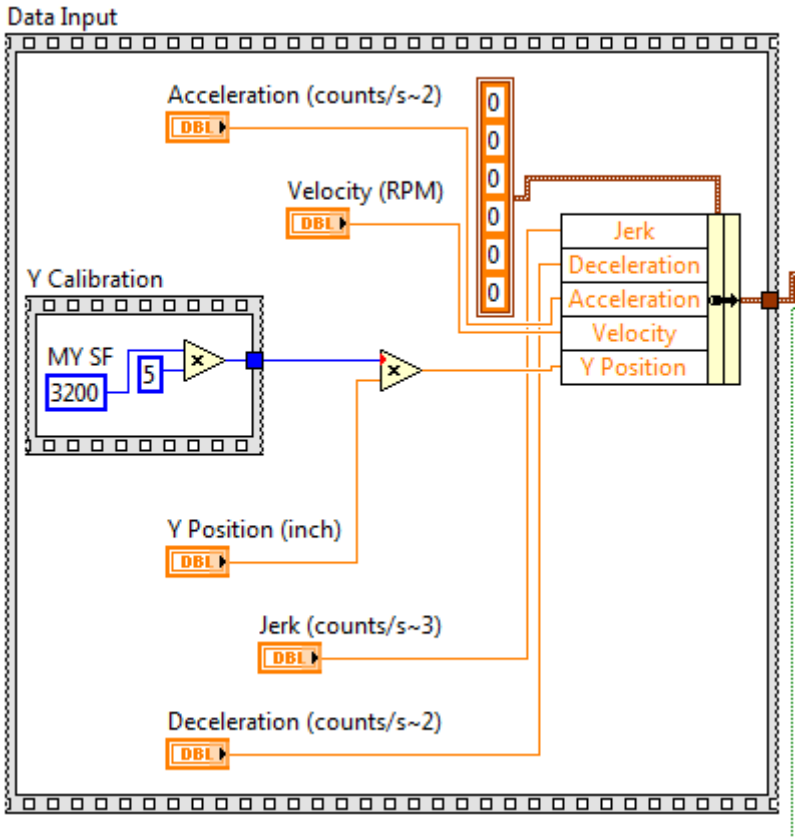

Figure 5.25 Input Parameters Phase

5.2.2.2.3 1D Straight-line Move Control Phase

A 1D Straight-line Move Control Phase consists of a Data Consumer section and a Check Movement section. Figure 5.26 shows the configuration of the Data Consumer section which commands the electric motor to start moving. Figure 5.27 shows the configuration of the Check Movement section, which reads the position of the electric motor and decides when to stop moving. A straight-line move algorithm is used in 1D Straight-line Move Control Phase:

1) Use board ID to identify motion controller; the board ID is assigned by Measurement & Explorer (MAX) manually (Data Consumer section). Measurement & Explorer is the software to configure National Instrument hardware and software.

2) Input the values in the cluster to the corresponding functions (Data Consumer section).
3) Start motion.
4) Check and read the current position in a loop (Check Movement section).
5) Stop when the move completes, the stop button activates, or the other statuses go False (Check Movement section).

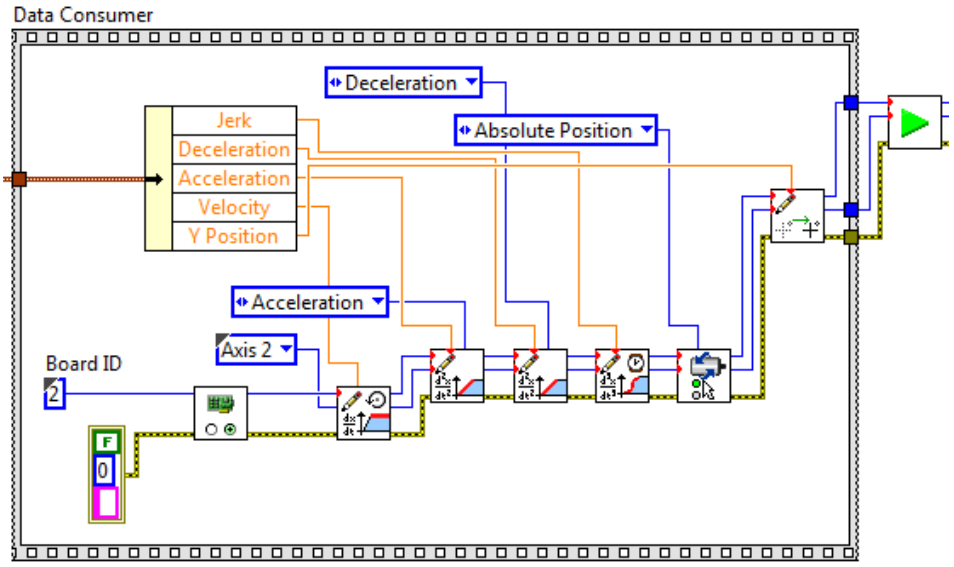

Figure 5.26 Data Consumer section

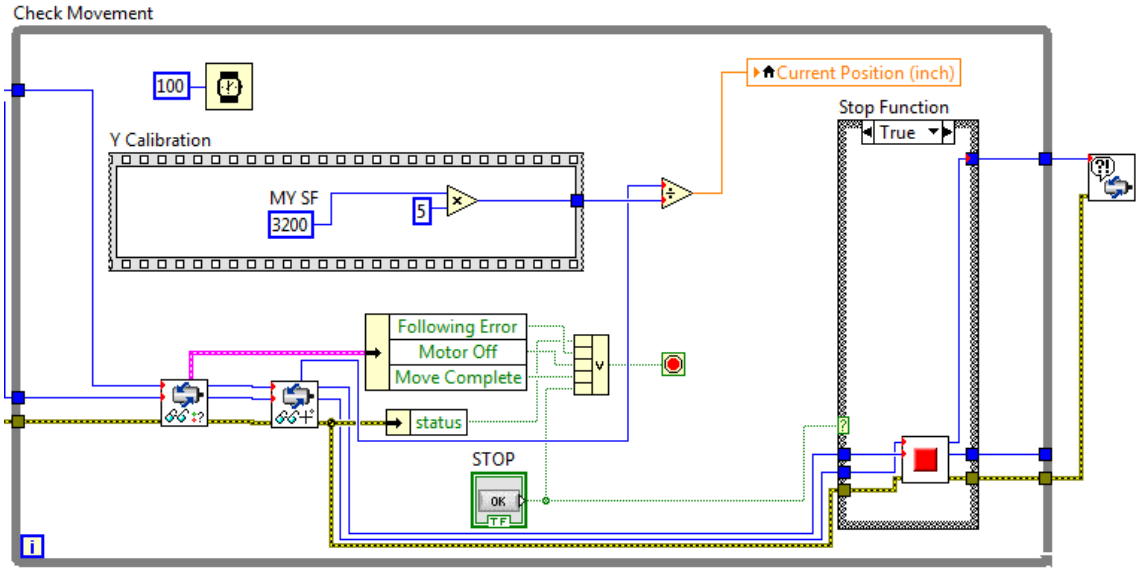

Figure 5.27 Check Movement section

5.2.2.2.4 Stop Phase

The stop conditions are different between the One Move case and Cycle Moves case. The stop condition of the One Move case is when the current position equals the target position. In the Cycle Moves case, the stop condition is when the Cycles now indicator equals to zero.

Figure 5.28 shows the configuration of the stop condition in the Cycle Moves case. In this case the program has two target positions, Y1 and Y2. Here is the algorithm for the stop condition in the Cycle Moves case:

Step 1) Input an integer number for the Target Cycles

Step 2) Move the electric motor to Y1 and set the Cycles now variable to minus 0.5.

Step 3) Check the Cycles now variable. If the Cycles now variable equals to zero, stop the motor. If the Cycles now variable does not equal zero, go to Step 4.

Step 4) Move the electric motor to Y2 and set the Cycles now variable to minus 0.5.

Step 5) Check the Cycles now variable. If the Cycles now variable equals to zero, stop the motor. If the Cycles now variable does not equal zero, go to Step 2.

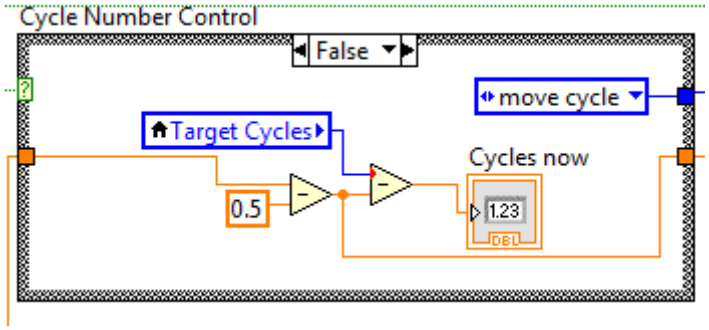

Figure 5.28 Stop Phase

5.3 Demonstration of Data Acquisition and Motion Control Programs

To verify the application of the Data Acquisition and Motion Control program, we conducted a T-bar test on Gulf of Mexico soil. First, the T-bar test is introduced. Then the results of the T-bar test are presented.

5.3.1 Introduction of T-bar test

We conducted a T-bar test to verify the operation of the Data Acquisition and Motion Control programs. The T-bar test is an in situ test to measure the undrained shear strength of the soil in the test bed. The T-bar is an cylindrical probe with a 1-inch diameter and a 4-inch length. A steel rod is connected with the T-bar probe at the bottom of the rod. A stack of weight is put at the top of the rod to push the T-bar into the soil during the test (Figure 5.29), and a line under tension connected to the motor controls the rate of penetration.

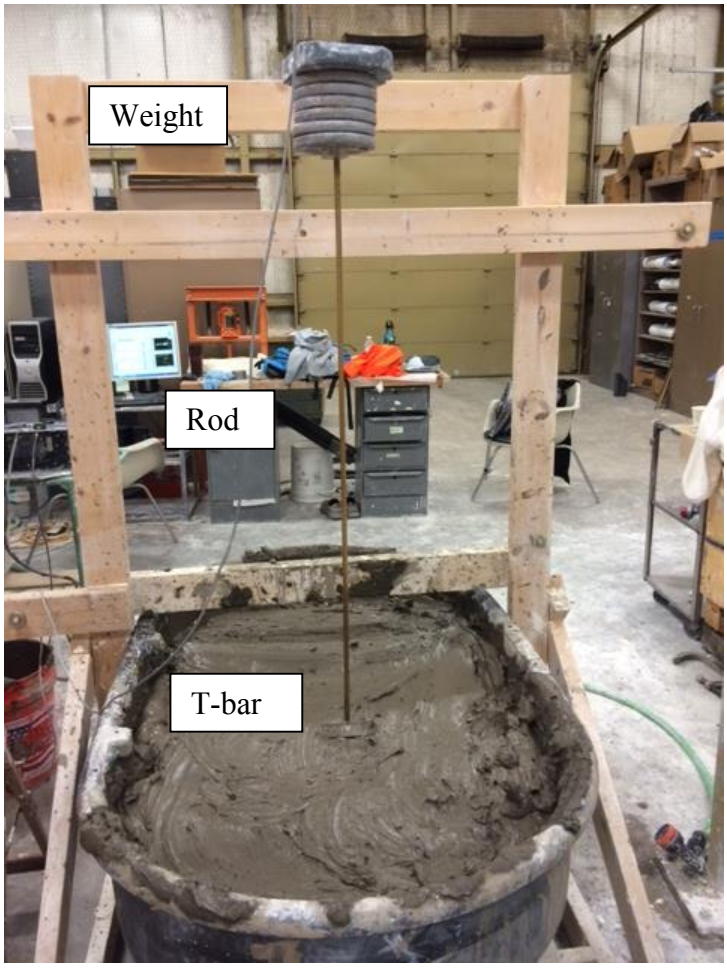

Figure 5.29 T-bar test

The undrained shear strength is obtained as follows from this tests:

$$S_u = \frac{(F_{total} - F_{rod})}{N_c \times A} \qquad Equation\ (5.4)$$

where: F_{total} = the total measured resistance in the load cell during T-bar penetration

F_{rod} = the measured resistance in the load cell during rod penetration (with no T-bar probe)

N_c = a bearing capacity factor typically taken to be 10.5

A = the projected area of the T-bar (1 inch by 4 inches)

To measure F_{total} at each depth, we connect the complete T-bar system (T-bar, rod, and weight) with the load cell and connected the load cell with the LMT displacement sensor. When the T-bar system is released, the T-bar penetrates into the soil under the weight. The Motion Control system controls the electric motor to maintain the T-bar system penetration at a contstant rate of 0.8 inches per second. To measure F_{rod}, we remove the T-bar probe from the T-bar system and repeat the test without the T-bar on the rod.

5.3.2 Results from T-bar tests

A set of T-bar tests were conducted to measure how the profile of undrained shear strength with depth changes with time after remolding in a test bed of marine clay. We measured the undraind shear strength of the clay versus depth at 0, 15, 30, 60 minutes, and 5 days after the clay was remolded (Figure 5.30).

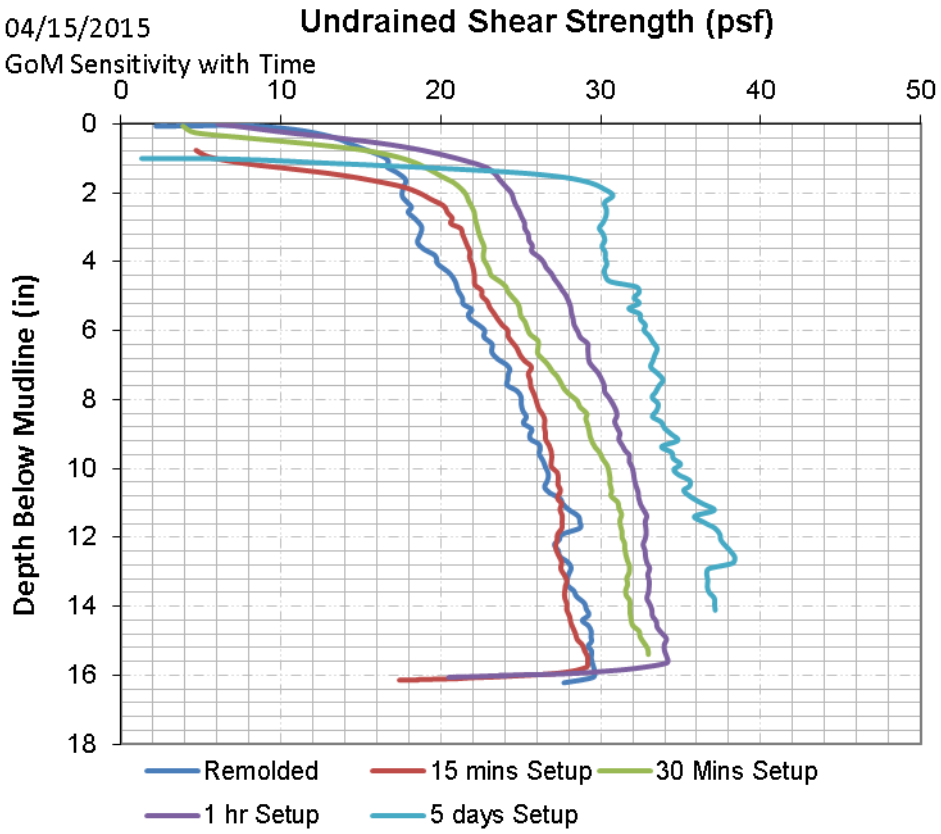

Figure 5.30 Sensitivity test on Golf of Mexico soil

From Figure 5.30, we saw that the Gulf of Mexico soil regained its strength fast.

5.4 Summary of the Data Acquisition and Motion Control Programs

We have developed a new Data Acquisition System in order to conduct drag tests with a model-scale of the Flying Wing Anchor. Two LabVIEW programs have been created: (1) a Data Acquisition program to record readings from displacement and load sensors, to convert those readings to variables of interest, to synchronize the readings versus time, and to store the readings in a data file; and (2) a Motion Control program to

control the movement of an electric motor system used to apply loads. A series of T-bar tests demonstrates that this new Data Acquisition System is functional.

Chapter 6: Conclusion and Future Work

The goal of this study was to develop a plan for conducting model tests on a new anchor concept, the Flying Wing Anchor (patent pending). The concept consists of a wing-shaped anchor that is embedded vertically into the sea floor by free falling through the water column, that is pitched to an angle to begin diving by pulling on the anchor line and triggering a mechanism to release the shank from the fluke, and that then dives further into the soil as the tension in the anchor line increases until its ultimate holding capacity is achieved with the anchor line pulling near normal to the fluke. The following tasks were completed to achieve this goal:

1. Develop a simplified analytical model to predict the trajectory and capacity of the anchor when it is pulled (dragged) through the soil by the anchor line.
2. Use the simplified analytical model to design an experimental program for model testing.
3. Create a data acquisition system to conduct model tests

6.1 Conclusion

Four modules constitute the simplified predictive model: (1) input module, (2) line model module, (3) dive initiation module, and (4) dive trajectory module. The dive trajectory module calculates the trajectory during drag and the holding capacity. We investigated four factors in a sensitivity study with this model: (1) the angle of the line with respect to the fluke when the shank is released during pitch rotation, (2) the profile of the undrained shear strength versus depth for the soil, (3) the diameter of the anchor line, and (4) the initial embedment depth after free fall. We drew the following conclusions:

(1) When the shank is released with the anchor line acting at an angle between 30 and 40 degrees relative to the normal to the fluke, the new anchor achieves the maximum ultimate depth and holding capacity.

(2) If the undrained shear strength is constant with depth, the ultimate dive depth is not influenced by the soil strength and the holding capacity is proportional to

the strength. If the soil profile increases linearly with depth with a small intercept at the mudline, the ultimate dive depth is constant and the holding capacity is proportional to the gradient of strength increasing with depth.

(3) A smaller diameter of the line makes the anchor dive deeper and increases the ultimate capacity.

(4) A deeper initial embedment depth after free fall makes the anchor dive deeper and increases the ultimate capacity.

To calibrate the simplified predictive model, we will measure the pure bearing factors and the drag trajectory of the anchor. To study the how the geometry of the anchor affects it interaction in the soil, we described a series of tests to measure the bearing capacity of the anchor in pure normal loading, pure shear loading and pure pitch rotation loading. To study the drag trajectory of the anchor, we designed a series drag embedment tests using the simplified predictive model by varying the diameter of the line, the area of the fluke, the depth of the initial embedment, and the initial pitch angle. With the measured trajectories in these model tests, intend to calibrate (1) the interaction between the anchor line and the anchor and (2) the yield interaction surface between shear and normal loading on the anchor during dive.

To conduct these model tests, we developed a new data acquisition system. The new system includes a Data Acquisition program and a Motion Control program. The Data Acquisition program is able to: (1) read signals from the electric sensors, (2) calibrate the signals to variables of interest, (3) synchronize the readings versus time, and (4) write the readings to a data file. The Motion Control program is able to control the movement of the electric motor.

6.2 FUTURE WORK

The following are recommendations for future work:

- Perform pure bearing factors tests to obtain bearing factors for experimental tests.

- Perform drag embedment tests to calibrate the simplified predictive model.
- Develop a larger test bed to allows the anchor to reach deeper ultimate depth.
- Extend the simplified predictive model to accommodate a general profile of undrained shear strength versus depth and an angle of the anchor line at the mudline that varies with the tension in the line or the location of the anchor.

APPENDICES

Appendix I – Spreadsheets and Program Code for Simplified Prediction Model

Parameters Share Module

Line Model Module

Dive Initiation Module

Trajectory Prediction Module

Line Model Function VBA Code

Appendix II – LabVIEW Modules

APPENDIX I – SPREADSHEETS AND PROGRAM CODE FOR SIMPLIFIED PREDICTION MODEL

Excel file link:

https://drive.google.com/open?id=0B2dTYYm5PJLsQk90Tl9FWGhGcDg&authuser=0

Line Model Module

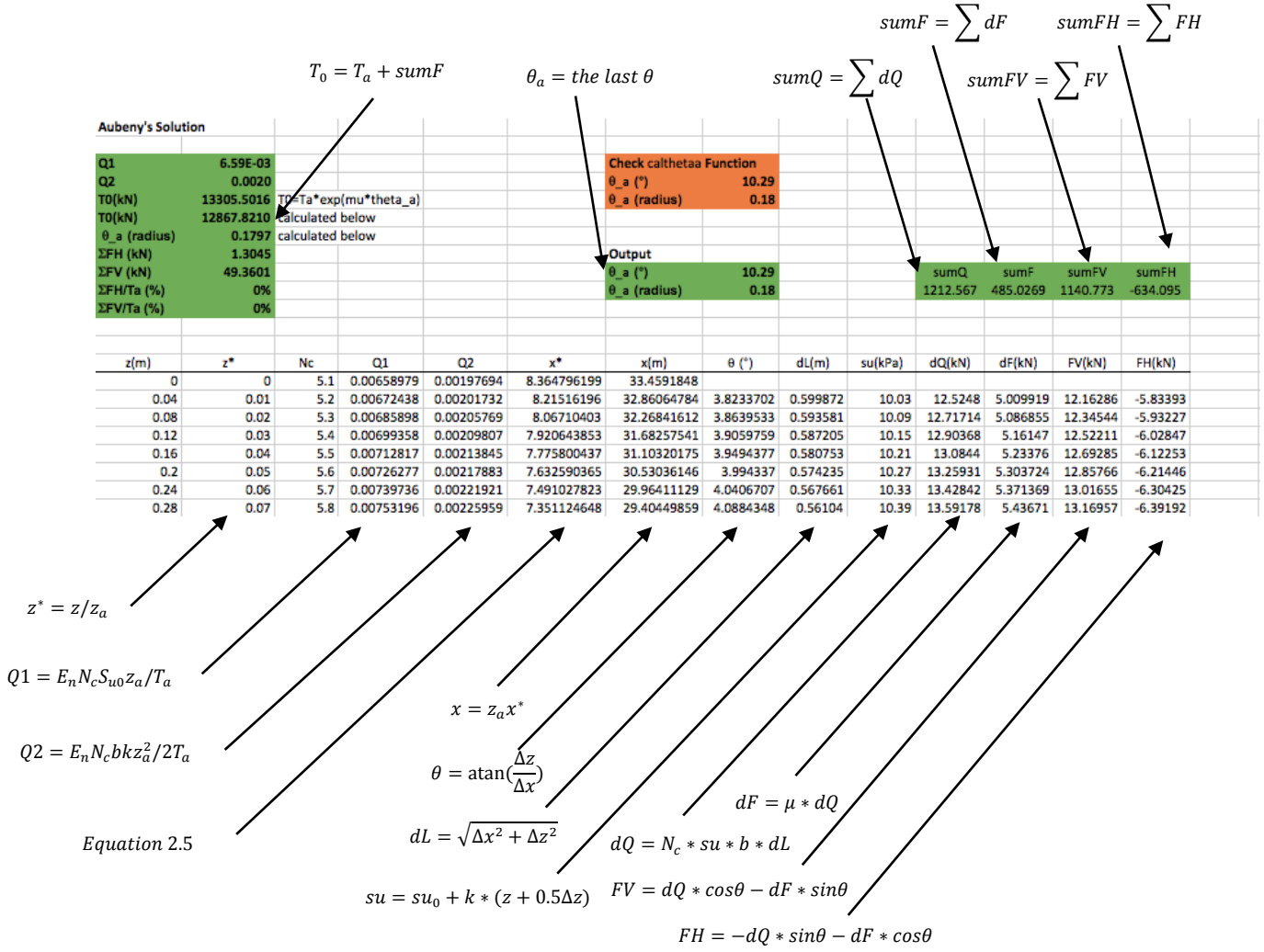

Dive Initiation Module

Initiation of Rotation

$T_s = \mathrm{T_a}\cos(90 - \theta_a - \alpha)$ $up = T_p(suA)/N_p$ $um = T_m(suA\text{^}1.5)/N_m$ $us = T_s(suA)/N_s$ $T_a(suA) = T_a(subz) * b * z/A$ $T_{av} = \mathrm{T_a}\sin\theta_a$

21	Pitch Rotation															
22	Angle between Fluke Normal and Line	Angle between Fluke and Vertical	Total Line Tension at Anchor*	Horizontal Line Tension at Anchor	Vertical Line Tension at Anchor	Line Angle with Horizontal*	Horizontal Line Tension at Anchor	Vertical Line Tension at Anchor	Total Line Tension at Anchor	Applied Moment to Fluke	Applied Shear to Fluke	Applied Bearing to Fluke	Moment Utilization	Shear Utilization	Bearing Utilization
23	β (deg)	α (deg)	Ta ($s_u$bz)	Tah ($s_u$bz)	Tav ($s_u$bz)	θ (deg)	Tah (s_uA)	Tav (s_uA)	Ta (s_uA)	T_m (s_uA^1.5)	T_s (s_uA)	T_p (s_uA)	um	us	up
24	-41.0452	0	16.57403	12.5	10.8834	41.04518	2.5	2.17668	3.314806	2.5	-2.17668	2.5	1	-0.54417	0.2
25	-40.0452	1	16.57403	12.5	10.8834	41.04518	2.5	2.17668	3.314806	2.537607547	-2.13272	2.537608	1.015043	-0.53318	0.203009
26	-39.0452	2	16.57403	12.5	10.8834	41.04518	2.5	2.17668	3.314806	2.574442114	-2.08811	2.574442	1.029777	-0.52203	0.205955
27	-38.0452	3	16.57403	12.5	10.8834	41.04518	2.5	2.17668	3.314806	2.610492481	-2.04286	2.610492	1.044197	-0.51071	0.208839
28	-37.0452	4	16.57403	12.5	10.8834	41.04518	2.5	2.17668	3.314806	2.645747667	-1.99699	2.645748	1.058299	-0.49925	0.21166

$\theta_a = calthetaa(Ta(KN))$ $T_{ah} = \mathrm{T_a}\cos\theta_a$ $T_m = \mathrm{T_{ah}} * \mathrm{e/L}$ $T_p = \mathrm{T_a}\sin(90 - \theta_a - \alpha)$

Pitch Rotation

$\beta = \alpha - \theta_a$ $T_{ah} = \mathrm{N_m}/(\frac{\mathrm{e}}{\mathrm{L}})$

Pitch Rotation															
Angle between Fluke Normal and Line	Angle between Fluke and Vertical	Total Line Tension at Anchor*	Horizontal Line Tension at Anchor	Vertical Line Tension at Anchor	Line Angle with Horizontal*	Horizontal Line Tension at Anchor	Vertical Line Tension at Anchor	Total Line Tension at Anchor	Applied Moment to Fluke	Applied Shear to Fluke	Applied Bearing to Fluke	Moment Utilization	Shear Utilization	Bearing Utilization
β (deg)	α (deg)	Ta ($s_u$bz)	Tah ($s_u$bz)	Tav ($s_u$bz)	θ (deg)	Tah (s_uA)	Tav (s_uA)	Ta (s_uA)	T_m (s_uA^1.5)	T_s (s_uA)	T_p (s_uA)	um	us	up
-41.0452	0	16.57403	12.5	10.8834	41.04518	2.5	2.17668	3.314806	2.5	-2.17668	2.5	1	-0.54417	0.2
-40.0452	1	16.57403	12.5	10.8834	41.04518	2.5	2.17668	3.314806	2.537607547	-2.13272	2.537608	1.015043	-0.53318	0.203009
-39.0452	2	16.57403	12.5	10.8834	41.04518	2.5	2.17668	3.314806	2.574442114	-2.08811	2.574442	1.029777	-0.52203	0.205955
-38.0452	3	16.57403	12.5	10.8834	41.04518	2.5	2.17668	3.314806	2.610492481	-2.04286	2.610492	1.044197	-0.51071	0.208839
-37.0452	4	16.57403	12.5	10.8834	41.04518	2.5	2.17668	3.314806	2.645747667	-1.99699	2.645748	1.058299	-0.49925	0.21166
-36.0452	5	16.57403	12.5	10.8834	41.04518	2.5	2.17668	3.314806	2.680196932	-1.95051	2.680197	1.072079	-0.48763	0.214416
-35.0452	6	16.57403	12.5	10.8834	41.04518	2.5	2.17668	3.314806	2.713829783	-1.90344	2.71383	1.085532	-0.47586	0.217106
-34.0452	7	16.57403	12.5	10.8834	41.04518	2.5	2.17668	3.314806	2.746635976	-1.85578	2.746636	1.098654	-0.46395	0.219731

Initation of Dive

$us^* = [1 - (up)^q]^{\frac{p}{n}}$

Initiation of Dive (shank open)															
	Angle between Fluke and Vertical	Angle between Fluke Normal and Line	Total Line Tension at Anchor	Horizontal Line Tension at Anchor	Vertical Line Tension at Anchor	Line Angle with Horizontal*	Horizontal Line Tension at Anchor	Vertical Line Tension at Anchor	Total Line Tension at Anchor	Applied Shear to Fluke	Applied Bearing to Fluke	Shear Utilization	Bearing Utilization		
Dive?	α (deg)	β (deg)	Ta ($s_u$bz)	Tah ($s_u$bz)	Tav ($s_u$bz)	θ (deg)	Tah (s_uA)	Tav (s_uA)	Ta (s_uA)	T_s (s_uA)	T_p (s_uA)	us	up	us*	Dive?
stay	84	42.95482	16.57403	12.49923	10.88428	41.04921	2.499847	2.176856	3.314806	2.25878	2.426077	0.564695	0.194086	0.999737	stay
stay	84	44.543	18.57403	14.34104	11.80378	39.457	2.868208	2.360755	3.714806	2.60573	2.647632	0.651432	0.211811	0.999613	stay
stay	84	45.95605	20.57403	16.20284	12.67907	38.04395	3.240567	2.535814	4.114806	2.95775	2.860654	0.739438	0.228852	0.999455	stay
stay	84	47.22172	22.57403	18.08086	13.51552	36.77828	3.616171	2.703105	4.514806	3.31381	3.06629	0.828453	0.245303	0.999258	stay
stay	84	48.36428	24.57403	19.97224	14.31756	35.63572	3.994448	2.863512	4.914806	3.673247	3.265359	0.918312	0.261229	0.99902	stay
dive	84	49.40269	26.57403	21.87476	15.08887	34.59731	4.374951	3.017774	5.314806	4.035542	3.458549	1.008885	0.276684	0.998735	dive
dive	84	50.35199	28.57403	23.78666	15.83256	33.64801	4.757331	3.166513	5.714806	4.400279	3.646443	1.10007	0.291715	0.9984	dive
dive	84	51.22432	30.57403	25.70654	16.55129	32.77568	5.141307	3.310258	6.114806	4.767126	3.829537	1.191782	0.306363	0.998012	dive

$dive\ when\ us > us^*$

Trajectory Prediction Module

$z = z + delta\ z$ $\quad su = su_0 + k * z$

15	trajectory												
16	Depth of Padeye	Horizontal Displacement of Padeye	Undrained Shear Strength	Angle between Fluke and Vertical	Angle between Fluke Normal and Line	Line Angle with Horizontal	Total Line Tension at Anchor*	Total Line Tension at Anchor*	Horizontal Line Tension at Anchor	Vertical Line Tension at Anchor	Horizontal Line Tension at Anchor	Vertical Line Tension at Anchor	Total Line Tension at Anchor
17	z (m)	x (m)	Su (Kpa)	α (deg)	β (deg)	θ (deg)	Ta ($s_u$bz)	Ta (kN)	Tah ($s_u$bz)	Tav ($s_u$bz)	Tah (s_uA)	Tav (s_uA)	Ta (s_uA)
18	8	0	22	84	50.66615	33.3338504	25.83284	1818.632	21.58289	14.19557	4.316579	2.839114	5.166568
19	8.9445963	9.9558017	23.416894	84	49.65212	34.34787673	23.44305	1964.103	19.35522	13.22695	4.328116	2.957743	5.242216
20	9.8760137	19.912989	24.814021	84	48.74695	35.25304852	21.51943	2109.452	17.573	12.42077	4.33878	3.066692	5.313155
21	10.794291	29.871557	26.191437	84	47.928	36.07200223	19.93277	2254.141	16.11121	11.73644	4.347729	3.167165	5.379003
22	11.699489	39.831499	27.549234	84	47.18796	36.81204452	18.61051	2399.356	14.89967	11.15127	4.357965	3.261603	5.443336
23	12.591632	49.792814	28.887449	84	46.5072	37.49279593	17.48231	2543.607	13.87099	10.64081	4.366459	3.349629	5.50327

$x = x + delta\ x$

$delta\ x = delta\ s * sin\alpha + delta\ n * \cos\alpha$

$Goal\ Seek\ T_a\ let\ f = 0$

15													
16	Total Line Tension at Anchor	Applied Shear to Fluke	Applied Bearing to Fluke	Shear Utilization	Bearing Utilization	Yield Function	delta s	df/dup	df/dus	(df/dup)/(df/dus)	delta n	delta x	delta z
17	Ta (s_uA)	T_s (s_uA)	T_p (s_uA)	us	up	f	(m)				(m)	(m)	(m)
18	5.166568	3.9961638	3.274767	0.999041	0.261981	9.06E-05	10	0.016806	1	0.016806	0.168065	9.962787	0.878141
19	5.203268	3.9645601	3.369905	0.99114	0.269592	-0.020465	10	0.018545	1	0.018545	0.185453	9.964604	0.860847
20	5.239437	3.9370972	3.457016	0.984274	0.276561	-0.038054	10	0.020246	1	0.020246	0.202465	9.966382	0.843929
21	5.273671	3.9118402	3.536823	0.97796	0.282946	-0.054019	10	0.0219	1	0.0219	0.219	9.968111	0.827484
22	5.308834	3.8908342	3.611804	0.972709	0.288944	-0.0671	10	0.023539	1	0.023539	0.235393	9.969824	0.811181
23	5.341536	3.8706352	3.681059	0.967659	0.294485	-0.079554	10	0.02513	1	0.02513	0.251295	9.971486	0.795366

$f = us - [1 - up^q]^{\frac{p}{n}}$

$\frac{df}{dup} = \frac{pq}{n}(1 - up^q)^{\frac{p}{n}-1} up^{q-1}$

$delta\ n = delta\ s * \frac{\frac{df}{up}}{\frac{df}{dus}}$

$delta\ z = delta\ s * sin\alpha - delta\ n * \cos\alpha$

Line Model Function VBA Code

```
Function calthetaa(Nc, b, su0, k, za, Ta, theta_0) As Double
    delta_za = za / 100
    za_2 = za - delta_za
    zastar = za / za
    zastar_2 = za_2 / za
    Q1 = Nc * b * su0 * za / Ta
    Q2 = Nc * b * k * za ^ 2 / 2 / Ta
    xstar = Sqr(1 / (2 * Q2)) * Application.WorksheetFunction.Ln((Q2 + Q1 / 2 + Sqr(Q2 ^ 2 + Q1 * Q2 + Q2 * theta_0 ^ 2 / 2)) / (Q2 * zastar + Q1 / 2 + Sqr(Q2 ^ 2 * zastar ^ 2 + Q1 * Q2 * zastar + Q2 * theta_0 ^ 2 / 2)))
    xstar_2 = Sqr(1 / (2 * Q2)) * Application.WorksheetFunction.Ln((Q2 + Q1 / 2 + Sqr(Q2 ^ 2 + Q1 * Q2 + Q2 * theta_0 ^ 2 / 2)) / (Q2 * zastar_2 + Q1 / 2 + Sqr(Q2 ^ 2 * zastar_2 ^ 2 + Q1 * Q2 * zastar_2 + Q2 * theta_0 ^ 2 / 2)))
    calthetaa = Atn(Abs((zastar_2 - zastar) / (xstar - xstar_2)))


End Function
```

APPENDIX II – LABVIEW MODULES

Data Acquisition program – user interface

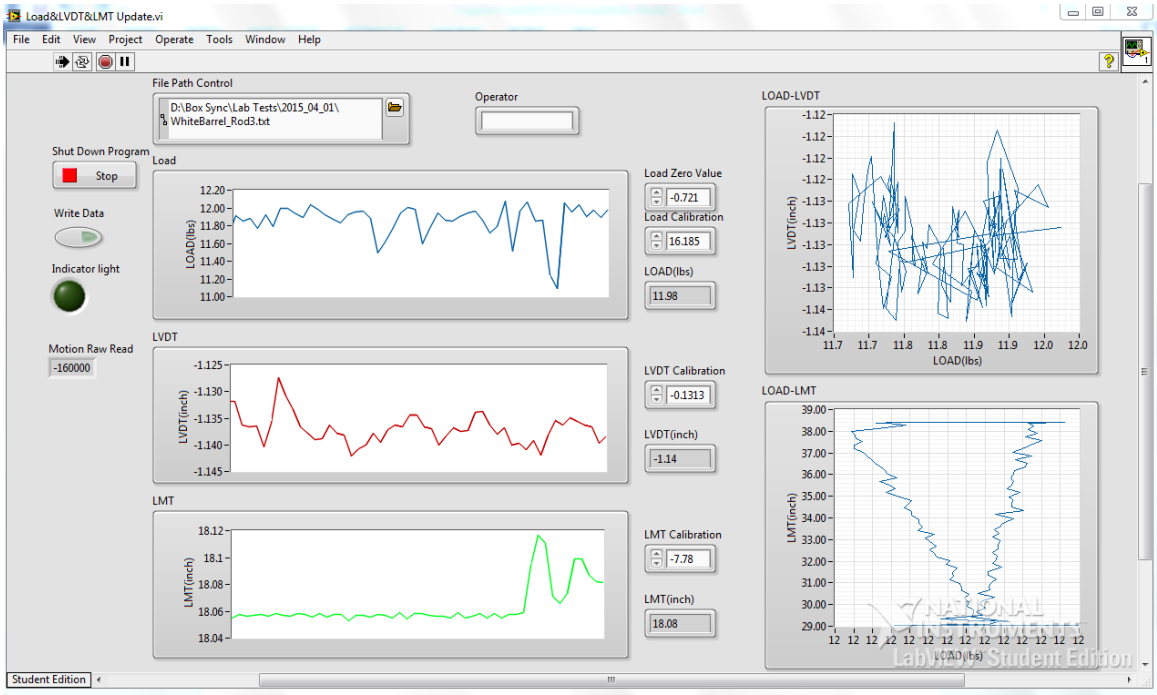

Data Acquisition program – Block Diagram layout

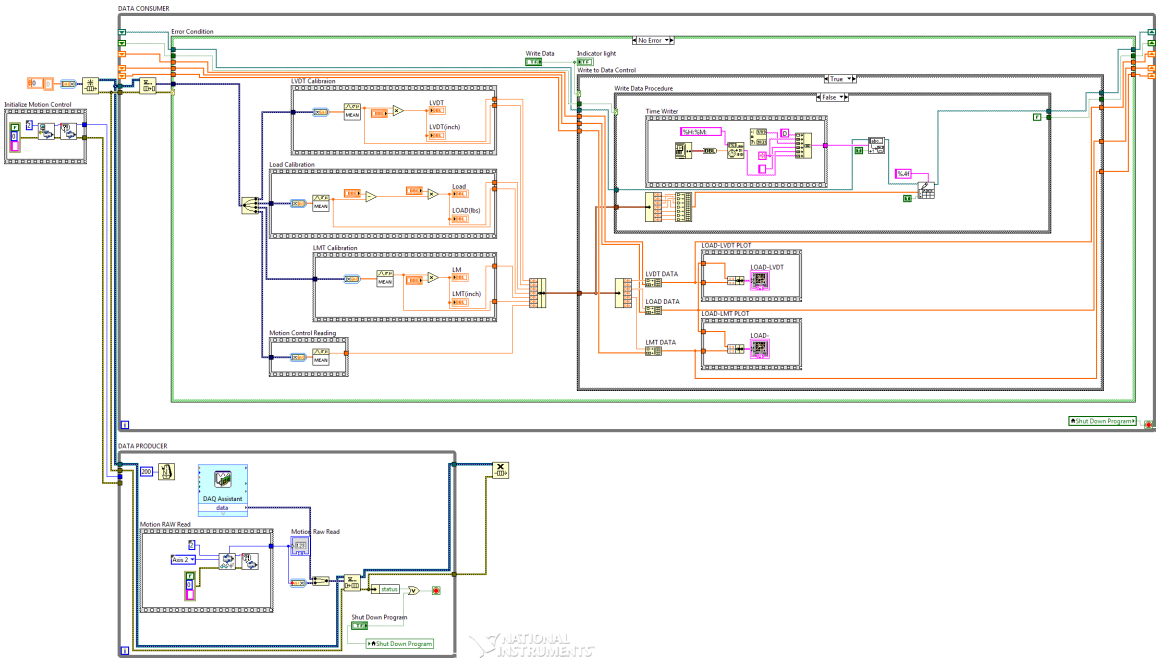

Data Acquisition program – data producer

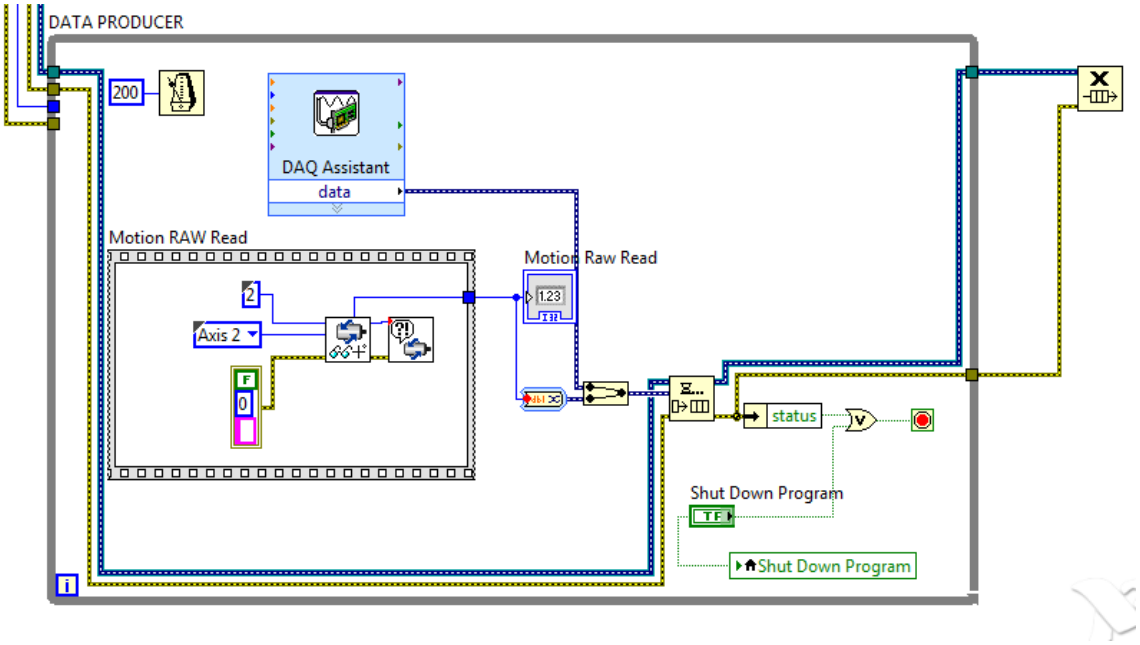

Data Acquisition program - calibration procedure

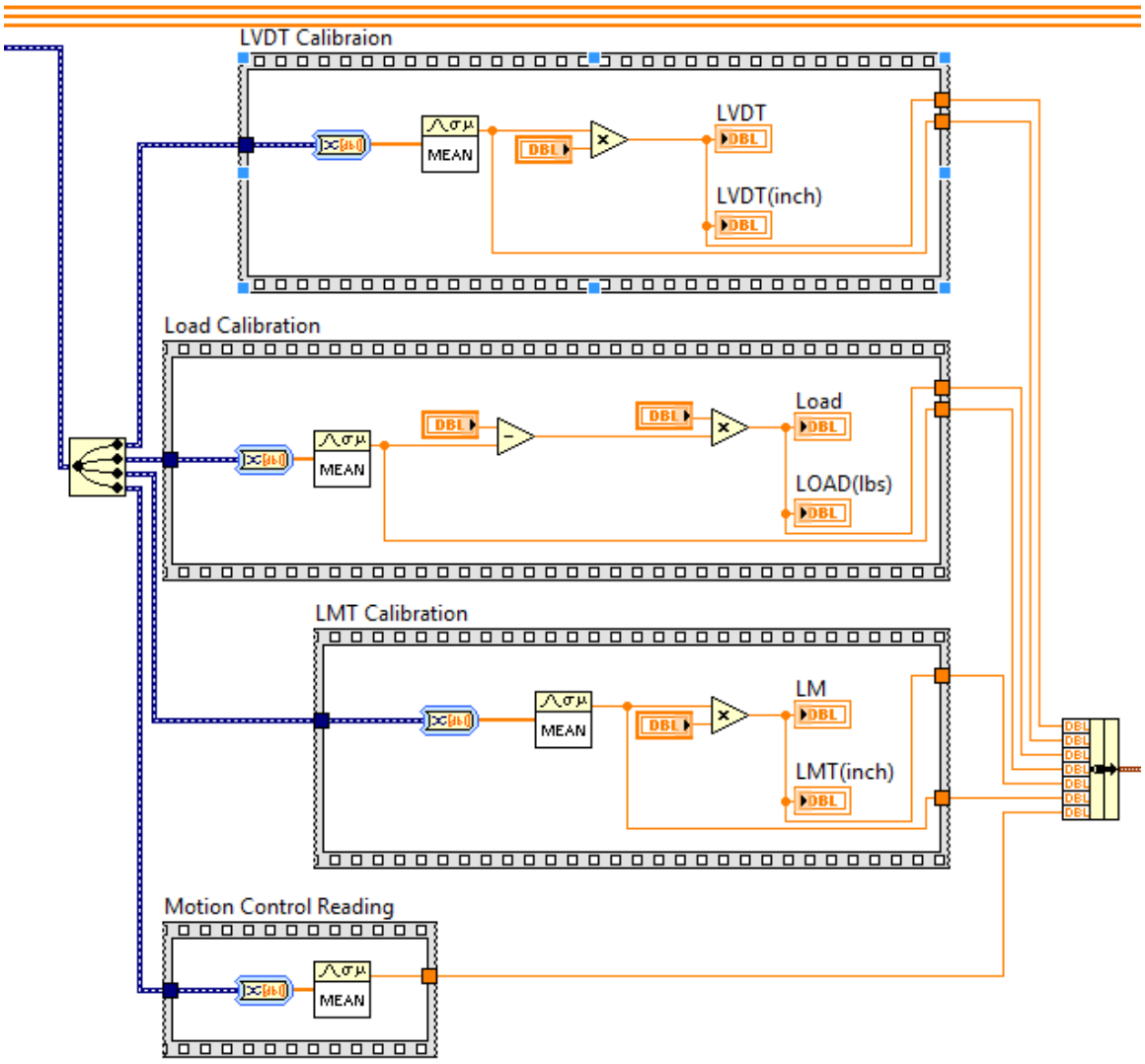

Data Acquisition program – chart output

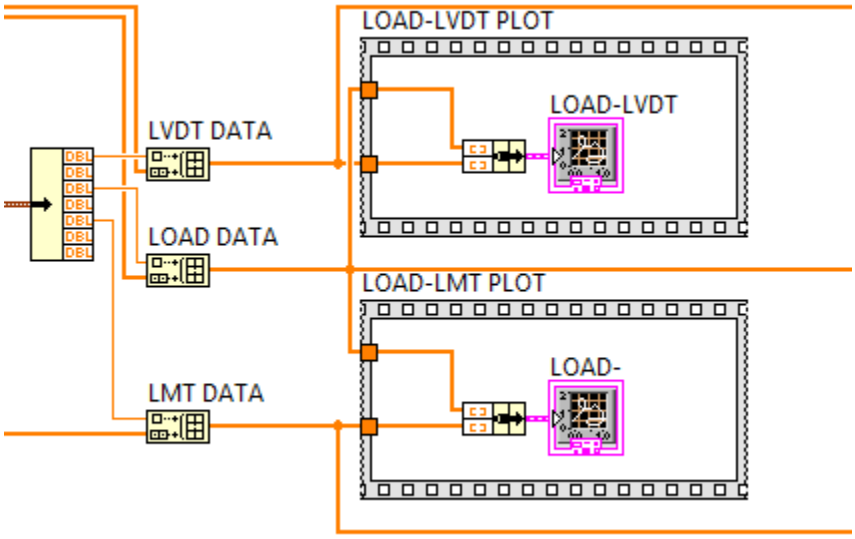

Data Acquisition program – writing data to file

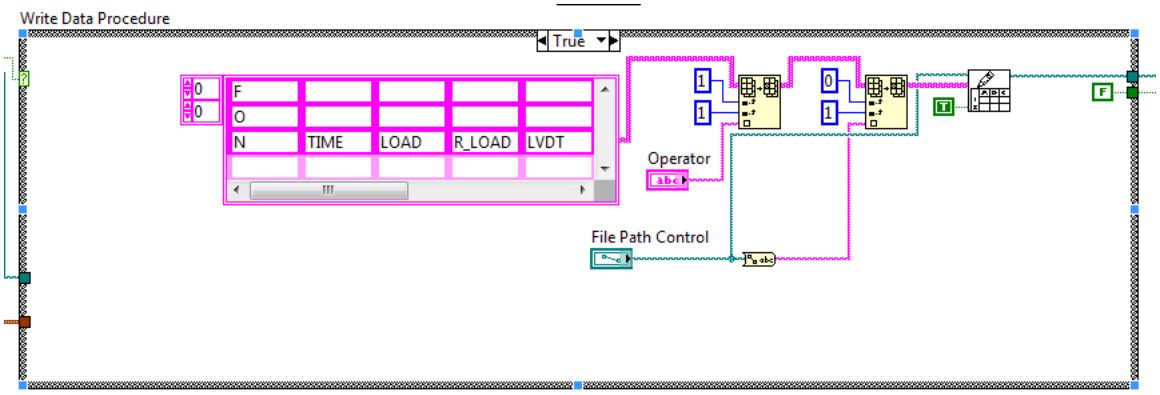

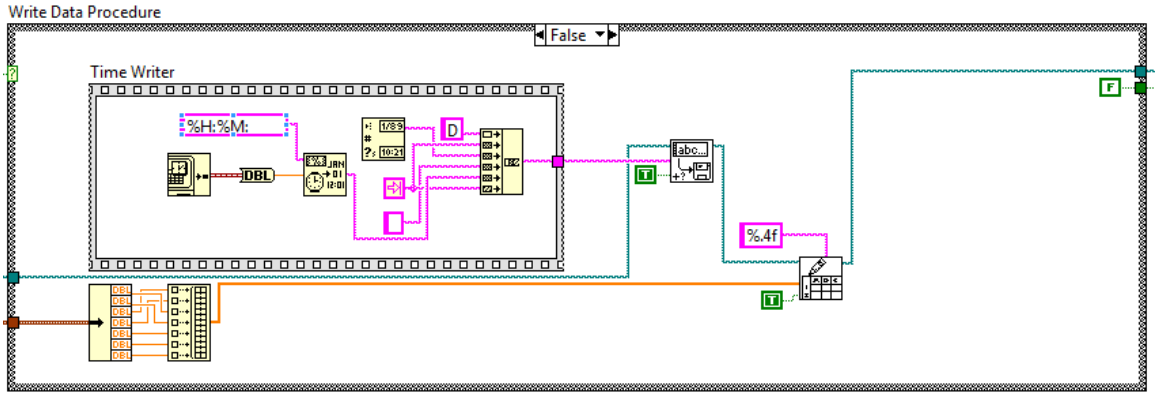

Motion Control program – user interface

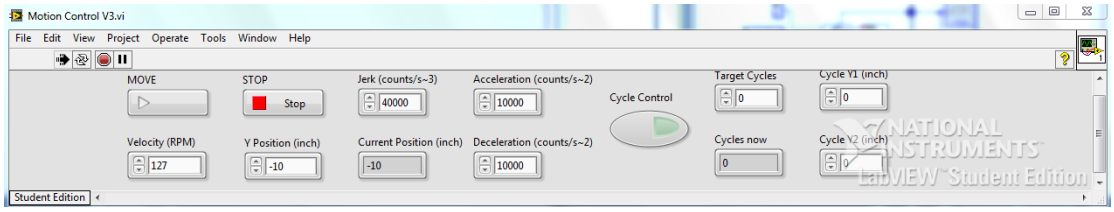

Motion Control program – Block Diagram layout

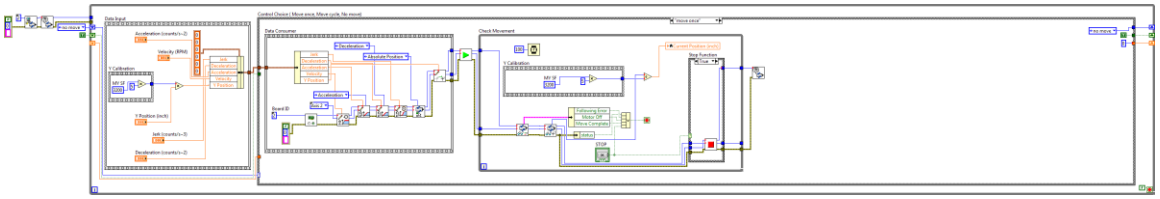

One Move

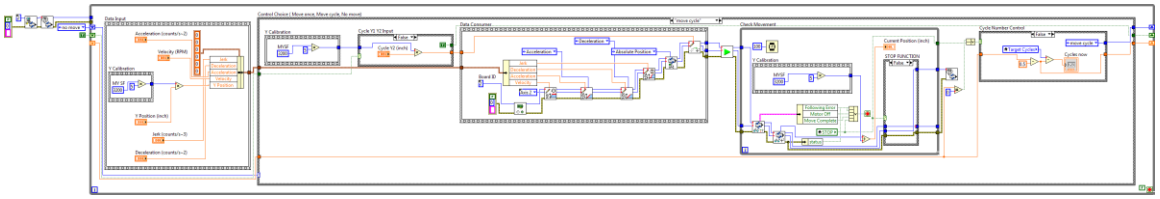

Cycle Moves

Motion Control program – Decision structure

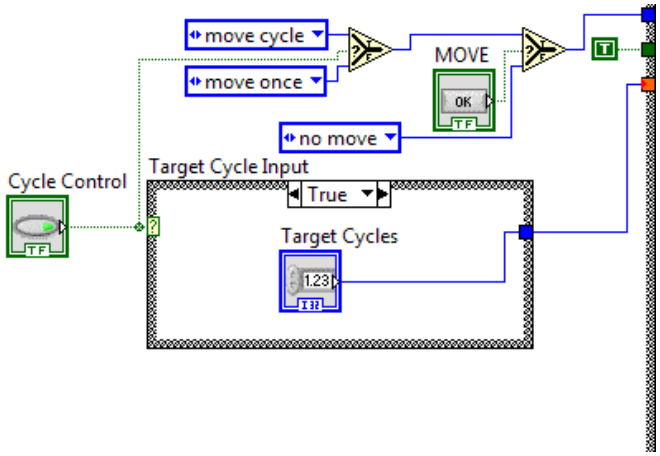

Motion Control program – Parameters input

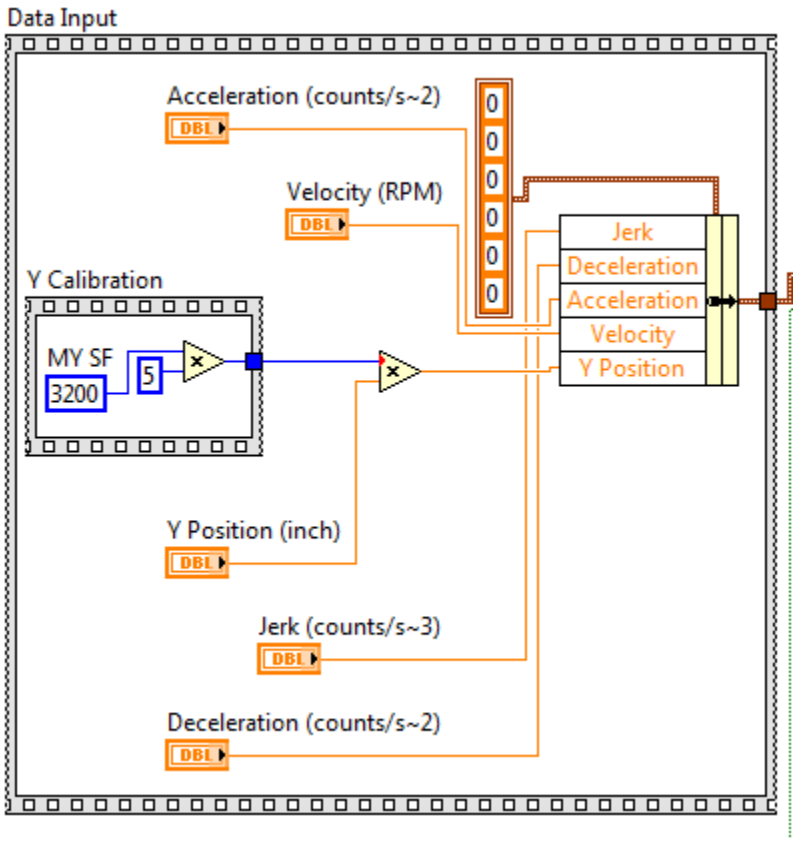

Motion Control – Command area to execute input

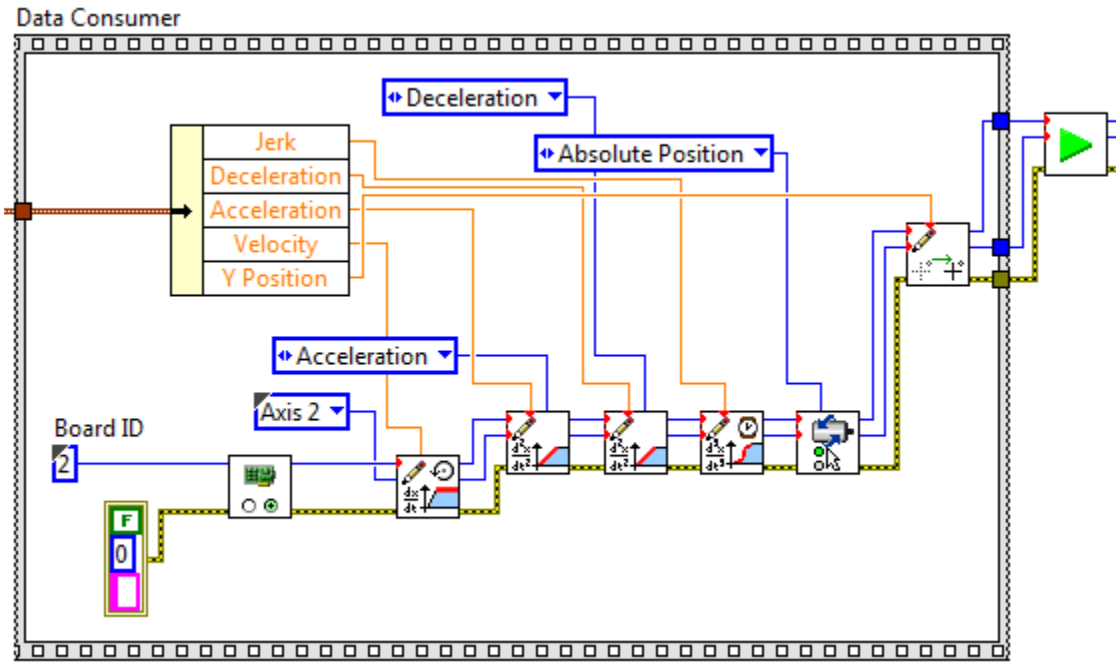

Motion Control – Check Movement

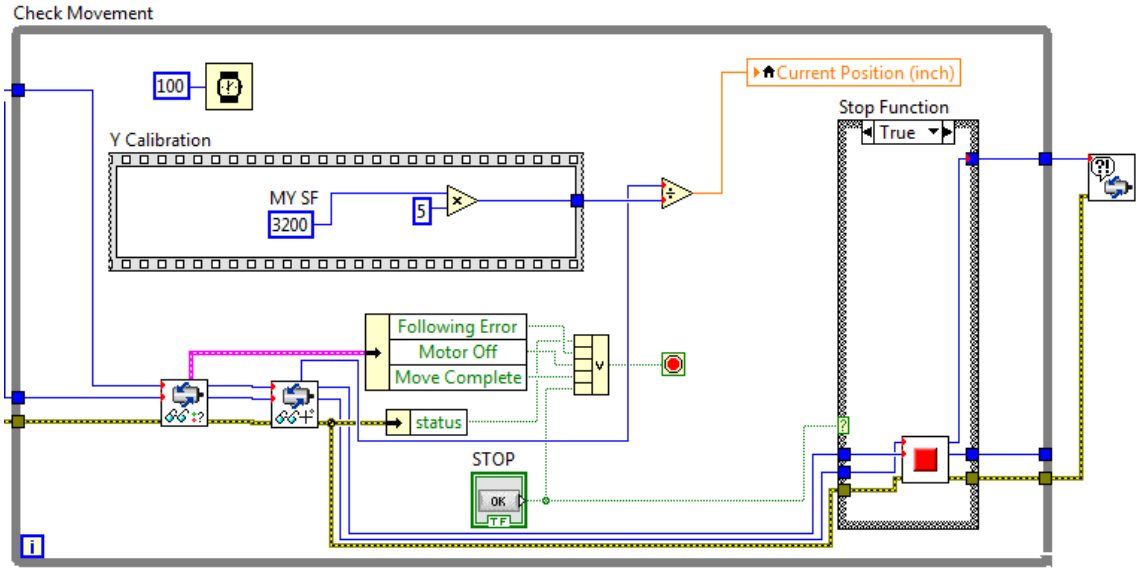

Motion Control – Stop condition in the Cycle Moves case

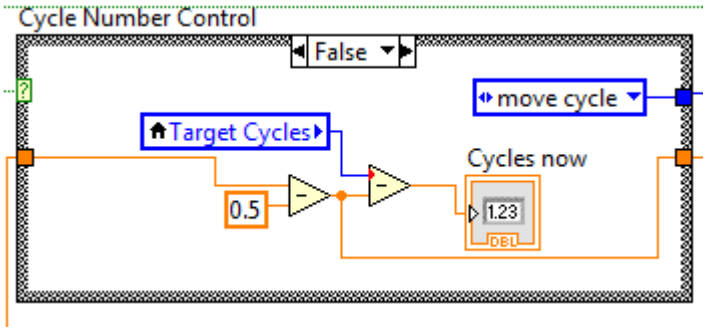

GLOSSARY

d = diameter of line

b = equivalent diameter of line

su_0 = undrained shear strength at mudline

k = soil strength gradient

μ = soil friction coefficient

T_0 = tension at mudline

T_a = tension at padeye

T_{ah} = horizontal line tension at padeye

T_{av} = vertical line tension at padeye

T_s = shear force to fluke

T_p = shear force to fluke

us = shear utilization

up = bearing utilization

um = moment utilization

θ_0 = angle between line and horizontal at mudline

θ_a = angel between line and horizontal at padeye

α = angle between fluke and vertical

β = angle between fluke normal and line

$\beta_{threshold}$ = angle between line and fluke normal at shank release

z_a = depth of padeye

z_0 = initial depth of padeye

A = area of fluke

x = drag displacement

N_m = moment bearing capacity factor

N_s = shear bearing capacity factor

N_p = normal bearing capacity factor

REFERENCES

Aubeny, C. P., & Chi, C. (2010). Mechanics of Drag Embedment Anchors in a Soft Seabed. Journal of Geotechnical and Geoenvironmental Engineering, 136(January), 57–68. doi:10.1061/(ASCE)GT.1943-5606.0000198

Aubeny, C. P., & Chi, C. (2013). Analytical Model for Vertically Loaded Anchor Performance. Journal of Geotechnical and Geoenvironmental Engineering, (January), 130605212729006. doi:10.1061/(ASCE)GT.1943-5606.0000979

Aubeny, C., Gilbert, R., Randall, R., Zimmerman, Z., McCarthy, K., Chen, C-H., Drake, A., Yeh, P., Chi, C-M. and Beemer, R. (2011), "The Performance of Drag Embedment Anchors (DEA)," Final Project Report, Offshore Technology Research Center, Prepared for Minerals Management Service, 333 pp.

Beemer, R. D. (2011). Analytical and Experimental Studies of Drag Embedment Anchors and Suction Caissons, (May).

Basic, T., & Drive, P. (2009). Motion Control, (April).

Degenkamp, G., and Dutta, A., "Soil resistances to embedded anchor chains in soft clay." Journal of the Geotechnical Enigneering Division, ASCE. Vol. 115, No. 10, 1420-1438, (1989).

Dahlberg, R. (1998), Design Procedures for Deepwater Anchors in Clay, Offshore Technology Conference, Paper OTC 8837, pp. 559-567. Houston.

Eklund T and Strøm, P.J. (1998), DIGIN Users's Manual ver. 5.3, DNV Report No. 96-3637, Rev. 03, dated 20 April 1998. Høvik

Flying Wing Anchor Project Proposal. (n.d.).

Flying Wing. http://en.wikipedia.org/wiki/Flying_wing (accessed April 15, 2015)

Ganjoo, K. (2010). Experimental Testing of Pure Translation and Rotation Loading of Drag anchors.

Gilbert, R. B., Lupulescu, C., Lee, C. H., Miller, J., Kroncke, M., Yang, M., Aubeny, C. P. and Murff, J. D. (2009), "Analytical and Experimental Modeling for Out-of-Plane Loading of Plate Anchors," Proc. Offshore Technology Conference, Houston, Texas, OTC Paper No. 20115.

Kim, B. M. I. N. (2005). Upper Bound Analysis for Drag Anchors in Soft Clay, (December).

McCarthy, K. B. (2011). Experimental In-Plane Behavior of a Generic Scale Model Drag Embedment Anchor in Kaolinite Test Beds.

Neubecker, S. R., & Randolph, M. F. (1995). Profile and Frictional Capacity of Embedded Anchor Chains. Journal of Geotechnical Engineering, 121(November), 797–803. doi:10.1061/(ASCE)0733-9410(1995)121:11(797)

Neubecker, S. R., & Randolph, M. F. (1995). Performance of Embedded Anchor Chains and Consequences for Anchor Design. Offshore Technology Conference, 1 May-4 May 1995, Houston, Texas. doi:10.4043/7712-MS

O'Neill, H. P., Bransby, F., & Randolph, M. F. (2003). Drag anchor fluke-soil interaction in clays, 94, 78–94. doi:10.1139/t02-096

Offshore wind turbines systems. http://energy.gov/articles/top-10-things-you-didn-t-know-about-offshore-wind-energy (accessed April 12, 2015)

Randolph, Mark; Gourvenec, Susan (2011). Offshore Geotechnical Engineering. Retrieved from http://www.eblib.com

Rami Mahmoud El-Sherbiny. (2005). Performance of Suction Caisson Anchors in Normally Consolidated Clay.

Stewart, W.P. (1992), "Drag Embedment Anchor Performance Prediction in Soft Soils," Offshore Technology Conference, Paper OTC 6970.

The Dalia deep offshore development in Angola. http://www.total.com/en/energies-expertise/oil-gas/exploration-production/strategic-sectors/deep-offshore/challenges/overcoming-harsh-conditions-ocean-deeps?%FFbw=kludge1%FF (accessed April 11, 2015)

The Bruce Dennla Mk 4 Vertically Loaded Anchor. http://www.bruceanchor.co.uk/Dennla_new_Mk4.html (accessed April 15, 2015)

Two "Dynamically Penetrating Anchors" before installation. http://www.ngi.no/en/NGI-Inc/Contentboxes-and-structures/Reference-projects/Reference-projects/Torpedo-Anchors/ (accessed April 15, 2015)

Typical trajectory for a Drag Embedment Anchor. http://lib.znate.ru/docs/index-107480.html?page=36 (accessed May 3, 2015)

Version, C. S., & Number, E. P. (2013a). LabVIEW Core 1 Course Manual, (August).

Version, C. S., & Number, E. P. (2013b). LabVIEW Core 2 Course Manual, (August).

Vryhof Anchors B.V. Vryhof Anchors. http://www.vryhof.com/pdf_2010/Mk5-MooringSystem.pdf (accessed April 05, 2015).

Zhang, W., Liu, H., Zhao, Y., & Yue, Y. (2014). Interactional Properties between Drag Anchor and Installation Line, 1-11. Doi:10.1061/(ASCE)GT.1943-5606.0001035

VITA

Yunhan Huang was born in Lian Yun Gang, China. He attended to attended in Xinhai High school at his home town in Sep 2006. After graduation of high school, he began to study in Hohai University, Nanjing, whose Water Conservancy and Hydropower major was the top in China. He graduated with a Bachelor of Science degree in Hydropower Engineer in Jun 2013. The stability of slope project in undergraduate graduation project made him interested in Geotechnical Engineer and he began to study at Department of Civil, Architectural, and Environmental Engineering at The University of Texas at Austin in August 2013. He worked under Prof. Gilbert on the anchor project of Offshore Geotechnical.

Email Address: yh.6543.ut@gmail.com